ACCELERATED TIME PROPAGATION IN TIME-DEPENDENT DENSITY FUNCTIONAL THEORY

By

Daniel Wayne Kidd

Dissertation
Submitted to the Faculty of the
Graduate School of Vanderbilt University
in partial fulfillment of the requirements
for the degree of

DOCTOR OF PHILOSOPHY
in
Physics

May 11, 2018

Nashville, Tennessee

Approved:
Kálmán Varga, Ph.D.
Sait Umar, Ph.D.
Andreas Berlind, Ph.D.
Robert Scherrer, Ph.D.
Neepa Maitra, Ph.D.

Dedicated to my parents

who provided the opportunities and support that made this possible.

ACKNOWLEDGMENTS

I would like to first thank a collection of mentors that have contributed, at various stages in my life, to forming who I am today as a person and as a scientist: John Claxton, Bob Campbell, Kevin Chopson, Tony Morton, Andrea Reeds, Alyce Dobyns, and, of course, many others. Thanks to Amy Welsh, for making me feel like I was one of the best students in AP calculus even though I just got lucky on the first assessment quiz; that confidence sort of carried me through. Similarly, thanks to Mrinal Raghupathi for telling me I was one of his better students in linear algebra, even though I definitely was not. Thanks to Libby Johnson and Don Pickert for answering my questions as both an undergraduate and graduate student.

Next, I would like to thank my advisor, Kalman Varga, for putting up with me for a total of seven years. Many thanks are owed to Kirk Bevan and his research group for being wonderful hosts during my two stays in Montreal and Kazuyuki Watanabe and his group for being equally wonderful hosts during my time in Tokyo. Of the latter, I would like to especially acknowledge many helpful conversations with Yasumitsu Suzuki and Elena Silaeva. Many past members of the Varga research group have helped me along the way: Joe Driscoll, Sergiy Bubin, Brandon Cook, Arthur Russakoff, Jorge Salas, Shenglai He, Yonghui Li, and Cody Covington.

Finally, I would like to acknowledge and thank the friends that have been there through the long haul and have meant the world to me: Michael Ioannou, Brad Hinkle, Alex Lee, Andrew Eagar, Cole Perry, Seth Coats, Thomas McLaughlin, Zac Mahoney, Glenn DeWitt, Bob Shi, Paul Hart, Mack Atkinson, Max Ofori, Jeff Bond, and even Mickey Esparza.

FUNDING ACKNOWLEDGMENTS

The work presented in this thesis has been supported by the National Science Foundation (NSF) under Grants No. PHY 1314463, ECCS 1307368, OISE 1261117, and OISE 1613549. Furthermore, this work used the Extreme Science and Engineering Discovery Environment (XSEDE), which is supported by National Science Foundation Grant No. OAC 1053575.

TABLE OF CONTENTS

Page

Chapter

LIST OF TABLES

LIST OF FIGURES

Chapter 1

INTRODUCTION

Recent advances in laser technology have allowed for the development of pulses with sub-femtosecond (10^{-15} s) pulse durations [1–3]. The advent of such pulses opens the door to the probing of nonstationary electron states and laser-induced electron dynamics which evolve on the timescale of hundreds or even tens of attoseconds (10^{-18} s) [4–7]. It is expected that this ability will lead to the control of electron dynamics in nanoscale systems which play a role in numerous fields of physics [8–10], optics [11, 12], biology [13, 14], material engineering [15], chemistry [16, 17], and the development of next generation computing devices [18, 19]. With such an intense focus on attosecond-scale phenomena and growing experimental capabilities, the need for similarly sophisticated theoretical and computational analysis becomes ever more prevalent in order to interpret experimental findings, as well as to guide new studies.

The original breakthrough of Erwin Schrödinger's equation describing the wavelike property of particles in 1926 [20] provided the backbone of the theoretical treatment of electronic structure and dynamics. However, it was soon realized that for the description of many electrons, where the N-particle wave function is to be defined as an $3N$-dimensional quantity, $\Psi(\mathbf{r}_1, \mathbf{r}_2, ..., \mathbf{r}_N)$, an analytical solution to this equation was not available and further work was required in order to achieve a theoretical description of many desirable systems. This complication was soon to be addressed in 1927 by Llewellyn Thomas [21] and Enrico Fermi [22], who proposed a semiclassical approach, circumventing the discussion of a many-particle wave function in favor of the relatively simple three-dimensional electron density, $\rho(\mathbf{r}) = N \int |\Psi(\mathbf{r}, \mathbf{r}_2, ..., \mathbf{r}_N)|^2 d\mathbf{r}_2, ..., d\mathbf{r}_N$, in order to describe the electronic structure of atoms. While this representation, known today as the Thomas–Fermi model, was limited due to an approximate expression for the kinetic energy and the exclusion of the exchange interaction resulting from Pauli's principle, it served as an important early step towards realizing a theoretical description of electronic configuration while avoiding the use of the many-particle wave function.

Simultaneous to the invention of the Thomas–Fermi model, Douglas Hartree introduced the self-consistent field approach to determining approximate many-particle wave functions as the product of single-particle wave functions [23]. In what would be known as the Hartree method, no potentials incorporating semiemperical parameters were used, thus leading to a method described as *ab initio*, meaning "from first principles". The self-consistent field approach meant that the equations would be solved via a method such as iteration, in which a solution is found and then fed back into the original equation repeatedly until satisfactory convergence is achieved. This method was capable of well representing atomic orbitals, but the resulting energies were found to be too inaccurate. This property was addressed soon thereafter as a product of a wave function which was not antisymmetric and, thus, lacking the exchange interaction. In 1929, John C. Slater introduced the form of the antisymmetric many-particle wave function [24], and one year later, Vladimir Fock [25] and Slater [26] both simultaneously incorporated this concept into the Hartree method, from then on known as the Hartree–Fock method.

While descriptions of atomic structures continued to grow more sophisticated through advances such as the descriptions of Felix Bloch [27] and Eugene Wigner and Frederick Seitz [28, 29] for the conduction of electrons in crystalline solids, as well as Hans Hellman's replacement of core electrons and nuclei with effective pseudopotentials [30], the full solutions for systems larger than medium-sized atoms remained elusive due to the computational demand. It was not until the advent of electronic computers in the 1950s that small molecules could begin to be described using the Hartree–Fock method.

The early 1960s brought a return to the concept of representing electronic structures only by the density rather than the many-particle wave function. This concept had existed, as stated above, since Thomas and Fermi's early attempts at constructing single atom structures. In fact, Paul Dirac made the following note in 1930 [31]:

> “Each three-dimensional wave function will give rise to a certain electric density. This electric density is really a matrix, like all dynamical variables in the quantum theory. By adding the electric densities from all the wave functions, we can obtain the total electric density for the atom. If we adopt the equations of the self-consistent field as amended for exchange, then this total electric density (the matrix) has one important property, namely, if the value of the total electric density at any time is given, then its value at any later time is determined by the equations of motion. This means that *the whole state of the atom is completely determined by this electric density; it is not necessary to specify the individual three-dimensional wave functions that make up the total electric density.* Thus one can deal with any number of electrons by working with just one matrix density function.”

It was the years of 1964 and 1965 that saw the landmark work of Pierre Hohenberg, Walter Kohn, and Lu Jeu Sham [32, 33], in which it was proven that the many-particle electron density did, indeed, uniquely describe the entirety of any given ground state structure, i.e., that there was a one-to-one mapping of the potential and ground state density and that, given an adequate representation of the exchange interaction, one could formulate a self-consistent field method to solve for an electronic ground state while avoiding ever representing the many-particle wave function.

The proposed method consisted of solving a set of single-particle, time-independent Schrödinger equations for fictitious particles in a local effective potential. The employed representation for each of the energy terms in the formalism, including approximations for the exchange interaction and the dynamic correlation interactions resulting from the instantaneous Coulomb repulsion between electrons (together called exchange-correlation), would need to be functionals of the density; i.e., expressions with the density as an input which would produce a scalar value. This feature led to the resulting name of density functional theory (DFT). While this formalism presented a far more straightforward alternative to the Hartree–Fock method with no limitation to small systems, such wave function theories still remained popular until the 1990s, in which better approximations to the exchange-correlation functional were produced.

DFT has now become the prominent tool of choice for describing the ground state electronic structure of atoms, molecules, and bulk materials, with numerous choices of representations for the exchange-correlation functional which can be chosen to best suit a given application. Applications are numerous in fields of physics [34] as well as chemistry [35, 36], geosciences [37], biology [38], and material science [39]. Walter Kohn shared a Nobel Prize in Chemestry in 1998 [40] for inventing the theory.

While DFT is a theory for the ground state of an electronic system, its development played a fundamental role in the formation of a theory describing nonadiabatic electron dynamics. In 1984, Erich Runge and Eberhard K. U. Gross presented an extension to DFT which showed that there was a similar one-to-one mapping between a time-dependent potential and the time-dependent many-particle electron density [41]. Thus, using similarly approximate expressions for the time-dependent exchange and correlation functionals, one may solve the set of single-particle, time-dependent Schrödinger equations corresponding to the fictitious noninteracting particles of DFT in order to achieve a time propagation of the electron density and recover *ab intio* results for excited state phenomena like optical spectra, scattering, and ionization.

This so-called time-dependent density functional theory (TDDFT) first emerged as a prominent tool in theoretical modeling with the introduction of an efficiently implementable formalism in the late 1990s [42, 43] and has seen increasingly prevalent use since then [44–47]. This rise in popularity has been driven by the fact that, in this same span of time, rapid breakthroughs in laser technology have yielded the advent of femtosecond-width pulses [48–51] as well as extreme ultraviolet pulses generated by means of above threshold ionization [52] or high harmonic generation [53–55] with widths of less than one femtosecond [56–58]. Such intense, few-cycle pulses allow for the metrology of ultrafast light signals and the real-time observation and influence of electron dynamics which take place on the attosecond timescale [59]. In the following discussion, examples of such processes are explained as motivation for the further sophistication of TDDFT as a means of theoretical investigation.

The optical spectra of materials is a property commonly referred to in order to characterize potential functionality via quantities such as absorption, reflectivity, and photoluminescence. Optical excitations, furthermore, provide means of technical applications such as light-emitting devices and laser technology. It is thus important to accurately describe such spectra via reliable *ab initio* methods in order to address these excitations.

Since the 1970s, *ab initio* Green's function based methods, not entirely unlike TDDFT, such as solving the Bethe–Salpeter equation [60, 61] or using the GW approximation [62–64], have been employed in order to assess the optical spectra of materials. However, the advent of TDDFT allows for the important practical advantage of incorporating a dependence on the electron density rather than on multivariable Green's functions [45]. The application of TDDFT to the calculation of optical spectra represents one of the earliest means of the theory's benchmarking and is still commonly used to study new materials of interest [65–70].

High harmonic generation (HHG) is another important, fundamentally attosecond-scale process in which laser light of frequency ω can be used to generate new integer multiples of that frequency, $n\omega$, via interaction with matter. This phenomenon was first observed in 1977 when up to 11 harmonics of nanosecond CO_2 pulses were generated by interaction with a electron plasma generated from solid targets [71]. A similar study was conducted in 1981 in which harmonics up to the 46th order were reported [72]. Later, in 1987, the first example of high harmonic generation in gases was observed [73]. The three step semi-classical explanation of HHG was first suggested by Paul Corkum in 1993 [74]. In this simplified picture, an initially bound electron undergoes three stages of motion: (1) ionization, (2) acceleration in the laser field, and (3) recombination with the ion core, resulting in the emission of a HHG photon. This laser-matter interaction has been widely used in order to generate single attosecond pulses, as mentioned above, as well as to characterize systems of interest and monitor electron dynamics [75–78]. Today there is much interest in the recently realized generation of high harmonics in solids [79–82] which has become a popular subject of TDDFT studies [83–85].

The field of plasmonics represents an intersection between optics and electronics in which electromagnetic waves are converted into collective excitations of free electrons [86]. The creation of these collective excitations, often described as quasiparticles named plasmons, is a phenomenon theorized to find applications within the fields of nanophotonics [87–89], biology [90, 91], sensing [92], single molecule detection [93], nanophotonic lasers [94], photovoltaic devices [95, 96], spectroscopy [97, 98], and solar energy harvesting [99, 100]. As components exhibiting plasmonic behavior continue to shrink due to the emphasis on smaller electronic devices, the study of this behavior must be conducted within a truly quantum framework, rather than by classical models [101–105]. This calls for the computational modeling of methods such as TDDFT, which has become a popular method of analyzing such field-induced, attosecond-scale electron dynamics [106–108].

Finally, the focus of much research as of late, within the field of information technology, has been the development of faster signal processing devices. Presently, high-speed devices employ radiofrequency electric fields in order to control the electronic motion within semiconductors, which provides operating speeds at the terahertz (10^{12} Hz) range [109]. The next breakthrough, therefore, is slated to be the development of signal processing devices operating within the petahertz (10^{15} Hz) regime. Suggested means of achieving transistors of these speeds include optically driven semiconductors [110], dielectrics [111, 112], or even nano-scale vacuum-tube diodes [113–116]. TDDFT may be used in order to further assess the functionality of these proposed devices as well as to investigate new potential mechanisms [117].

As demonstrated above, the modeling of attosecond electron dynamics as facilitated by TDDFT stands to shed light on various processes of much interest. Therefore, the increased optimization of computational methods within TDDFT are of great importance, as the furthering of speed and accuracy of such codes stands to provide enhanced reliability, applicability, and accessibility. Herein such improvements are developed, discussed, and tested. The thesis is divided as follows.

Chapter 2 contains a succinct review of the relevant formalism. This includes a brief introduction to many-body quantum theory, comprehensive reviews of DFT and TDDFT, remarks on the inclusion of external, dynamic electromagnetic fields, the psuedopotential representation for ionic cores, and the Bloch theory of describing periodic systems.

Chapter 3 provides an examination of various choices of basis—the discrete representation for the computational space. Conventional choices are presented, such as the atomic orbital, plane wave, and real space grid representations.

Chapter 4 presents the pseudospectral basis which exhibits enhanced accuracy. Techniques of sum-acceleration are discussed, which allow the kinetic energy matrix in this basis to be of the same sparsity as that used in the related real space grid approach. The sum-accelerated pseudospectral basis is then introduced to density functional calculations as a proposed means of enhanced scalability with respect to computational domain and matrix bandwidth, providing better computational efficiency.

Chapter 5 describes selected options for solving the single-particle time-dependent Schrödinger equation via time propagation of the wave function. Again, conventional techniques are presented, including the Taylor expansion, Crank–Nicolson, and split operator approaches. An introduction of exponential integrator methods to time-dependent density functional theory follows, accompanied by a comparison to a wide variety of alternative, popular propagation techniques as applied to the one-dimensional helium atom. It is shown that such exponential integrator methods appear to allow for improvements by orders of magnitude in accuracy when describing dynamics driven by the nonlinear part of the Hamiltonian.

Chapter 6 discusses the simulation of laser-induced electron dynamics in crystalline solids. The time-dependent Volkov state basis is introduced and related to the plane wave basis representation. The Volkov state basis is compared to the plane wave basis and real space grid approaches within calculations for both one- and three-dimensional test cases in which the Volkov state basis is shown to speed up calculations by an order of magnitude. This basis is then applied to the investigation of a nano-scale vacuum tube diode device.

Chapter 7 finally concludes the thesis and provides an outlook on potential further improvements to the computational schemes discussed herein as well as possible applications.

Chapter 2

BACKGROUND AND THEORY

2.1 Many-Body Quantum Theory

The central landmark of the quantum revolution was Schrödinger's equation, widely known as the time-dependent Schrödinger equation (TDSE), for the evolution of nonrelativistic wave functions, which provides a probabilistic interpretation to the location and momentum of massive particles. For a collection of such particles, a time-dependent, N-body wave function, $\Psi(\mathbf{r}_1, \mathbf{r}_2, \ldots, \mathbf{r}_N; t)$, may be described using this differential form,

$$i\hbar\frac{\partial}{\partial t}\Psi(\mathbf{r}_1, \mathbf{r}_2, \ldots, \mathbf{r}_N; t) = H\Psi(\mathbf{r}_1, \mathbf{r}_2, \ldots, \mathbf{r}_N; t). \tag{2.1}$$

Here, $\hbar$ is the reduced Planck constant and H is the Hamiltonian. This latter ingredient fully identifies the physics of the system in question, including all relevant interactions felt by the particles described. For example, the Hamiltonian used to describe N electrons in an atom would take the form

$$H = \sum_{i=1}^{N} T_i + \sum_{i=1}^{N} V^{\text{nuc}}(\mathbf{r}_i) + \sum_{i<j}^{N} V^{\text{ee}}(\mathbf{r}_i, \mathbf{r}_j) \tag{2.2}$$

where the first term represents the total kinetic energy,

$$T_i = -\frac{\hbar^2}{2m}\nabla_i^2, \tag{2.3}$$

the second term describes the external Coulomb interaction with a nucleus of Z_A protons and location $\mathbf{R}_A$,

$$V^{\text{nuc}}(\mathbf{r}_i) = \frac{1}{4\pi\varepsilon_0}\frac{-Z_A e^2}{|\mathbf{r}_i - \mathbf{R}_A|}, \tag{2.4}$$

and the third term describes the interaction of Coulomb repulsion between electrons

$$V^{\mathrm{ee}}(\mathbf{r}_i, \mathbf{r}_j) = \frac{1}{4\pi\varepsilon_0} \frac{e^2}{|r_i - r_j|}. \tag{2.5}$$

In the case of the atom described above, however, the TDSE may be simplified to its time-independent form, known as the time-independent Schrödinger equation (TISE), which describes wave functions at equilibrium within static potentials. The TISE takes the form of an eigenvalue problem,

$$H\Psi(\mathbf{r}_1, \mathbf{r}_2, \ldots, \mathbf{r}_N) = E\Psi(\mathbf{r}_1, \mathbf{r}_2, \ldots, \mathbf{r}_N), \tag{2.6}$$

where the eigenvalue, E, represents the energy of the wave function. This form suggests that multiple eigensolutions are possible, giving rise to the description of individual states, typically ordered by their energy value. The state with the lowest energy is known as the ground state, while that with the next highest value is the first excited state and so on.

While the TDSE and TISE are simple to formulate for physical systems such as the atom, an analytic solution is usually impossible for $N > 1$, due to the two-body, electron-electron interaction potential. Therefore, in order to describe such systems, it is necessary to develop accurate numerical approximations. Paul Dirac made note of this in 1929 [118],

> “The underlying physical laws necessary for the mathematical theory of a large part of physics and the whole of chemistry are thus completely known, and the difficulty is only that the exact application of these laws leads to equations much too complicated to be soluble. It therefore becomes desirable that approximate practical methods of applying quantum mechanics should be developed, which can lead to an explanation of the main features of complex atomic systems without too much computation.”

As mentioned in Chapter 1, this desire for accurate numerical approximations led to the development of *ab initio* theories such as the Hartree-Fock method, and eventually DFT. This chapter focuses on the latter and its extension to time-dependent phenomena, TDDFT. The inclusion of relevant interaction potentials, such as that with external electromagnetic fields and core electrons, are also discussed. Lastly, modifications necessary when describing periodic Hamiltonians are presented.

2.2 Density Functional Theory Formalism

As introduced above, DFT is a widely employed *ab initio* theory which makes use of the many-electron probability density in order to fully describe the system of interest, rather than attempting to approximate the many-electron wave function. This density may be defined as

$$\rho(\mathbf{r}) = N \int |\Psi(\mathbf{r}, \mathbf{r}_2, ..., \mathbf{r}_N)|^2 d\mathbf{r}_2, ..., d\mathbf{r}_N, \tag{2.7}$$

where $\int_V \rho(\mathbf{r}) d\mathbf{r}$ represents the probability of finding an electron within volume V. The use of this simplified metric is made possible by the two Hohenberg–Kohn theorems of Ref. [32] which describe interacting particles within an external potential, $V^{\text{ext}}(\mathbf{r})$. The first theorem is as follows:

Theorem 2.2.1 *The external potential (and, thus, the total energy) is a functional of the density, apart from a trivial additive constant.*

This statement establishes the one-to-one mapping of the external potential and electronic density and allows one to conclude that the many-particle ground state, as a whole, is a unique functional of $\rho(\mathbf{r})$, including the many-particle wave function and all observables. Thus, via theorem 2.2.1, if the ground state electron density is given, one has enough information to construct the external potential, the total energy, and all desirable observables. The mathematical mapping of any test density, ρ', to a total energy is given in functional notation as

$$E[\rho'] = \int V^{\text{ext}}(\mathbf{r}) \rho'(\mathbf{r}) d\mathbf{r} + F[\rho']. \tag{2.8}$$

The second theorem provides instructions on how to arrive at the correct density via use of the variational principle:

Theorem 2.2.2 $E[\rho']$ *assumes its minimum value when the electron density is its correct value; i.e.,* $\rho'(\mathbf{r}) = \rho(\mathbf{r})$.

The importance of this statement is in allowing one to search for the correct density by use of the total energy as an indicative metric—once this value is at its global minimum, the density used is known to be the true ground state density of the system. The remaining task, then, is to determine what functional to use as $F[\rho]$, a point best summarized by the original statement of Hohenberg and Kohn,

> "If $F[\rho]$ were a known and sufficiently simple functional of ρ, the problem of determining the ground state energy and density in a given external potential would be rather easy since it requires merely the minimization of a functional of the three-dimensional density function. The major part of the complexities of the many-electron problems are associated with the determination of the universal functional $F[\rho]$."

This problem was to be addressed one year later with the work of Kohn and Sham [33]. The proposed form for $F[\rho]$ was separated into three partitions,

$$F[\rho] = T[\rho] + \frac{1}{4\pi\varepsilon_0}\frac{e^2}{2}\int \frac{\rho(\mathbf{r})\rho(\mathbf{r}')}{|\mathbf{r}-\mathbf{r}'|}d\mathbf{r}' + E^{\mathrm{xc}}[\rho]. \tag{2.9}$$

Each term was to represent a physical energy contribution. The first term in the above equation is the total kinetic energy. The second term is known as the Hartree energy which describes the simple electrostatic energy between electrons. The third term is the exchange-correlation energy, a combination of two problematic quantities: the exchange energy, a consequence of the electrons being indistinguishable particles subject to exchange symmetry, and the energy related to the dynamic correlation interaction resulting from the instantaneous Coulomb repulsion between electrons lacking from the Hartree term.

With the above description and use of the variational principle, Kohn and Sham showed that one could obtain the density which minimizes the total energy functional by solving the one-particle TISE for a set of fictitious non-interacting particles, Φ_n,

$$H^{\mathrm{KS}}\Phi_n(\mathbf{r}) = \epsilon_n \Phi_n(\mathbf{r}) \tag{2.10}$$

and setting

$$\rho(\mathbf{r}) = \sum_{n=1}^{N_{\mathrm{occupied}}} |\Phi_n(\mathbf{r})|^2. \tag{2.11}$$

The latter is the result of assigning the occupied, so-called, Kohn–Sham orbitals as the single-particle wave functions comprising a Slater determinant. Importantly, the Kohn-Sham Hamiltonian used in (2.10) is defined using the functional derivative of $F[\rho]$ with respect to the density,

$$H^{\mathrm{KS}} = -\frac{\hbar^2}{2m}\nabla^2 + V^{\mathrm{H}}[\rho](\mathbf{r}) + V^{\mathrm{xc}}[\rho](\mathbf{r}) + V^{\mathrm{ext}}(\mathbf{r}). \tag{2.12}$$

Here, V^{H} is the Hartree potential,

$$V^{\mathrm{H}}[\rho](\mathbf{r}) = \frac{e^2}{4\pi\varepsilon_0}\int \frac{\rho(\mathbf{r}')}{|\mathbf{r}-\mathbf{r}'|}d\mathbf{r}', \tag{2.13}$$

V^{xc} is the exchange-correlation potential,

$$V^{\mathrm{xc}}[\rho](\mathbf{r}) = \frac{\delta E^{\mathrm{xc}}[\rho]}{\delta[\rho(\mathbf{r})]}, \tag{2.14}$$

and the term $-\frac{\hbar^2}{2m}\nabla^2$ is related to the kinetic energy of the Kohn-Sham system of non-interacting electrons. Corrections to the kinetic energy are included in the definition of the correlation part of $E^{\mathrm{xc}}[\rho]$. Equation (2.10) may be used to simplify the expression for the total energy, making use of the Kohn–Sham eigenvalues, ϵ_n,

$$E = \sum_{n=1}^{N_{\text{occupied}}} \epsilon_n + \int \left(\frac{1}{2} V^{\text{H}}(\mathbf{r}) - V^{\text{xc}}(\mathbf{r}) \right) \rho(\mathbf{r}) d\mathbf{r} + E^{\text{xc}}[\rho]. \tag{2.15}$$

This is the scheme used today to solve for the electronic density. In practice, this search for the electron density is done self-consistently. One begins by initializing the density using some guess, this density is used to calculate the form of the Kohn–Sham Hamiltonian, and the orbitals are obtained by solving what is now known as the Kohn–Sham equations. If the density defined by these orbitals is equal to that which was input originally, then the solution is said to be self-consistent and one has arrived at the exact ground state density. If not, then this density is used as a new input and the above steps are repeated.

Up until this point, all treatment of the many-particle system has been exact; however, remaining to be addressed is the form of the exchange-correlation functional, $E^{\text{xc}}[\rho]$. The exact form of this functional is not known and, thus, approximations are necessary in order to provide reasonable solutions using the above described method. Many such approximations have been suggested since DFT's inception.

The most simplistic choice is that of the local density approximation (LDA). Here, the exchange-correlation functional is only dependent on the density at each point in space. The functional may be expressed as

$$E^{\text{xc}}_{\text{LDA}} = \int \rho(\mathbf{r}) \epsilon_{\text{xc}}(\rho) d\mathbf{r}, \tag{2.16}$$

where ϵ_{xc} is described as the exchange-correlation energy per particle of a homogeneous electron gas of charge density ρ. The associated potential may be separated into two terms,

$$V^{\text{xc}}_{\text{LDA}}[\rho](\mathbf{r}) = V^{\text{x}}_{\text{HEG}}[\rho] + V^{\text{c}}_{\text{HEG}}[\rho]. \tag{2.17}$$

The exchange term, V^{x}, is known exactly for the homogeneous electron gas,

$$V^{\mathrm{x}}_{\mathrm{HEG}} = -\left(\frac{3\rho}{\pi}\right)^{1/3}. \tag{2.18}$$

The correlation term, however, must be treated by approximation, even for this simplified case. Accurate Monte Carlo simulations were performed by Ceperley and Alder [119] on the homogeneous electron gas in 1980. This data was then parametrized by Perdew and Zunger [120] the next year in order to provide the following popular form for this functional:

$$V^{\mathrm{c}}_{\mathrm{HEG}}[\rho](\mathbf{r}) \approx \begin{cases} \gamma_U \frac{1+\frac{7}{6}\beta_{1U}\sqrt{r_s}+\frac{4}{3}\beta_{2U}r_s}{(1+\beta_{1U}\sqrt{r_s}+\beta_{2U}r_s)^2}, & r_s \geq 1 \\ \mathrm{A}_U \ln r_s + (\mathrm{B}_U - \frac{1}{3}\mathrm{A}_U) + \frac{2}{3}\mathrm{C}_U r_s \ln r_s + \frac{1}{3}(2\mathrm{D}_U - \mathrm{C}_U)r_s, & r_s < 1 \end{cases}, \tag{2.19}$$

where $r_s = (3/4\pi\rho)^{1/3}$ and the numeric constants are $\gamma_U = -0.1423$, $\beta_{1U} = 1.0529$, $\beta_{2U} = 0.3334$, $\mathrm{A}_U = 0.0311$, $\mathrm{B}_U = -0.048$, $\mathrm{C}_U = 0.002$, and $\mathrm{D}_U = -0.0116$, each in atomic units.

Increasingly sophisticated approximations for the exchange-correlation functional have been introduced throughout DFT's lifetime. This progression is, today, commonly referred to as the Jacob's ladder of density functional approximations [121]. LDA is positioned at the bottom rung. The next highest is considered to be the generalized gradient approximation [122], which accounts for inhomogeneities by including a dependence on the density's gradient; a very popular implementation of this form is the Perdew-Burke-Ernzerhof (PBE) functional [123]. Higher still are the meta-generalized gradient approximation [124], which takes into account the kinetic energy density, and orbital-dependent functionals. Despite the ever-growing library of functionals, there is no all-inclusive solution. Oftentimes, the functional used is that with the simplest form which is expected to perform adequately for the system in question.

2.3 Time-Dependent Density Functional Theory Formalism

The theorems of Hohenberg and Kohn proved that the ground state density uniquely determined the encompassing external potential and, thus, the entirety of the system in question. This development allowed for the study of complex electronic systems in equilibrium. However, it was later shown that the simulation of time-dependent phenomenon, specifically molecular dynamics, could also benefit from this description via an improved representation of the electron-nuclei interaction. In 1885, Car and Parrinello introduced their groundbreaking scheme for incorporating a density functional ground state calculation within molecular dynamics [125], and later, in 1995, the now more common Born–Openheimer molecular dynamics scheme was introduced [126]. While these methods allowed for the enhanced study of nuclear vibrations and femtosecond scale dynamics, the electronic description was kept purely adiabatic or described using fictitious dynamical variables.

In 1984, the theorems of Hohenberg and Kohn were extended to time-dependent densities and external potentials by that of Runge and Gross [41]:

Theorem 2.3.1 *The exact time-dependent density of the system can be computed from*

$$\rho(\mathbf{r}, t) = \sum_{n=1}^{N_{\text{occupied}}} |\Phi_n(\mathbf{r}, t)|^2, \tag{2.20}$$

where the single-particle (Kohn–Sham) orbitals, $\Phi_n(\mathbf{r}, t)$*, fulfill the time-dependent Schrödinger equation*

$$i\hbar \frac{\partial}{\partial t} \Phi_n(\mathbf{r}, t) = \left[-\frac{\hbar^2}{2m} \nabla^2 + V^{\text{eff}}[\rho](\mathbf{r}, t) \right] \Phi_n(\mathbf{r}, t) \tag{2.21}$$

with an effective one-particle potential given by

$$V^{\text{eff}}[\rho](\mathbf{r},t) = V^{\text{ext}}(\mathbf{r},t) + \frac{e^2}{4\pi\varepsilon_0}\int \frac{\rho(\mathbf{r}',t)}{|\mathbf{r}-\mathbf{r}'|}d\mathbf{r}' + V^{\text{xc}}[\rho](\mathbf{r},t). \tag{2.22}$$

This theorem was built from the assertion that, analogous to theorem 2.2.1, the time-dependent external potential is also uniquely determined by the time-dependent density. This extension of the density functional formalism allows for the straightforward determination of the time-dependent density and resulting observables via propagation of the Kohn-Sham orbitals using well established techniques of solving the single-particle TDSE. This new set of equations describing the orbitals is known as the time-dependent Kohn–Sham (TDKS) equations. The probability current density may be constructed from the orbitals as

$$\mathbf{j}(\mathbf{r},t) = \frac{\hbar}{2mi}\sum_{n=1}^{N_{\text{occupied}}} \left(\Phi_n^*\nabla\Phi_n - \Phi_n\nabla\Phi_n^*\right). \tag{2.23}$$

As in the case of the ground state theory, approximate forms are necessary for describing the now time-dependent exchange-correlation functional. It is well known that an exact form of this functional must include memory effects; that is, the functional at time t should take into account the history of the density, $\rho(\mathbf{r}, t < t_{\text{final}})$, the initial interacting many-body state, $\Psi(r1...rN, t = 0)$, and the initial Kohn–Sham state, $\Phi_n(\mathbf{r}, t = 0)$ [127, 128]. Nevertheless, adiabatic approximations, in which memory effects are ignored and the functional is entirely evaluated at each point in time according to the associated instantaneous density, work well in describing many time-dependent electronic phenomenon. It is common practice to prepare the initial Kohn–Sham state ahead of time via a DFT calculation and to describe the time-dependent exchange correlation potential with such an adiabatic approximation. One such popular choice is that of the adiabatic local density approximation (ALDA) in which the exchange-correlation potential at any given point in time, t, is equal to the above described LDA exchange-correlation potential used in DFT, with the density at that same time used as the input:

$$V^{\mathrm{xc}}_{\mathrm{ALDA}}[\rho](\mathbf{r},t) = V^{\mathrm{xc}}_{\mathrm{LDA}}[\rho(t)](\mathbf{r}). \tag{2.24}$$

An overwhelming amount of TDDFT studies use this functional due to its simplicity and effectiveness. It is worth noting that, in the same manner, any of the above described exchange-correlation functionals from DFT may be used in TDDFT as adiabatic analogues. While the adiabatic choice has been shown to cause the absence double-excitations [129, 130], progress has been made in establishing theories related to TDDFT which are capable of producing such states [131].

For the effects of small perturbations, such as in the case of spectroscopy studies which make use of weak probes to study the spectral response of a system, one may simplify the description of a time-dependent observable using linear response TDDFT (LR-TDDFT) [132]. This popular method makes use of the first-order perturbation theory instead of solving for the entirety of the solution to the TDKS equations. Such calculations can be very advantageous as they directly determine the change of a certain variable of interest rather than describing the change in the wave function and are, therefore, computationally inexpensive. In this work, the effects of strong laser fields are studied; therefore, LR-TDDFT cannot be used to describe the induced dynamics. Instead, real-time TDDFT (RT-TDDFT) [133] is employed throughout this thesis, in which the TDKS equations are solved via real-time propagation of the Kohn–Sham orbitals. Methods for this propagation are discussed in detail in Chapter 5.

2.4 Quantum Dynamics in External Fields

In order to describe laser-driven phenomenon using TDDFT, one must introduce external electromagnetic fields within the Kohn-Sham Hamiltonian. One begins by listing Maxwell's microscopic equations which govern such fields in vacuum. Given in SI units, these equations are the following:

$$\nabla \cdot \mathbf{E} = \frac{\rho_{\text{charge}}}{\varepsilon_0} \tag{2.25}$$

$$\nabla \cdot \mathbf{B} = 0 \tag{2.26}$$

$$\nabla \times \mathbf{E} = -\frac{\partial \mathbf{B}}{\partial t} \tag{2.27}$$

$$\nabla \times \mathbf{B} = \mu_0 \left(\mathbf{J}_{\text{charge}} + \varepsilon_0 \frac{\partial \mathbf{E}}{\partial t} \right). \tag{2.28}$$

Here, $\mathbf{E}$ and $\mathbf{B}$ are the time-dependent electric and magnetic fields, respectively, ρ_{charge} is the total charge density, and $\mathbf{J}_{\text{charge}}$ is the total charge current density. It is important to note that these densities are not that of the above described probability densities, ρ and $\mathbf{j}$, in the TDDFT formalism. Instead, they are related in that, on average, one would expect that $\langle \rho_{\text{charge}} \rangle = -e\rho + e \sum_a \delta(\mathbf{r} - \mathbf{R}_a)$ and $\langle \mathbf{J}_{\text{charge}} \rangle = -e\mathbf{j}$, where the coordinates $\mathbf{R}_a$ represent the semiclassical locations of the nuclei which are assumed to exhibit negligible velocities. While these expressions illustrate how moving charged particles give rise to electromagnetic fields, the complimentary inverted effect is made clear by the Lorentz force law,

$$\mathbf{F} = q\mathbf{E} + q\mathbf{v} \times \mathbf{B}, \tag{2.29}$$

which describes the force felt on a moving particle of charge q and velocity $\mathbf{v}$.

One may reformulate Maxwell's equations using descriptions of the electric scalar potential, φ, and the magnetic vector potential, $\mathbf{A}$ using the following relationships with $\mathbf{E}$ and $\mathbf{B}$:

$$\mathbf{B} = \nabla \times \mathbf{A} \tag{2.30}$$

$$\mathbf{E} = -\nabla\varphi - \frac{\partial \mathbf{A}}{\partial t}. \tag{2.31}$$

Plugging this transformation into eqs. (2.25)–(2.28) results in

$$-\nabla^2\varphi - \frac{\partial}{\partial t}\left(\nabla \cdot \mathbf{A}\right) = \frac{\rho_{\text{charge}}}{\varepsilon_0} \tag{2.32}$$

$$\varepsilon_0\mu_0\frac{\partial^2 \mathbf{A}}{\partial t^2} - \nabla^2\mathbf{A} = \mu_0\mathbf{J}_{\text{charge}} - \nabla\left(\nabla \cdot \mathbf{A} + \varepsilon_0\mu_0\frac{\partial\varphi}{\partial t}\right). \tag{2.33}$$

In order to simplify these expressions, one may take advantage of the gauge freedom of the potential description of electromagnetic fields. It can be shown that the physical fields, $\mathbf{E}$ and $\mathbf{B}$, remain unchanged under the transformations $\mathbf{A} \to \mathbf{A} + \nabla\lambda$ and $\varphi \to \varphi - \partial\lambda/\partial t$, where $\lambda(\mathbf{r}, t)$ is an arbitrary function of space and time. A common choice is to apply what is known as the Coulomb gauge, which asserts that

$$\nabla \cdot \mathbf{A}(\mathbf{r}, t) = 0. \tag{2.34}$$

Furthermore, if one assumes that there are no sources of the external field, ρ_{charge}, present in the region of interest, such as when dealing with an external laser field, then $\varphi = 0$. This leads to a simplified set of equations,

$$\mathbf{B} = \nabla \times \mathbf{A} \tag{2.35}$$

$$\mathbf{E} = -\frac{\partial \mathbf{A}}{\partial t}. \tag{2.36}$$

$$\varepsilon_0\frac{\partial^2 \mathbf{A}}{\partial t^2} = \mathbf{J}_{\text{charge}}. \tag{2.37}$$

In order to incorporate electromagnetic fields within the TDDFT formalism, one needs to arrive at a Hamiltonian addressing their interaction with charged particles. This may be accomplished by deriving a Lagrangian which results in the force described in (2.29) and a subsequent Hamiltonian. The following Lagrangian, making use of eqs. (2.30) and (2.31), can be shown via the Euler-Lagrange equations to be consistent with the Lorentz force law regardless of the choice of gauge:

$$L = \frac{1}{2}m|\mathbf{v}|^2 - q\varphi(\mathbf{r}, t) + q\mathbf{v} \cdot \mathbf{A}(\mathbf{r}, t). \tag{2.38}$$

A Legendre transformation is then used in order to obtain the Hamiltonian

$$H = \frac{1}{2m}\left(\mathbf{p} - q\mathbf{A}\right)^2 + q\varphi, \tag{2.39}$$

where $\mathbf{p}$ is the conjugate variable to position. Using the above simplifications, the scalar potential is dropped, $\varphi = 0$, and the final electromagnetic Hamiltonian of interest is

$$H = \frac{1}{2m}\left(\mathbf{p} - q\mathbf{A}\right)^2. \tag{2.40}$$

When studying light-matter interactions on the nano-scale, one often takes advantage of the dipole approximation. The employed assumption is that the length scales associated with the target system are significantly smaller than the wavelength of the electric field. This leads to the simplification of considering only homogeneous fields; i.e., the vector potential is no longer a function of the spatial coordinate. Thus, the magnetic field component of the incident laser is zero, since $\mathbf{B} = \nabla \times \mathbf{A} = \mathbf{0}$. Expansion terms such as the magnetic dipole moment, electric quadrupole moment, etc., are ignored. This approximation is well-suited for many studies on the molecular scale and is employed throughout this thesis.

One may transform the classical Hamiltonian of Eq. (2.40) into one suitable for describing wave functions by the introduction of the quantum mechanical momentum operator in real space, $\mathbf{p} \rightarrow \hat{\mathbf{p}} - i\hbar\nabla$. Furthermore, when describing electronic dynamics, one may set $q = -e$. Using these changes, one arrives at a Hamiltonian which describes the free motion of an electron subject to an external electromagnetic field,

$$H^{\mathrm{vel}} = \frac{1}{2m}\left(-i\hbar\nabla + e\mathbf{A}\right)^2. \tag{2.41}$$

The subsequent TDSE, then, is often called the velocity gauge representation for the field-influenced wave function,

$$i\hbar\frac{\partial}{\partial t}\psi(\mathbf{r},t) = \frac{1}{2m}\left(-i\hbar\nabla + e\mathbf{A}\right)^2\psi(\mathbf{r},t), \tag{2.42}$$

and Eq. (2.41), the velocity gauge Hamiltonian. This may also be thought of as the regular TDSE with an external potential of

$$V^{\mathrm{EM}}(\mathbf{r},t) = \frac{e^2}{2m}|\mathbf{A}|^2 - \frac{i\hbar e}{m}\mathbf{A}\cdot\nabla. \tag{2.43}$$

A popular alternative representation to the velocity gauge is that of the length gauge representation. Here, one factors the wave function into

$$\psi(\mathbf{r},t) = \phi(\mathbf{r},t)\mathrm{e}^{-i\mathbf{A}(t)\cdot\mathbf{r}/\hbar}. \tag{2.44}$$

By plugging this form into Eq. (2.42) and making use of Eq. (2.36), one arrives at

$$i\hbar\frac{\partial}{\partial t}\phi(\mathbf{r},t) = \left[-\frac{\hbar^2}{2m}\nabla^2 + \mathbf{E}(t)\cdot\mathbf{r}\right]\phi(\mathbf{r},t). \tag{2.45}$$

The length gauge Hamiltonian, then, is given as

$$H^{\mathrm{len}} = -\frac{\hbar^2}{2m}\nabla^2 + \mathbf{E}(t)\cdot\mathbf{r} \tag{2.46}$$

In this way, the time-dependent ϕ functions may be solved for as easily as the velocity gauge wave functions, ψ. This form is often preferred due to its straightforward depiction of the electromagnetic potential which, in this gauge, takes the form

$$V^{\mathrm{EM}}(\mathbf{r},t) = \mathbf{E}(t)\cdot\mathbf{r}. \tag{2.47}$$

By adding the Kohn–Sham effective potential, Eq. (2.22), either of these representations may be used within TDDFT in order to describe the evolution of the Kohn–Sham orbitals subject to an external field. The construction of the current density is modified due to the new representation of the Hamiltonian:

$$\mathbf{j}(\mathbf{r}, t) = \frac{\hbar}{2mi} \sum_{n=1}^{N_{\text{occupied}}} \left(\Phi_n^* \nabla \Phi_n - \Phi_n \nabla \Phi_n^*\right) + \frac{e}{m} \rho \mathbf{A}. \tag{2.48}$$

It must be noted, however, that outside of the dipole approximation, corrections are necessary for formally exact representations of the time-dependent electron density when describing periodic systems. Ghosh and Dhara [134] were the first to provide a formal proof of time-dependent current-DFT (TDCDFT) which considers current the basic variable, rather than density. This theory asserts that the Runge–Gross theorem, theorem 2.3.1, only holds true for cases in which the electron density reaches zero at some boundary. For finite systems such as atoms or molecules, this requirement poses no difficulty. It also holds true for periodic systems, given that the external potential is similarly periodic. However, in the case of homogeneous fields applied to a periodic system, this condition is not met, and TDCDFT shows that an additional exchange-correlation contribution to the vector potential must be included [135]. As most uses of TDDFT take advantage of the dipole approximation, this correction is rarely needed and is neglected throughout this thesis. Nevertheless, the methods introduced in the following chapters may be applied within a TDCDFT formalism.

2.5 Pseudopotentials

The pseudopotential approximation is meant to simplify the representation of atomic systems by replacing the complicated interactions with nuclei and core electrons described by the exact Hamiltonian with a pseudopotential operator. The purpose of this operator is to effectively represent the presence of these interactions in a phenomenological manner. The motivation for this simplification is in avoiding the computationally costly and complex all-electron Hamiltonian in favor of an approximate representation for the valence electron wave function, which is expected to remain accurate in regions of interest. This concept is made possible due to the principle that only the valence electrons are considered chemically active, that is, only these electrons participate in determining the properties and reactions of any given atom within a greater system.

One begins by describing the Hamiltonian for the valence electrons, which resembles that of Eq. (2.2):

$$H = \sum_{i=1}^{N} T_i + \sum_{i=1}^{N} V^{\text{ion}}(\mathbf{r}_i) + \sum_{i<j}^{N_{\text{v}}} V^{\text{ee}}(\mathbf{r}_i, \mathbf{r}_j). \tag{2.49}$$

Here, V^{nuc} has been replaced with V^{ion} which describes the interaction of the valence electrons with the combination of nuclei and core electrons, or ions. The two-body Coulomb potential, V^{ee} is now only used to manage the interaction of valence electrons and can be approached using the DFT formalism described above.

The simplest and most popular application of pseudopotentials is to represent V^{ion} using the Kleinmann and Bylander separable form [136]:

$$V^{\text{ion}} = V^{\text{pp,local}}(\mathbf{r}) + V^{\text{pp,nonlocal}}(\mathbf{r}, \mathbf{r}') \tag{2.50}$$

which describes a local and a nonlocal contribution. The local part,

$$V^{\text{pp,local}}(\mathbf{r}) = \sum_{a=1}^{N_{\text{atoms}}} V_a^{\text{pp,local}}(|\boldsymbol{\rho}_a|), \tag{2.51}$$

is only dependent upon the magnitude of the displacement from the ion location, $\boldsymbol{\rho}_a = \mathbf{r} - \mathbf{R}_a$, and extends beyond the core regions with a long range part of the form $-Z_a/r$, where Z_a is the charge of the ion. The nonlocal part is defined as

$$V^{\text{pp,nonlocal}}(\mathbf{r}, \mathbf{r}') = \sum_{a=1}^{N_{\text{atoms}}} \sum_{l} \sum_{m=-l}^{l} \frac{\langle \mathbf{r} | \Delta V_{a,l}^{\text{nl}} | \psi_{a,l,m}^{\text{ps}} \rangle \, \langle \psi_{a,l,m}^{\text{ps}} | \Delta V_{a,l}^{\text{nl}} | \mathbf{r}' \rangle}{\langle \psi_{a,l,m}^{\text{ps}} | \Delta V_{a,l}^{\text{nl}} | \psi_{a,l,m}^{\text{ps}} \rangle}, \tag{2.52}$$

where $\Delta V^{\mathrm{nl}}_{a,l}(\boldsymbol{\rho}_a) = V_{a,l}(|\boldsymbol{\rho}_a|) - V^{\mathrm{pp,local}}_a(|\boldsymbol{\rho}_a|)$. The functions $V_{a,l}$ are the l angular momentum components of the nonlocal part of the pseudopotential and $\psi^{\mathrm{ps}}_{a,l,m}$ are the so-called node-free atomic pseudo wave functions, represented as the product of a radial part and spherical harmonics as $\psi^{\mathrm{ps}}_{a,l,m}(\mathbf{r}) = R^{\mathrm{ps}}_{a,l}(|\boldsymbol{\rho}_a|)Y_{lm}(\hat{\boldsymbol{\rho}}_a)$. The nonlocal term of the pseudopotential is often only considered within a cutoff radius, r^a_c, near the core region of each atom in order to limit computational expenses.

The functions $V^{\mathrm{pp,local}}$, $V_{a,l}$, and $R^{\mathrm{ps}}_{a,l}$ may be determined by performing an all-electron DFT calculation, projecting out the core electron states, and fitting a potential for the valence states. After they are determined once, these functions may be used to represent ionic core potentials as pseudopotentials in a wide variety of static or time-dependent simulations. Many schemes exist for the description of these functions. One of the most popular methods is that of Troullier and Martins [137] which produces norm-conserving pseduopotentials. This means that the radial part of the atomic pseudo wave function is identical to that of the all-electron wave function for any particular atom, $R^{\mathrm{ps}}_{a,l}(r)$, outside of the cutoff radius,

$$R^{\mathrm{ps}}_{a,l}(r) = R^{\mathrm{ae}}_a(r) \quad \text{for} \quad r \geq r^a_c \tag{2.53}$$

and that the norm of the radial part is conserved within the cutoff region, that is,

$$\int_0^{r_c} |R^{\mathrm{ps}}_{a,l}(r)|^2 r^2 dr = \int_0^{r^a_c} |R^{\mathrm{ae}}_a(r)|^2 r^2 dr. \tag{2.54}$$

These conditions allow for proper numerical convergence with reasonable computational efficiency. This choice of pseudopotential is used throughout this thesis.

Lastly, in the case of time-dependent studies, an additional term must be included in the definition of the current resulting from the nonlocal pseudopotential [138, 139]. Here, the corrected expression is

$$\mathbf{j}(\mathbf{r},t) = \frac{\hbar}{2mi} \sum_{n=1}^{N_{\mathrm{occupied}}} (\Phi^*_n \nabla \Phi_n - \Phi_n \nabla \Phi^*_n) + \frac{e}{m}\rho\mathbf{A} + \mathbf{j}_{\mathrm{NL}}(\mathbf{r},t), \tag{2.55}$$

where

$$\mathbf{j}_{\mathrm{NL}}(\mathbf{r},t) = \frac{1}{i\hbar}\sum_{n=1}^{N_{\mathrm{occupied}}}\int \Phi_n^*(\mathbf{r},t)\left[\mathbf{r}V^{\mathrm{pp,nonlocal}}(\mathbf{r},\mathbf{r}') - V^{\mathrm{pp,nonlocal}}(\mathbf{r},\mathbf{r}')\mathbf{r}'\right]\Phi_n(\mathbf{r}',t)d\mathbf{r}'. \quad (2.56)$$

2.6 Bloch Theory

In the case of zero-temperature bulk solids, ions are arranged within repeating Wigner–Seitz cells defined by the the associated Bravais lattice [140]. In the following discussion, these periodically repeating unit cells are assumed to extend infinitely; i.e., surface effects are ignored. The translational symmetry of the resulting potential is defined using the crystal lattice vectors, $\mathbf{R}_n^{\mathrm{c}}$,

$$V^{\mathrm{ion}}(\mathbf{r}+\mathbf{R}_n^{\mathrm{c}}) = V^{\mathrm{ion}}(\mathbf{r}). \quad (2.57)$$

This relationship shows that the potential, and, subsequently, all aspects of the system, remain invariant for a translation by $\mathbf{R}_n^{\mathrm{c}}$. These vectors are constructed as integer combinations of the three primitive vectors, $(\mathbf{a}_1, \mathbf{a}_2, \mathbf{a}_3)$, defining the volume of a single unit cell:

$$\mathbf{R}_n^{\mathrm{c}} = n_1\mathbf{a}_1 + n_2\mathbf{a}_2 + n_3\mathbf{a}_3, \quad (2.58)$$

where n indicates a unique combination of n_1, n_2, and n_3.

Electrons subject to such a potential are known as Bloch electrons, named for Felix Bloch who provided the mathematical description of the periodic Hamiltonian eigenstate [27]. Bloch's theorem may be stated as the following [141]:

Theorem 2.6.1 *The eigenstates of the Hamiltonian describing a perfect crystal lattice may be described as*

$$\psi_{n\mathbf{k}}(\mathbf{r}) = \mathrm{e}^{i\mathbf{k}\cdot\mathbf{r}}u_{n\mathbf{k}}(\mathbf{r}), \quad (2.59)$$

where $u_{n\mathbf{k}}(\mathbf{r})$ are complex functions of the same translational symmetric as the lattice; that *is,*

$$u_{n\mathbf{k}}(\mathbf{r}+\mathbf{R}_n^{\mathrm{c}}) = u_{n\mathbf{k}}(\mathbf{r}). \tag{2.60}$$

Here, the reciprocal lattice vectors, $\mathbf{k}$, are not to be considered indicative of momentum eigenstates, since $\hat{\mathbf{p}}\psi_{n\mathbf{k}}(\mathbf{r}) \neq \hbar\mathbf{k}\psi_{n\mathbf{k}}$ as might be intuitive. Instead, $\hbar\mathbf{k}$ is called the crystal momentum. For any value of crystal momentum, the single particle TISE has multiple solutions indicated by subscript n. The associated eigenvalues $E_{n\mathbf{k}}$ vary continuously for fixed values of integer n and are described as bands.

The Bloch wave functions similarly exhibit symmetry by translation in the reciprocal space,

$$\mathrm{e}^{i(\mathbf{k}+\mathbf{K}_m)\cdot\mathbf{r}}u_{n(\mathbf{k}+\mathbf{K}_m)}(\mathbf{r}) = \mathrm{e}^{i\mathbf{k}\cdot\mathbf{r}}u_{n\mathbf{k}}(\mathbf{r}). \tag{2.61}$$

Here, $\mathbf{K}_m$ represents reciprocal lattice vectors which may be defined by reciprocal primitive vectors, $(\mathbf{b}_1, \mathbf{b}_2, \mathbf{b}_3)$, as

$$\mathbf{K}_m = m_1\mathbf{b}_1 + m_2\mathbf{b}_2 + m_3\mathbf{b}_3. \tag{2.62}$$

These reciprocal primitive vectors may be related to the direct primitive vectors in the following manner:

$$\begin{aligned}
\mathbf{b}_1 &= 2\pi\frac{\mathbf{a}_2\times\mathbf{a}_3}{\mathbf{a}_1\cdot(\mathbf{a}_2\times\mathbf{a}_3)}\\
\mathbf{b}_2 &= 2\pi\frac{\mathbf{a}_3\times\mathbf{a}_1}{\mathbf{a}_2\cdot(\mathbf{a}_3\times\mathbf{a}_1)}\\
\mathbf{b}_3 &= 2\pi\frac{\mathbf{a}_1\times\mathbf{a}_2}{\mathbf{a}_3\cdot(\mathbf{a}_1\times\mathbf{a}_2)}.
\end{aligned} \tag{2.63}$$

By defining a matrix with column vectors as the direct primitive vectors, $[\mathbf{a}_1\mathbf{a}_2\mathbf{a}_3]$, one may recast Eq. (2.63) as

$$[\mathbf{b}_1\mathbf{b}_2\mathbf{b}_3] = 2\pi[\mathbf{a}_1\mathbf{a}_2\mathbf{a}_3]^{-1} \tag{2.64}$$

In this way, any choice of Bravais lattice defining the arrangement of ions in a crystal may be used to also define an equivalently representative reciprocal Bravais lattice.

Due to the above described reciprocal lattice symmetry of the Bloch wave functions, one may fully describe the electronic system by considering values of $\mathbf{k}$ which lie within the first Brillouin zone. In order to define this volume in reciprocal space, one must first choose a reference origin, which is set as $\mathbf{K}_m = \mathbf{0}$ for simplicity. The first Brillouin zone is then a Wigner–Seitz primitive cell of the reciprocal lattice and is defined as the volume which encompasses this origin, with boundaries defined by the planes perpendicularly bisecting the lines connecting the origin to surrounding reciprocal lattice points. In other words, the first Brillouin zone contains values of $\mathbf{k}$ which are closer to the reference point, $\mathbf{K}_m = \mathbf{0}$, than any other values for $\mathbf{K}_m$. One may similarly define higher order Brillouin zones of equal volume which consist of $\mathbf{k}$ values increasingly distant from the designated origin. Furthermore, one may use intrinsic symmetries of the lattice being represented to define an irreducible Brillouin zone, which is the smallest subset of $\mathbf{k}$ values which uniquely represent the full electronic solution.

The Bloch theory of electron wave functions may be readily described by DFT. The Kohn–Sham orbitals are now distinguished by the same two quantum numbers as above and are of the same form as the Bloch wave function; that is,

$$\Phi_{n\mathbf{k}}(\mathbf{r}) = \mathrm{e}^{i\mathbf{k}\cdot\mathbf{r}} u_{n\mathbf{k}}(\mathbf{r}) \tag{2.65}$$

and the Kohn–Sham single particle eigenvalues are $\epsilon_{n\mathbf{k}}$. In this modification of DFT, one defines the particle density by integrating over the first Brillouin zone,

$$\rho(\mathbf{r}) = \int_{\mathrm{BZ}} \sum_{n=1}^{N_{\mathrm{occupied}}} |\Phi_{n\mathbf{k}}(\mathbf{r})|^2 d\mathbf{k}, \tag{2.66}$$

and similarly defines the sum over single particle eigenvalues found in Eq. (2.15) as

$$\int_{\mathrm{BZ}} \sum_{n=1}^{N_{\mathrm{occupied}}} \epsilon_{n\mathbf{k}} d\mathbf{k}. \tag{2.67}$$

In practice, the same problem that arises when attempting to numerically represent integrals over continuous variable $\mathbf{r}$ occurs in this case of representing integrals over the continuous variable $\mathbf{k}$. Therefore, one must, again, discretize this domain. The most common practice is to transform integrals over the first Brillouin zone into weighted sums, $\int_{\mathrm{BZ}} d\mathbf{k} \rightarrow \sum_{\mathbf{k}} w_{\mathbf{k}}$, over discrete values of $\mathbf{k}$ arranged on a grid. These discrete values are known in the literature as $\mathbf{k}$-points.

In the case of TDDFT simulations of laser-matter interactions within solids, the velocity gauge representation for the orbitals is necessary in order to preserve the translational symmetry of the Hamiltonian. Thus, the electric field is included as a time-dependent vector potential according to the time-dependent Hamiltonian

$$H(t) = H^{\mathrm{vel}}(t) + V^{\mathrm{eff}}(t), \tag{2.68}$$

where the velocity gauge Hamiltonian is defined in Eq. (2.41) and the effective potential is that of Eq. (2.22). For the case of $\mathbf{A}(t=0) = \mathbf{0}$, it is common to consider the crystal momentum as time-dependent and defined as $\hbar\mathbf{k}(t) = \hbar\mathbf{k}_0 + e\mathbf{A}(t)$, where $\hbar\mathbf{k}_0$ is the crystal momentum at $t = 0$. This leads to a simple computational form since the initial crystal momentum and time-dependent vector potential appear together in this way in many calculations.

Chapter 3

BASIS REPRESENTATIONS

3.1 Ritz Method

Because computers are unable to represent continuous functions, discretization is necessary when a numerical representation of the wave function is desirable, such as in the case of most DFT and RT-TDDFT approaches. This is often addressed by means of representing the wave function, as well as any other functions, as linear combinations of basis functions, ϕ_i,

$$\psi(\mathbf{r}) = \sum_{i=1}^{N_{\mathrm{BF}}} c_i \phi_i(\mathbf{r}). \tag{3.1}$$

This is possible due to the fact that in the equations relevant to quantum mechanics, one is solving equations involving linear operators such as in the case of differentiation or integration. In this way, the expansion coefficients, c_i fully represent the wave function in a discrete way that can be stored on a computer and used to recreate the complete wave function with knowledge of the predefined basis set. The basis size, N_{BF}, indicates the amount of memory needed to store a function as well as the processing time needed to apply a numerical method. As such, this number dictates the computational expense of a simulation program.

While Eq. (3.1) is only exact for basis sets which comprise a complete Hilbert space, truncating the basis is necessary for reasonable computational implementation and can still provide satisfactory numerical accuracy. The balance of basis size and accuracy is a common topic of simulation improvement. By choosing basis functions which reflect the symmetries of Hamiltonian of interest, one may decrease the basis size needed to reach a desired level of accuracy. Investigation of novel bases which decrease the required basis size is a common topic of research which allows for the improvement of computational efficiency and, therefore, the accessibility of simulation programs. In the interest of time-dependent simulations, one usually must first test candidate bases via their ability to represent the static ground state case.

In order to solve the TDSE or Kohn–Sham equations using such a basis expansion, one typically employs the Ritz method [142, 143]. This method uses Eq. (3.1) as the form of a trial wave function to be used alongside the variational principle. The variational principle asserts that the ground state energy, E_0, associated with a wave function, ψ, by the TISE, $H\psi = E_0\psi$, will exhibit the following behavior:

$$E_0 \leq \epsilon, \tag{3.2}$$

where

$$\epsilon = \frac{\langle \psi^{\text{trial}} | H | \psi^{\text{trial}} \rangle}{\langle \psi^{\text{trial}} | \psi^{\text{trial}} \rangle} \tag{3.3}$$

represents the trial energy and ψ^{trial} is a trial wave function. The equality of Eq. (3.2) holds if and only if $\psi^{\text{trial}} = \psi$. In this way, a common activity is to use a trial wave function which contains variational parameters such that one may minimize ϵ by adjusting these parameters. The trial wave function which minimizes this expression best reflects the true wave function.

By inserting Eq. (3.1) into the right-hand side of Eq. (3.3), one arrives at the following expression for the trial energy:

$$\epsilon = \frac{\langle \sum_{i=1}^{N_{\text{BF}}} c_i \phi_i | H | \sum_{j=1}^{N_{\text{BF}}} c_j \phi_j \rangle}{\langle \sum_{i=1}^{N_{\text{BF}}} c_i \phi_i | \sum_{j=1}^{N_{\text{BF}}} c_j \phi_j \rangle} = \frac{\sum_{i=1}^{N_{\text{BF}}} \sum_{j=1}^{N_{\text{BF}}} c_i^* c_j H_{ij}}{\sum_{i=1}^{N_{\text{BF}}} \sum_{j=1}^{N_{\text{BF}}} c_i^* c_j S_{ij}}. \tag{3.4}$$

Here, the Hamiltonian matrix elements have been defined as

$$H_{ij} = \int \phi_i(\mathbf{r}) H \phi_j(\mathbf{r}) d\mathbf{r}, \tag{3.5}$$

and the overlap matrix elements have been similarly defined as

$$S_{ij} = \int \phi_i(\mathbf{r})\phi_j(\mathbf{r})d\mathbf{r}. \tag{3.6}$$

Minimizing this expression with respect to the complex conjugate of each expansion coefficient, i.e., over the set $\{c_k^*\}$, amounts to setting the following derivative as zero:

$$\frac{\partial \epsilon}{\partial c_k^*} = \frac{\sum_{j=1}^{N_{\mathrm{BF}}} c_j \left(H_{kj} - \epsilon S_{kj}\right)}{\sum_{i=1}^{N_{\mathrm{BF}}} \sum_{j=1}^{N_{\mathrm{BF}}} c_i^* c_j S_{ij}} = 0. \tag{3.7}$$

This leads to a set of linear equations defining the expansion coefficients within the context of a generalized eigenvalue problem,

$$\sum_{j=1}^{N_{\mathrm{BF}}} H_{kj} c_j = \epsilon \sum_{j=1}^{N_{\mathrm{BF}}} S_{kj} c_j. \tag{3.8}$$

In linear algebra notation, this is equivalent to

$$\mathbf{Hc} = \epsilon \mathbf{Sc}, \tag{3.9}$$

where $\mathbf{H}$ and $\mathbf{S}$ are matrices with elements defined in Eq. (3.5) and Eq. (3.6), respectively, and $\mathbf{c}$ is the column vector containing all expansion coefficients, c_i.

In the limit of a complete basis set, Eq. (3.9) is exactly equivalent to the TISE, as expressed in Eq. (2.6), for the one-particle case, and $\epsilon = E$, the difference only being in the choice of basis—$\{\phi_i\}$ rather than all real space. Similar to the TISE, Eq. (3.9) permits a number of eigensolutions, equal to the basis dimension; Eq. (3.9) is thus rewritten in terms of eigensolution k as

$$\mathbf{Hc}_n = \epsilon_n \mathbf{Sc}_n. \tag{3.10}$$

The min-max theorem [144] then allows one to draw the conclusion that these eigenvalues, ϵ_n, serve as upper bounds to the true eigenvalues, E_n, of the TISE; i.e., $E_n \leq \epsilon_n$. Using this method, then, one may simply solve the generalized eigenvalue problem of Eq. (3.10) using any popular solution technique and, given a basis set which well spans the Hilbert space of interest, determine close approximations to the true energy eigenvalues and wave function eigenvectors. It is worth noting that the proximity of the Ritz method eigenvalues to the true energy values worsens for higher order eigensolutions; thus, if a large number of eigensolutions are necessary, an appropriately large basis dimension must be used.

In the following two sections, the atomic orbital and plane wave bases are presented. These bases first saw application within density functional calculations by representing the ground state system via DFT. Recently, however, both have seen use in TDDFT simulations, with the plane wave basis being very popular. Next, the real space grid approach is introduced as another popular choice for representing wave functions in both DFT and TDDFT codes. Lastly, the pseudospectral basis is introduced as an alternative choice which is associated with advantages in accuracy and simplicity. In order to enhance the computational efficiency of this approach, sum acceleration techniques are introduced to the calculation of the kinetic energy matrix which allow for fewer needed matrix elements in order to achieve the same degree of accuracy as a full matrix calculation. This method is tested for small hydrocarbon molecules and compared to results using the real space grid approach.

3.2 Conventional Basis Sets

3.2.1 Atomic Orbitals

Of the most obvious candidate basis functions are those that resemble single-atom atomic orbitals, which are naturally well suited for describing molecular and bulk solid wave functions. By assuming the form of any given Kohn–Sham orbital in DFT as a linear combination of atomic orbitals (LCAO), one may efficiently describe the many-electron density in terms of required basis size. Furthermore, as a result of this efficiency, it is more common to be able to represent the all-electron system using this choice of basis, as opposed to relying on pseudopotentials. This choice of basis was first used in 1929 by Sir John Lennard-Jones [145] to describe diatomic molecules of the first main row of the periodic table. Today, this type of basis sees extensive use in popular DFT codes such as SIESTA [146], CP2K [147], NWChem [148], GPAW [149] and Q-Chem [150], as well as some limited use in RT-TDDFT codes [108, 151, 152].

The LCAO approach defines the wave function, Φ, or Kohn–Sham orbitals in the case of DFT, as

$$\Phi(\mathbf{r}) = \sum_{a=1}^{N_{\text{atom}}} \sum_{k_a=1}^{n_a} \sum_{l_a=0}^{l_a^{\max}} \sum_{m_a=-l_a}^{l_a} c_{ak_al_am_a}\phi_{k_al_am_a}(\mathbf{r}-\mathbf{R}_a), \tag{3.11}$$

where N_{atom} is the number of atoms represented in the system, n_a is the number of orbitals for the ath atom, $l_a^{\max}$ is the maximum orbital momentum used for a given atom, and $\mathbf{R}_a$ is the location of any given atom. The challenge of describing any given molecular system with DFT now rests in determining the matrix elements

$$H_{ij} = \int \phi_i^*(\mathbf{r}-\mathbf{R}_i)H\phi_j(\mathbf{r}-\mathbf{R}_j)d\mathbf{r} \tag{3.12}$$

and

$$S_{ij} = \int \phi_i^*(\mathbf{r}-\mathbf{R}_i)\phi_j(\mathbf{r}-\mathbf{R}_j)d\mathbf{r}, \tag{3.13}$$

where i and j have been chosen to represent unique combinations of the indices a, k_a, l_a, and m_a used above. Once determined, these matrices can be used in Eq. (3.10) in order to return the linear combination coefficients defining each eigenstate and the associated energy values.

The basis functions, ϕ_i, are most commonly represented by Gaussian type orbitals (GTO). In the literature, a single Gaussian function is called a primitive GTO. Two popular options exist for this representation: spherical primitive GTOs,

$$g_{\zeta,n,l,m}(r,\theta,\phi) = NY_{l,m}(\theta,\phi)r^{2n-2-l}\mathrm{e}^{-\zeta r^2}, \tag{3.14}$$

and Cartesian primitive GTOs,

$$g_{\zeta,l_x,l_y,l_z}(x,y,z) = N x^{l_x} y^{l_y} z^{l_z} \mathrm{e}^{-\zeta r^2}. \tag{3.15}$$

Here, N serves as a normalization factor and the indices used in the latter definition may be related to that of the former, such as $l_x + l_y + l_z = l$. In practice, the final basis functions are often linear combinations of these primitive GTOs which attempt to approximate Slater-type orbitals.

Many well-documented sets of atomic orbitals functions exist and are incorporated within the codes listed above. While this class of basis is widely used, some disadvantages exist when describing ground state systems. First, the basis functions can become overcomplete, meaning linear dependence can occur between functions in close proximity, resulting in the degradation of accuracy. Second, it can often be difficult to design computationally efficient evaluations of the matrix elements. Lastly, it is difficult to demonstrate absolute convergence due to the large number of adjustable parameters used to define the basis functions. The LCAO approach is not as popular as the following representations for use within TDDFT calculations since its primary advantage of optimally representing static molecular wave functions does not translate to the representation of electron distributions that are extended far from the ions without the use of many additional functions. However, some extensions of this basis such as the inclusion of diffuse functions have been shown to better facilitate this purpose [152–155].

3.2.2 Plane Waves

Plane waves serve as another very popular choice of basis in DFT codes. These functions are often preferred due to the simple form of their matrix elements, their orthogonality, and the ability to efficiently facilitate ab initio molecular dynamics calculations. Furthermore, this basis, being spatially periodic in nature, is well equipped to efficiently describe systems of the same symmetry such as bulk solids. Examples of popular plane wave DFT codes include VASP [156], QUANTUM ESPRESSO [157], and ABINIT [158], each of which also support TDDFT in either real time or frequency space forms.

In the plane wave basis, the Kohn–Sham orbitals are represented as

$$\Phi(\mathbf{r}) = \sum_{\mathbf{g}} c_{\mathbf{g}} \phi_{\mathbf{g}}(\mathbf{r}) = \sum_{\mathbf{g}} c_{\mathbf{g}} \langle \mathbf{r} | \mathbf{g} \rangle = \sum_{\mathbf{g}} c_{\mathbf{g}} \frac{1}{\sqrt{\Omega}} \mathrm{e}^{i\mathbf{g}\cdot\mathbf{r}}, \tag{3.16}$$

where Ω is the normalizing volume of the computational space. This notation indicates a sum over choices of three-dimensional reciprocal lattice vector, g. This representation is used in many fields of study due to the simplicity of determining matrix elements resulting from operators containing spatial derivatives. For instance, the kinetic energy operator becomes diagonal

$$-\frac{\hbar^2}{2m}\nabla^2 \phi_{\mathbf{g}}(\mathbf{r}) = -\frac{\hbar^2}{2m}\nabla^2 \frac{1}{\sqrt{\Omega}} \mathrm{e}^{i\mathbf{g}\cdot\mathbf{r}} = \frac{\hbar^2}{2m}|\mathbf{g}|^2 \frac{1}{\sqrt{\Omega}} \mathrm{e}^{i\mathbf{g}\cdot\mathbf{r}} = \frac{\hbar^2}{2m}|\mathbf{g}|^2 \phi_{\mathbf{g}}(\mathbf{r}). \tag{3.17}$$

In most applications, the basis size is defined using what is known as the energy cutoff, E_{cut}. In this scheme, only plane waves exhibiting a kinetic energy eigenvalue less than this cutoff,

$$\frac{\hbar^2}{2m}|\mathbf{g}|^2 < E_{\text{cut}}, \tag{3.18}$$

are kept within the basis set. In this way, one may readily balance accuracy and computational expense by adjusting the value for E_{cut}. In addition to the wave function, the electron density and potentials are also represented as a linear combination of plane waves in this choice of basis. The density, being quadratic in the wave function, requires a larger set of plane waves with an energy cutoff of $4E_{\text{cut}}$. The density, Eq. (2.11), can be calculated as

$$\begin{aligned}\rho(\mathbf{r}) = \sum_{n=1}^{N_{\text{occupied}}} |\Phi_n(\mathbf{r})|^2 &= \frac{1}{\Omega} \sum_{n=1}^{N_{\text{occupied}}} \left(\sum_{\mathbf{g}} c^*_{n,\mathbf{g}} \mathrm{e}^{-i\mathbf{g}\cdot\mathbf{r}} \right) \left(\sum_{\mathbf{g}'} c_{n,\mathbf{g}'} \mathrm{e}^{i\mathbf{g}'\cdot\mathbf{r}} \right) \\ &= \frac{1}{\Omega} \sum_{n=1}^{N_{\text{occupied}}} \sum_{\mathbf{g},\mathbf{g}'} \left(c^*_{n,\mathbf{g}} c_{n,\mathbf{g}'} \mathrm{e}^{i(\mathbf{g}'-\mathbf{g})\cdot\mathbf{r}} \right).\end{aligned} \tag{3.19}$$

This form clearly exhibits a dependence on all plane waves of reciprocal lattice vectors $\mathbf{g}' - \mathbf{g}$ which span the reciprocal lattice within the energy cutoff of $4E_{\text{cut}}$. Local potentials are also represented by plane waves as

$$V(\mathbf{r}) = \frac{1}{\sqrt{\Omega}} \sum_{\mathbf{g}} \widetilde{V}(\mathbf{g}) \mathrm{e}^{i\mathbf{g}\cdot\mathbf{r}}, \tag{3.20}$$

where $\widetilde{V}(\mathbf{g})$ is the Fourier transform of $V(\mathbf{r})$. As in this case, recovering the real space representation of any function in the plane wave basis is straightforward as one need only apply an inverse fast Fourier transform to the expansion coefficients.

The overlap matrix elements are simply $S_{\mathbf{g}\mathbf{g}'} = \delta_{\mathbf{g}\mathbf{g}'}$ since the basis functions are orthonormal. The matrix elements associated with the sum of all local potentials, V, are given as

$$\langle \mathbf{g}|V|\mathbf{g}'\rangle = \frac{1}{\Omega} \int \mathrm{e}^{-i\mathbf{g}\cdot\mathbf{r}} V(\mathbf{r}) \mathrm{e}^{i\mathbf{g}'\cdot\mathbf{r}} d\mathbf{r} = \frac{1}{\sqrt{\Omega}} \widetilde{V}(\mathbf{g} - \mathbf{g}'), \tag{3.21}$$

where $\widetilde{V}$ is the Fourier transform of V. The matrix elements for the nonlocal potential, $W(\mathbf{r}, \mathbf{r}')$, which is of the form found in Eq. (2.52), are defined as

$$\langle \mathbf{g}|W|\mathbf{g}'\rangle = \frac{1}{\Omega} \int\int \mathrm{e}^{-i\mathbf{g}\cdot\mathbf{r}} W(\mathbf{r}, \mathbf{r}') \mathrm{e}^{i\mathbf{g}'\cdot\mathbf{r}} d\mathbf{r} d\mathbf{r}' = \widetilde{W}(\mathbf{g}, \mathbf{g}'). \tag{3.22}$$

The Kohn–Sham Hamiltonian matrix elements are, then,

$$H_{\mathbf{g}\mathbf{g}'} = \langle \mathbf{g}|H^{\text{KS}}|\mathbf{g}'\rangle = \frac{\hbar^2}{2m} |\mathbf{g}|^2 \delta_{\mathbf{g}\mathbf{g}'} + \frac{1}{\sqrt{\Omega}} \widetilde{V}(\mathbf{g} - \mathbf{g}') + \widetilde{W}(\mathbf{g}, \mathbf{g}'). \tag{3.23}$$

In practice, for a small basis size, one may use these matrix elements in order to directly diagonalize the Hamiltonian matrix and solve Eq. (3.10). More commonly, however, the basis size is too large for this approach, and iterative methods such as the conjugate gradient method must be used. However, it is often useful to form the guess for the initial density by directly diagonalizing a plane wave basis Hamiltonian matrix defined using a small cutoff energy.

Due to its naturally periodic form, the plane wave basis is a common choice when describing bulk solids [156, 159]. For such cases, the form of the Kohn–Sham orbitals is that of Eq. (2.65). Here, the periodic functions, $u_{n\mathbf{k}}(\mathbf{r})$, occurring in the definition of the Kohn–Sham orbitals, are the functions which are expanded, resulting in

$$\Phi_{n\mathbf{k}}(\mathbf{r}) = \sum_{\mathbf{g}} c_{n\mathbf{k},\mathbf{g}} \mathrm{e}^{i(\mathbf{g}+\mathbf{k})\cdot\mathbf{r}}. \tag{3.24}$$

The inclusion of $\mathbf{k}$-points in the definition of the Kohn–Sham orbitals does not alter most of the above results; however, some modifications are necessary. For instance, the kinetic energy matrix elements must be calculated as

$$\langle \mathbf{g}+\mathbf{k}|T|\mathbf{g}'+\mathbf{k}\rangle = \frac{\hbar^2}{2m}|\mathbf{g}+\mathbf{k}|^2\delta_{\mathbf{g}\mathbf{g}'}, \tag{3.25}$$

which implies a new cutoff energy procedure according to

$$\frac{\hbar^2}{2m}|\mathbf{g}+\mathbf{k}|^2 < E_{\text{cut}}. \tag{3.26}$$

Furthermore, while the local potential matrix elements remain the same, the nonlocal pseudopotential matrix elements, Eq. (3.22), now become

$$\langle \mathbf{g}+\mathbf{k}|W|\mathbf{g}'+\mathbf{k}\rangle = \widetilde{W}(\mathbf{g}+\mathbf{k},\mathbf{g}'+\mathbf{k}). \tag{3.27}$$

The Hartree potential matrix elements may be determined by solving the Poisson equation

$$\nabla^2 V^{\mathrm{H}}(\mathbf{r}) = -\frac{e^2}{\varepsilon_0}\rho(\mathbf{r}). \tag{3.28}$$

By Fourier transforming the density, one can readily obtain

$$\widetilde{V}^{\mathrm{H}}(\mathbf{g}) = -\frac{e^2}{\varepsilon_0}\frac{\widetilde{\rho}(\mathbf{g})}{|\mathbf{g}|^2}. \tag{3.29}$$

The $\mathbf{g} = \mathbf{0}$ component of $\widetilde{V}^{\mathrm{H}}(\mathbf{g})$ will be divergent if $\widetilde{\rho}(\mathbf{g} = \mathbf{0})$ is nonzero. However, a compensatory Gaussian charge may be added at each atomic position in order to avoid this divergence [160].

For TDDFT calculations involving an external vector potential, $\mathbf{A}(t)$, the matrix elements of the velocity gauge Hamiltonian are given as

$$\langle \mathbf{g}+\mathbf{k}|H^{\mathrm{vel}}(t)|\mathbf{g}'+\mathbf{k}\rangle = \frac{\hbar^2}{2m}|\mathbf{g}+\mathbf{k}+\frac{e}{\hbar}\mathbf{A}(t)|^2\delta_{\mathbf{g}\mathbf{g}'}. \tag{3.30}$$

The time-dependent plane wave basis Hamiltonian matrix elements for a particular $\mathbf{k}$-point are then

$$H^{\mathrm{PW}}_{\mathbf{g}\mathbf{g}'}(t) = \frac{\hbar^2}{2m}|\mathbf{g}+\mathbf{k}+\frac{e}{\hbar}\mathbf{A}(t)|^2\delta_{\mathbf{g}\mathbf{g}'} + V^{\mathrm{PW}}_{\mathbf{g},\mathbf{g}'}(t), \tag{3.31}$$

where

$$V^{\mathrm{PW}}_{\mathbf{g}\mathbf{g}'}(t) = \frac{1}{\sqrt{\Omega}}\widetilde{V}(\mathbf{g}-\mathbf{g}') + \widetilde{W}(\mathbf{g}+\mathbf{k},\mathbf{g}'+\mathbf{k}). \tag{3.32}$$

The time-dependent plane wave basis coefficients, here designated in vectorized notation $\mathbf{c}^{\mathrm{PW}}_{n\mathbf{k}}$, where each element represents the value of $c_{n\mathbf{k},\mathbf{g}}$ at a particular discretized choice of g, may then be described by the equation

$$i\hbar\dot{\mathbf{c}}^{\mathrm{PW}}_{n\mathbf{k}}(t) = \mathbf{H}^{\mathrm{PW}}(t)\mathbf{c}^{\mathrm{PW}}_{n\mathbf{k}}(t). \tag{3.33}$$

There are three major drawbacks of the plane wave basis representation within DFT.

First, it can be relatively difficult to work with spatially localized wave functions, an important task when building order-N methods, due to the extended nature of the basis functions. Second, forward and inverse Fourier transforms between real and reciprocal spaces make parallelization difficult. Third, periodic boundary conditions are a natural condition of the plane wave basis, which is not always desirable. While these issues may be addressed individually, the following discussion of the real space grid representation presents a simple answer to these issues.

3.3 Real Space Grid Approach

The real space grid approach is distinguished from the previous two choices of representation by the fact that no Ritz variational principle is available in this case and no matrix elements are to be calculated. Instead, values are assigned to grid points in real space in order to best approximate continuous functions. Like in the case of the plane wave basis, the balance between accuracy and computational expense may be tuned by adjusting the grid spacing. In lieu of defining matrix elements, this method relies on the use of iterative schemes, such as the conjugate gradient method, which only require the action of the Hamiltonian operator on a grid-defined wave function, to solve the Kohn–Sham equations. The simplicity and versatility of the real space grid approach has led to the rapid development of such calculations [161–165] as an alternative to plane wave-based schemes. This representation has also seen much use with TDDFT [166, 167], as extended electron density may be well represented anywhere within the computational space of equidistant grid points. Today, codes such as GPAW [168] and RMG [169] support grid-based DFT calculations, with GPAW [170] and the popular program OCTOPUS [171] providing TDDFT simulations using this approach.

The Kohn–Sham orbitals, density, and potentials are directly represented on a grid of N_{grid} points with equal spacing h. Any given coordinate, $\mathbf{r}$, on this discretized grid may be assigned as

$$\mathbf{r}_{i,j,k} = (ih, jh, kh), \tag{3.34}$$

such that any wave function may be represented as

$$\psi(\mathbf{r}) \approx \psi(\mathbf{r}_{i,j,k}). \tag{3.35}$$

Here, $i = 1, \ldots, N_x$, $j = 1, \ldots, N_y$, $k = 1, \ldots, N_z$, and $N_{\text{grid}} = N_x N_y N_z$. Integrals may be performed using the three-dimensional trapezoidal rule,

$$\int_\Omega f(\mathbf{r}) d\mathbf{r} \approx h^3 \sum_{i,j,k=1}^{N_{\mathbf{grid}}} f(\mathbf{r}_{i,j,k}). \tag{3.36}$$

In order for this form to provide accurate values, the integrand, $f(\mathbf{r})$, must be band-limited, meaning that the Fourier transform of the integrand must not contain significant values in the frequency range above the maximum defined on the real space grid,

$$\mathbf{g} > \mathbf{g}_{\text{max}} = \pi/h. \tag{3.37}$$

This can present a problem when integrating over pseudopotential contributions to the total energy, in which small shifts of the ion positions with respect to the grid points may cause nonphysical fluctuations in the total energy due to the oscillatory nature of the potentials. Such dependencies on the ion locations is known as an eggbox effect. Fourier filtering techniques have been developed which limit these issues [172]. Alternatively, these considerations may be avoided by using a grid which is fine enough to allow for a sufficiently large $\mathbf{g}_{\text{max}}$.

Derivatives may be evaluated using the finite difference method. In the case of the kinetic energy operator, the action of the Laplacian acting on a wave function may be determined as

$$-\frac{\hbar^2}{2m}\nabla^2\psi(\mathbf{r}_{i,j,k}) \approx -\frac{\hbar^2}{2m}\left[\sum_{n=-N_{\rm FD}}^{N_{\rm FD}} \Delta_n^{(2)}\psi(\mathbf{r}_{i+n,j,k}) + \sum_{n=-N_{\rm FD}}^{N_{\rm FD}} \Delta_n^{(2)}\psi(\mathbf{r}_{i,j+n,k}) + \sum_{n=-N_{\rm FD}}^{N_{\rm FD}} \Delta_n^{(2)}\psi(\mathbf{r}_{i,j,k+n})\right], \quad (3.38)$$

where $\Delta_n^{(2)}$ are the second derivative finite difference coefficients, and $N_{\rm FD}$ is the finite difference order. This is often referred to as a $(2N_{\rm FD}+1)$-point finite difference representation. Unless otherwise specified, $N_{\rm FD}=4$ throughout this thesis when using the real space grid approach. The action of local potentials on a wave function may be straightforwardly determined as the product of each function represented on the grid, $V^{\rm local}(\mathbf{r}_{ijk})\psi(\mathbf{r}_{ijk})$.

The action of the nonlocal pseudopotential, Eq. (2.52), may also be described using a real space grid. Because the nonlocal term is only nonzero within the core region centered upon any ion location, integrals involved in this evaluation must only be represented by sums over grid points within these regions, saving computational effort. The result of the action of the nonlocal pseudopotential on a real space grid may be descried as

$$\int_\Omega V^{\rm pp,nonlocal}(\mathbf{r},\mathbf{r}')\psi(\mathbf{r}')d\mathbf{r}' \approx \sum_{a=1}^{N_{\rm atoms}} \sum_{l,m} \frac{\Delta V_{a,l}^{\rm nl}(|\mathbf{r}_{ijk}-\mathbf{R}_a|)\psi_{a,l,m}^{\rm ps}(\mathbf{r}_{ijk})\,\langle\psi_{a,l,m}^{\rm ps}|\Delta V_{a,l}^{\rm nl}|\psi\rangle}{\langle\psi_{a,l,m}^{\rm ps}|\Delta V_{a,l}^{\rm nl}|\psi_{a,l,m}^{\rm ps}\rangle}, \quad (3.39)$$

where the integral $\langle\psi_{a,l,m}^{\rm ps}|\Delta V_{a,l}^{\rm nl}|\psi\rangle$ must only be carried out over the core region,

$$\langle\psi_{a,l,m}^{\rm ps}|\Delta V_{a,l}^{\rm nl}|\psi\rangle \approx h^3 \sum_{\substack{i,j,k \\ \forall|\mathbf{r}_{ijk}-\mathbf{R}_a|\le r_c^a}} {\psi_{a,l,m}^{\rm ps}}^*(\mathbf{r}_{i,j,k})\Delta V_{a,l}^{\rm nl}(|\mathbf{r}_{i,j,k}-\mathbf{R}_a|)\psi(\mathbf{r}_{i,j,k}). \quad (3.40)$$

With the action of the Hamiltonian defined, one may apply the conjugate gradient method to solve the Kohn–Sham equations. In practice, an initial guess for the Kohn–Sham orbitals is provided, and only a few conjugate gradient steps are necessary in order to find an approximate electron density before updating the functionals at each self-consistent iteration. This process is carried out until the change in energy and density are sufficiently small.

Chapter 4

ACCELERATED PSEUDOSPECTRAL BASES

4.1 Pseudospectral Bases

In the real space grid approach, all grid points are evenly distributed throughout the computational space and are all weighted equally. In general, however, one can choose a means of weighting each grid point in a way which enhances numerical accuracy and/or efficiency. A pseudospectral basis, or discrete variable representation, is a means of doing just that. Here, one chooses a set of interpolant basis functions, which are defined by real space grid points. The wave function and action of local potentials on the wave function are represented as linear combinations of these basis functions, and the scalar product of these basis functions are calculated as a weighted sum over the grid points. This technique has grown in popularity within DFT calculations over the last decade [173–175]. In this section, sinc functions, belonging to a special class of of pseudospectral basis functions known as Lagrange functions [176, 177], are discussed. This class of basis exhibit low computational complexity and are well suited for order-N calculations. Methods of sum-acceleration are introduced as a means of improving the scaling with respect to the grid step size and matrix bandwidth while maintaining a computational speed equivalent with that of the finite difference description.

Here, basis functions are built from the cardinal sine functions, otherwise known as sinc functions,

$$\operatorname{sinc}(x) = \begin{cases} \frac{\sin(\pi x)}{\pi x} & \text{if } x \neq 0 \\ 1 & \text{if } x = 0 \end{cases} . \tag{4.1}$$

The associated one-dimensional orthonormal basis functions are centered on the associated grid points, x_i, and are defined as

$$\phi_i(x) = \frac{1}{\sqrt{h}} \text{sinc}\left(\frac{x - x_i}{h} \right), \tag{4.2}$$

where h is the grid step size. In this case, the kinetic energy matrix elements may be calculated as [160]

$$t_{ij} = \left\langle \phi_i \middle| -\frac{\hbar^2}{2m} \frac{d^2}{dx^2} \middle| \phi_j \right\rangle = \left\{ \begin{array}{ll} \frac{\hbar^2 \pi^2}{6h^2 m} & \text{if } i = j \\ \frac{\hbar^2 (-1)^{i-j}}{h^2 (i-j)^2 m} & \text{if } i \neq j \end{array} \right. . \tag{4.3}$$

These matrix elements depend only on $(i - j)$. Therefore, the matrix, t, is constant along diagonals and is an example of a Toeplitz matrix as described in Ref. [178]. This matrix is $N \times N$ in size, where N is the number of grid points used to define unique sinc functions.

The three-dimensional pseudospectral basis functions may be defined in the straightforward manner,

$$\Phi_i(\mathbf{r}) = \phi_{i1}(x)\phi_{i2}(y)\phi_{i3}(z), \tag{4.4}$$

where index i indicates a unique combination of $i1$, $i2$, and $i3$. The three-dimensional kinetic energy matrix elements may be constructed in a similarly simple way,

$$T_{ij} = \left\langle \Phi_i \middle| -\frac{\hbar^2}{2m} \frac{d^2}{dx^2} \middle| \Phi_j \right\rangle = t_{i1,j1}\delta_{i2,j2}\delta_{i3,j3} + \delta_{i1,j1}t_{i2,j2}\delta_{i3,j3} + \delta_{i1,j1}\delta_{i2,j2}t_{i3,j3}. \tag{4.5}$$

For pseudospectral bases, matrix elements related to local potentials may be conveniently evaluated from the potential represented on the real space grid,

$$V_{ij} = \langle \Phi_i | V | \Phi_j \rangle = V(\mathbf{r}_{i1,i2,i3})\delta_{i1,j1}\delta_{i2,j2}\delta_{i3,j3}. \tag{4.6}$$

The nonlocal pseudopotential matrix elements may be calculated as

$$V_{ij}^{\mathrm{NL}} = \sum_{a}\sum_{l,m} \frac{{g_{l,m,i}^{a}}^{*} g_{l,m,j}^{a}}{\langle \psi_{a,l,m}^{\mathrm{ps}} | \Delta V_{a,l}^{\mathrm{nl}} | \psi_{a,l,m}^{\mathrm{ps}} \rangle}, \tag{4.7}$$

where

$$g_{l,m,i}^{a} = \int_{|\mathbf{r}-\mathbf{R}_a| \leq r_c^a} \psi_{a,l,m}^{\mathrm{ps}}(\mathbf{r}) \Delta V_{a,l}^{\mathrm{nl}}(|\mathbf{r}-\mathbf{R}_a|) \Phi_i(\mathbf{r}) d\mathbf{r}. \tag{4.8}$$

If the product $\psi_{a,l,m}^{\mathrm{ps}}(\mathbf{r})\Delta V_{a,l}^{\mathrm{nl}}$ may be described by a form such as a linear combination of Gaussians,

$$\psi_{a,l,m}^{\mathrm{ps}}(\mathbf{r}) \Delta V_{a,l}^{\mathrm{nl}}(\mathbf{r}) = \sum_{i} c_{l,i}^{a} \mathrm{e}^{-\nu_i r^2} r^l Y_{lm}(\hat{\mathbf{r}}), \tag{4.9}$$

then $g_{l,m,i}^{a}$ may be calculated analytically, leading to a more accurate representation than in the real spacegrid approach. On the other hand, in the real space grid approach, $g_{l,m,i}^{a}$ is only nonzero for grid points within the small core regions centered on the ion sites, whereas for the sinc basis, this integrand is nonzero for the entirety of the computational space. This would imply a significantly greater computational expense for the sinc basis representation. However, it will be shown in Sec. 4.3 that a large fraction of the matrix elements are negligible and that one may truncate $g_{l,m,i}^{a}$ to effectively the same region as the real space grid representation.

While, compared to the real space grid approach, pseudospectral representations allow for more accurate representations of the kinetic energy contribution due to the weighted sum of values, the matrices are more dense. On the otherhand, due to the enhanced accuracy, less grid points are necessary, resulting in smaller matrix dimensions. The grid step size can be limited by other factors, however, such as the oscillatory pseudopotentials and density. The large bandwidth of the kinetic energy matrix eventually becomes a bottleneck for computational efficiency considerations.

In order to make pseudospectral approaches more computationally efficient, one must decrease the kinetic energy matrix bandwidth while maintaining accuracy. The direct truncation of the matrix is not a satisfactory solution as the derivative series is alternating and converges slowly, thus resulting in significantly inaccurate values when only a few terms are present. John Boyd has developed [179, 180] a sum-acceleration method for pseudospectral bases and finite difference approaches which allows for exponential series convergence using sparse matrices via application of acceleration weights within the definition of the kinetic energy matrices.

4.2 Sum-Acceleration Weights

As mentioned in Sec. 3.3, derivatives in methods such as the real space grid approach are calculated as weighted sums over the wave function evaluated at grid point neighboring that of interest. This is exemplified by the important case of the one-dimensional second derivative,

$$\frac{d^2}{dx^2}\psi(x_i) \approx \Delta_0^{(2)}\psi(x_i) + \sum_{n=1}^{m}\left[\Delta_n^{(2)}\psi(x_{i+n}) + \Delta_{-n}^{(2)}\psi(x_{i-n})\right]. \tag{4.10}$$

In the real space grid approach, the second derivative weights, $\Delta_n^{(2)}$, are the relevant finite difference coefficients which are symmetric, meaning $\Delta_{-n}^{(2)} = \Delta_n^{(2)}$. The description of Eq. (4.10) is similarly well-suited to the pseudospectral approach in which basis functions are assigned at the same sites, x_i, and the second derivative weights are the matrix elements t_{in}, defined in Eq. (4.3), without the factor of $-\frac{\hbar^2}{2m}$. While in the case of the finite difference method, the sum on the right-hand side is truncated to a small number of terms, such as $m = 4$, in the pseudospectral case, the second derivative sum is defined using all points in the grid. The inclusion of all points results in high accuracy; however, since the speed of calculating the action of the kinetic energy matrix on the wave function vector is determined by the number of terms necessary to compute, the pseudospectral basis representation can be significantly more computationally costly than the real space grid approach.

One may truncate the sum in the case of the pseudospectral basis to the same number of terms as in the finite difference approach in order to achieve the same computational cost. However, because this sum is alternating and slowly converging, many terms are necessary in order to produce accurate results, and, thus, such a truncation undermines the advantage of the pseudospectral representation. John Boyd showed in Ref. [179] that Euler sum-acceleration may be applied in this case in order to significantly improve the convergence of this sum and thus make truncation viable. In this case, the second derivative weights are modified as

$$\widetilde{\Delta}_n^{(2)} = w_n \Delta_n^{(2)}, \tag{4.11}$$

where the Euler acceleration weights are defined as

$$w_n = \sum_{k=n}^{m} \frac{m!}{2^m k!(m-k)!}, \quad n = 1, 2, \ldots, m \tag{4.12}$$

and

$$w_0 = \frac{-12}{\pi^2} \sum_{k=1}^{m} \frac{(-1)^k w_k}{k^2}. \tag{4.13}$$

Other choices for acceleration weights, distinguished by their sampling of frequency space, have also been investigated which similarly allow for faster convergence of derivative sums [180, 181].

4.3 Computational Details and Results for Small Hydrocarbons

Despite advantages of the pseudospectral basis, this choice is still not as popular as the previously discussed representations, atomic orbitals, plane waves, and the real space grid. In this section, results are presented using the acceleration weights of Boyd in order to provide a step towards optimizing this basis for density functional calculations. These calculations are presented in atomic units (a.u.) in which $\hbar = e = m_e = 1/4\pi\varepsilon_0 = 1$; in familiar units, this corresponds to length units of 0.52918 Å, known as a Bohr, and energy units of 27.211 eV, known as a Hartree. Small hydrocarbons such as C_2H_2, C_3H_6, and

C_3H_8 are tested within a computational box of $18 \times 18 \times 18$ (a.u.)^3. All data and figures in this section are reproduced from Ref. [182] with the permission of Wiley Periodicals, Inc.

The accelerated pseudospectral matrices used are defined as

$$t_{ij}^{\text{acc}} = \begin{cases} t_{ij} w_{|i-j|} & \text{if } |i-j| \leq m \\ 0 & \text{otherwise} \end{cases} . \tag{4.14}$$

Here, the matrices are truncated to a bandwidth of $2m+1$. In the following results, $m = 8$ has been used. The options for the acceleration weights, w_k ($k = 0, \ldots, m$), are taken from Table I. of Ref [181] which include the Euler weights of Boyd [180] as well as others. The comparative finite difference kinetic energy matrix is defined as

$$t_{ij}^{\text{FD}} = \begin{cases} -\frac{\hbar^2}{2m} \Delta_{|i-j|}^{(2)} & \text{if } |i-j| \leq m \\ 0 & \text{otherwise} \end{cases} , \tag{4.15}$$

where m indicates the finite difference order, $m = N_{\text{FD}}$, and $\Delta_k^{(2)}$ are the finite difference coefficients.

The convergence of the total energy calculated by a full sinc basis for the molecule C_2H_2 is compared to that of the truncated sinc basis, that is $w_k = 1$ for all k, and the $m = 8$, that is 17-point, finite difference method in Fig. 4.1. The reference energy is the total energy calculated using $N = 80$. Here, N indicates the number of basis functions used along any particular direction of the three-dimensional computational box; therefore, the full basis size is N^3. In this comparison, fully converged Kohn–Sham orbitals were calculated for different grid sizes. This figure shows that the energy accuracy significantly decreases when crudely truncating the sinc basis. The truncation to $m = 8$ allows for the same computational efficiency as the $m = 8$ finite difference, real space grid approach, but the energy results are wildly inaccurate. A truncation to $m = N/3$, which maintains a substantial matrix bandwidth, is still less accurate than the $m = 8$ finite difference representation. The oscillations with respect to number of grid points is a result of shifts in

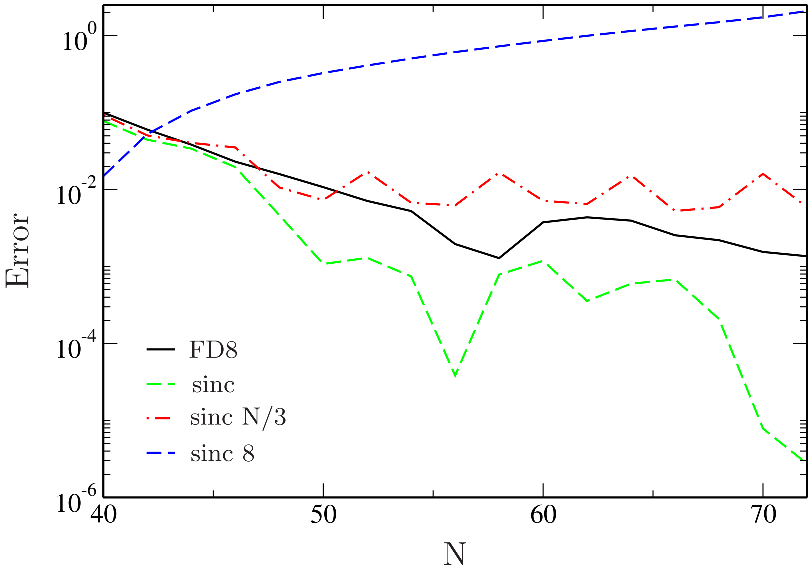

Figure 4.1: Comparison of the total energy accuracy of truncated sinc calculations for grid sizes raging between $N = 40$ to $N = 72$, corresponding to changing h from 0.45 a.u. to 0.25 a.u.; $m = 8$ finite difference (solid, black line), full sinc (dashed, light green line), sinc truncated to $m = N/3$ (dash-dotted, red line), and sinc truncated to $m = 8$ (dashed, dark blue line). The C_2H_2 molecule was used in these calculations.

the relative position of the atomic sites relative to the grid point locations. The lower error for the $m = 8$ truncated sinc matrix for small basis size is an artifact of the loss of the variational property. It is by accident that the energy calculated in that region happens to be closer to the converged value.

The results of applying various choices of acceleration weights to the $m = 8$ truncated sinc kinetic energy matrix are shown in Fig. 4.2 for the C_3H_8 molecule. In this figure, the accuracy of the kinetic energy is compared by reference to that calculated by use of the full $N = 80$ sinc basis matrix. The kinetic energies of the $m = 4$ and $m = 8$ finite difference calculations converge slowly compared to those of the $m = 8$ accelerated sinc representations, which are nearly identical to that the full sinc matrix. The latter result indicates that the acceleration succeeds extremely well in providing pseudospectral accuracy while exhibiting computational efficiency equivalent to that of the finite difference method. For the smallest grid spacing used, the difference between the full sinc representation and the best

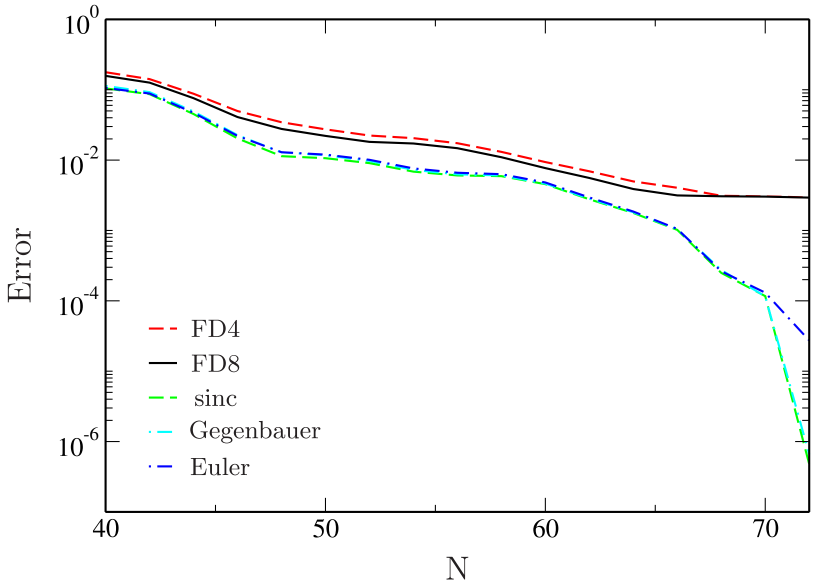

Figure 4.2: Comparison of the accuracy of the kinetic energy for grid sizes raging between $N = 40$ to $N = 72$, corresponding to changing h from 0.45 a.u. to 0.25 a.u.; $m = 4$ finite difference (dashed, red line), $m = 8$ finite difference (solid, black line), full sinc (dashed, light green line), $m = 8$ Gegenbauer-accelerated sinc (dash-dotted, cyan line), and $m = 8$ Euler-accelerated sinc (dash-dotted, dark blue line). Note that the Gegenbauer- and Euler-accelerated sinc representations yield nearly overlapping results. The C_3H_8 molecule was used in the calculations.

truncated, accelerated sinc representation is less than 10^{-6} a.u. Here, the Euler acceleration weights [179, 180] provide slightly less accurate results than the others listed in Table I. of Ref. [181]. The Gegenbauer, step, and sech weights (see Table I of Ref. [181]) give nearly identical results. Therefore, the latter two options are not shown.

The total energy for these choices of representation are shown in Fig. 4.3 for the C_2H_2, C_3H_6, and C_3H_8 molecules. The finite difference methods continue to exhibit slow convergence with doubling the finite difference order making little difference. The total energies truncated, accelerated sinc matrices, however, converge much quicker and often overlap with the full matrix results. For large grid spacings, the finite difference and sinc total energies are very close, indicating that the error in those cases arise from the coarse representation of the Kohn–Sham orbitals rather than the kinetic energy. The most economical choice for the grid spacing appears to be around $h = 0.35$ a.u., corresponding to $N = 50$,

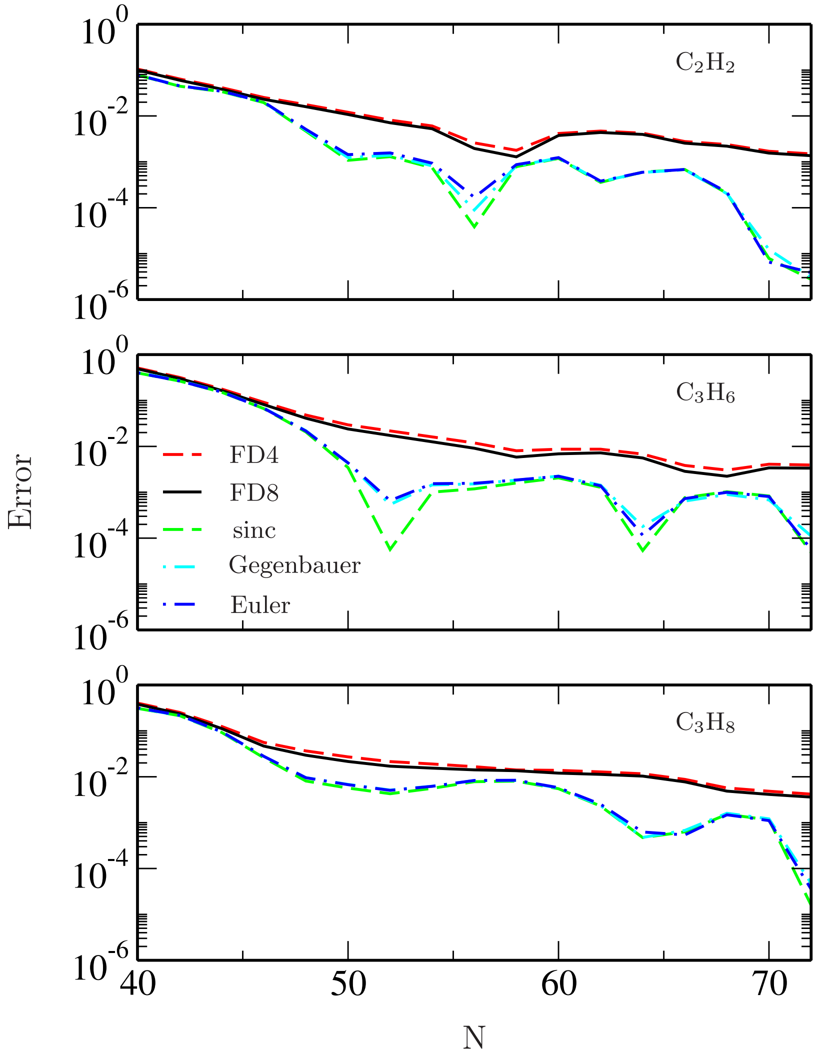

Figure 4.3: Comparison of the accuracy of the total energy for molecules C_2H_2 (top), C_3H_6 (middle), and C_3H_8 (bottom) using grid sizes ranging between $N = 40$ to $N = 72$, corresponding to changing h from 0.45 a.u. to 0.25 a.u.; $m = 4$ finite difference (dashed, red line), $m = 8$ finite difference (solid, black line), full sinc (dashed, light green line), $m = 8$ Gegenbauer-accelerated sinc (dash-dotted, cyan line), and $m = 8$ Euler-accelerated sinc (dash-dotted, dark blue line). Note that the Gegenbauer- and Euler-accelerated sinc representations yield nearly overlapping results.

at which point the sinc calculations are about one to two orders of magnitude more accurate than the finite difference real space grid approach. Decreasing the grid spacing past this point results in diminishing returns in accuracy.

Convergence of the Euler-accelerated sinc basis with respect to the kinetic energy ma-

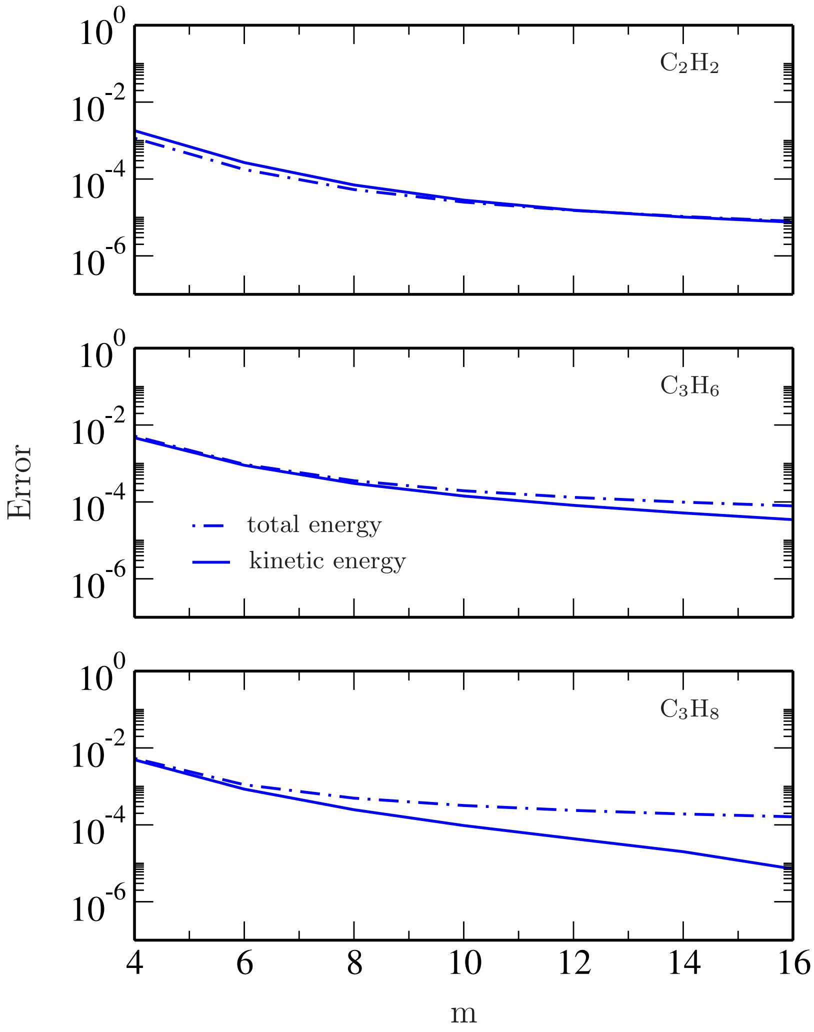

Figure 4.4: Dependence of the total (dash-dotted) and kinetic (solid) energy accuracy on the matrix bandwidth, $2m + 1$, for molecules C_2H_2 (top), C_3H_6 (middle), and C_3H_8 (bottom), using the Euler-accelerated sinc basis. A grid size of $N = 60$ was employed, corresponding to a grid step size of $h = 0.3$ a.u. The reference value was the total energy calculated on the same grid using the full sinc matrix.

trix bandwidth is presented in Fig. 4.4. For the larger molecules, once m is larger than around 10, the kinetic energy is sufficiently accurate and is no longer the prominent source of error as other detractors to the accuracy dominate. Results are summarized in Tab. 4.1 for the accuracy of the total energy using $m = 4$ or $m = 8$ for both finite difference and Euler-accelerated sinc representations. The Euler-accelerated kinetic energy converges much more quickly with respect to matrix bandwidth.

C_2H_2	FD	Euler
$m = 4$	3.0×10^{-3}	2.4×10^{-3}
$m = 8$	2.6×10^{-3}	4.7×10^{-5}

C_3H_6	FD	Euler
$m = 4$	6.6×10^{-3}	8.5×10^{-3}
$m = 8$	4.8×10^{-3}	1.7×10^{-4}

C_3H_8	FD	Euler
$m = 4$	8.3×10^{-3}	8.4×10^{-3}
$m = 8$	6.5×10^{-3}	1.5×10^{-4}

Table 4.1: Comparison of the bandwidth dependence of the total energy accuracy for finite difference (FD) and Euler-accelerated sinc (Euler) representations, using molecules C_2H_2, C_3H_6, and C_3H_8. A grid size of $N = 60$ was employed, corresponding to a grid step size of $h = 0.3$ a.u. The reference value was the total energy calculated on the same grid using the full sinc matrix.

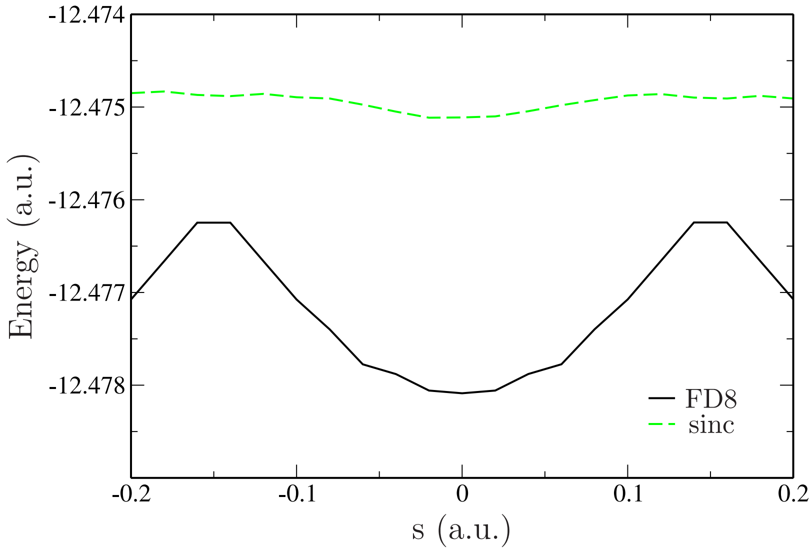

Figure 4.5: Comparison of the total energy dependence on the shift, s, of the grid points along the axis of the C_2H_2 molecule using the $m = 8$ finite difference real space grid and sinc basis representations. $N = 60$ and $h = 0.3$ a.u.

The accuracy in the total energy is also partially dictated by the ability to resolve the oscillatory nonlocal pseudopotential, as has been discussed in Sec. 4.1. Fig. 4.5 shows this energy contribution as a function of the relative positions of the grid points and the atomic centers. The eggbox effect is illustrated in the finite difference results where the energy value fluctuates as the grid points shift. The sinc calculations, however, do not exhibit this behavior and remain smooth in energy value. This is a result of the analytic integration in Eq. (4.8). In principle, all grid points, i, contribute to $g^a_{l,m,i}$, but the values of $g^a_{l,m,i}$ for grid points far from the pseudopotential center, a, are small. In this example, only values such that $|g^a_{l,m,i}| > 10^{-8}$ have been kept. This choice preserves the accuracy of the calculation and the sparsity of V^{NL}_{ij}. The results of using the full t and $m = 8$ Euler-accelerated t^{acc} kinetic energy matrix representations overlap. The grid dependence for the sinc calculations in this case comes from the local part of the pseudopotential.

While only grid points within the pseudopotential core region must be considered in the real space grid calculation of $g^a_{l,m,i}$, in the sinc case, using the above described truncation, points at a distance of up to twice the core radius yield non-negligible contribution. This results in a computational cost of calculating $g^a_{l,m,i}$ which is about an order of magnitude greater than in the real space grid case. This, however, is balanced by the better accuracy when using the sinc basis and the need for less grid points in general.

4.4 Summary

It has been shown that by introducing Euler acceleration to the truncated sinc function kinetic energy matrix, one is able to achieve results similar in accuracy to those obtained by using the full sinc kinetic energy matrix. This allows for pseudospectral simplicity and accuracy with computational efficiency on par with the widely used finite difference method used in the real space grid approach. The accelerated sinc matrix descriptions scales preferably with the grid step size as well as the matrix bandwidth. These improvements should prove invaluable towards the description of larger systems often described within DFT.

The sinc basis functions were also shown to eliminate the eggbox effect when representing pseudopotentials by analytical evaluation of the nonlocal matrix elements, possible when the pseudopotential functions can be represented by linear combinations of Gaussians. This construction effectively removes the dependence of the energy on the relative positions of the grid points and the ion centers.

Chapter 5

PROPAGATION ALGORITHMS

5.1 Introduction

So far, techniques for discretely representing wave functions in $\mathbf{r}$ have been discussed by means of a variety of bases. Such approaches are necessary for describing wave functions computationally and solving the Kohn–Sham equations of DFT. Because the DFT ground state description serves as the initial state of TDDFT simulations, these considerations are directly pertinent to time-dependent studies. Oftentimes, the plane wave basis or real space grid approach representations are used within TDDFT calculations due to their ability to flexibly describe orbitals which extend from the ion sites. In the case of a time-dependent wave function, the basis function representation, Eq. (3.1), is modified by allowing the expansion coefficients to vary in time:

$$\psi(\mathbf{r},t)=\sum_{i=1}^{N_{\mathrm{BF}}} c_i(t)\phi_i(\mathbf{r}). \tag{5.1}$$

In this chapter, techniques of solving the TDKS equations of RT-TDDFT,

$$i\hbar\frac{\partial}{\partial t}\Phi_n(\mathbf{r},t)=H^{\mathrm{KS}}[\rho](\mathbf{r},t)\Phi_n(\mathbf{r},t), \tag{5.2}$$

are discussed. In practice, the Kohn–Sham Hamiltonian, H^{KS}, is represented as a matrix, $\mathbf{H}^{\mathrm{KS}}$, in terms of the basis employed according to Eq. (3.5) and the Kohn–Sham orbitals, Φ_n are replaced in Eq. (5.2) by vectors containing the expansion coefficients or, in the case of the real space approach, the space-discretized orbitals. Furthermore, in the case of a nonorthogonal basis set, the Kohn–Sham Hamiltonian is replaced with the matrix product $\mathbf{S}^{-1}\mathbf{H}^{\mathrm{KS}}$, where $\mathbf{S}^{-1}$ is the inverse of the overlap matrix. In this discussion, however, an orthonormal basis will be assumed for the sake of simplicity, as this is often the case in time-dependent programs.

In the remainder of this chapter, methods of propagation by direct numerical integration are introduced, followed by a popular class of solution techniques which makes use of a time evolution operator. Next, a new class of solution techniques known as exponential integrators are introduced to RT-TDDFT. These techniques allow for the separate evolution of the linear and nonlinear parts of the TDKS equation, thereby allowing for an improvement over the accuracy of conventional techniques of up to multiple orders of magnitude. Results of the exponential integrator methods applied to the description of various excitations of the one-dimensional Helium atom and compared to those of the conventional time propagation techniques.

5.2 Propagation via Direct Numerical Integration

The simplest form of solving the single-particle TDSE,

$$i\hbar\frac{\partial}{\partial t}\psi(\mathbf{r},t) = H(\mathbf{r},t)\psi(\mathbf{r},t), \tag{5.3}$$

comes from approximating the time derivative of the wave function using the two-point, forward finite difference representation,

$$\frac{\partial\psi}{\partial t} \approx \frac{\psi(t_{m+1}) - \psi(t)}{\Delta t}, \tag{5.4}$$

where $t_m = m\Delta t$. This leads to an expression for prescribing $\psi(t_{m+1})$ known as the explicit forward Euler method,

$$\psi(t_{m+1}) = \psi(t_m) - \frac{i}{\hbar}\Delta t H(t_m)\psi(t_m). \tag{5.5}$$

Alternatively, one may define the implicit backwards Euler method as

$$\psi(t_{m+1}) = \psi(t_m) - \frac{i}{\hbar}\Delta t H(t_{m+1})\psi(t_{m+1}). \tag{5.6}$$

The latter is a more stable approach; however, it is clearly more computationally expensive as one must determine the explicitly not known $H(t_{m+1})\psi(t_{m+1})$. These methods are $\mathcal{O}(\Delta t^2)$ accurate in time.

Another, more accurate and widely used approach, is that of the Runge–Kuta method. Here, one approximates the following step, $\psi(t_{m+1})$ from the current step, $\psi(t_m)$, by taking a weighted average of the estimated slopes evaluated at temporal increments between the two steps. When choosing only one increment, one defines the above described Euler method. For two increments, one arrives at the second-order Runge–Kutta (RK2) method,

$$\begin{aligned} \psi(t_{m+1}) &= \psi(t_m) + k_2 \\ k_1 &= -\frac{i}{\hbar}\Delta t H[\rho_{\psi(t_m)}]\psi(t_m) \\ k_2 &= -\frac{i}{\hbar}\Delta t H[\rho_{\psi(t_m)+k_1/2}]\left[\psi(t_m) + \frac{1}{2}k_1\right]. \end{aligned} \tag{5.7}$$

Here, $H[\rho_{\psi(t_m)}]$ indicates that, in the case of RT-TDDFT, the Hamiltonian functional is updated with a density, ρ, calculated using $\psi(t_m)$. This technique is $\mathcal{O}(\Delta t^2)$ accurate in time.

The fourth-order Runge–Kutta (RK4) method is more commonly used within RT-TDDFT simulations [85, 183] and takes the form

$$\begin{aligned}\psi(t_{m+1}) &= \psi(t_m) + \frac{1}{6}k_1 + \frac{1}{3}k_2 + \frac{1}{3}k_3 + \frac{1}{6}k_4 \\ k_1 &= -\frac{i}{\hbar}\Delta t H[\rho_{\psi(t_m)}]\psi(t_m) \\ k_2 &= -\frac{i}{\hbar}\Delta t H[\rho_{\psi(t_m)+k_1/2}]\left[\psi(t_m) + \frac{1}{2}k_1\right] \\ k_3 &= -\frac{i}{\hbar}\Delta t H[\rho_{\psi(t_m)+k_2/2}]\left[\psi(t_m) + \frac{1}{2}k_2\right] \\ k_4 &= -\frac{i}{\hbar}\Delta t H[\rho_{\psi(t_m)+k_3}]\left[\psi(t_m) + k_3\right].\end{aligned} \tag{5.8}$$

This method exhibits high computational cost, as four evaluations of the Kohn–Sham Hamiltonian are required. On the other hand, however, the allowed time step size is much larger because the accuracy only scales as $\mathcal{O}(\Delta t^4)$.

5.3 Propagation via the Time Evolution Operator

The time evolution operator approaches are derived from the exact solution to the single-particle TDSE, Eq. (5.3), for a wave function at time t,

$$\psi(\mathbf{r}, t) = U(t, 0)\psi(\mathbf{r}, 0), \tag{5.9}$$

where the time evolution operator is

$$U(t, 0) = \mathcal{T} \exp\left[-\frac{i}{\hbar}\int H(\mathbf{r}, t')dt'\right]. \tag{5.10}$$

Here, $\mathcal{T}$ indicates time-ordering. Two properties worth noting of the time evolution operator are the following: (1) it is unitary for Hermitian Hamiltonains, $U(t', t)^\dagger = U^{-1}(t', t)$, and (2) it exhibits time reversal symmetry $U(t, t') = U^{-1}(t', t)$.

In practice, one splits the above, exact, representation of the time evolution operator into a product of multiple approximate time evolution operators, corresponding to a short time step, Δt,

$$U(t,0) = \prod_m U(t_m, t_{m+1}), \tag{5.11}$$

$$U(t_m, t_{m+1}) \approx \exp\left[-\frac{i}{\hbar}H(t_m)\Delta t\right]. \tag{5.12}$$

The short time steps ensure that the Hamiltonian at time t_m remains nearly commutative with the Hamiltonian at t_{m+1} and that the integral in Eq. (5.10) may be well-approximated with a left Riemann sum.

In the following sections, various popular choices for the approximation of the matrix exponential in Eq. (5.12) are introduced. In any case, one must choose an appropriately small time step size. One may determine the upper bound for this value by examining the energy-time uncertainty principle, $\Delta E \Delta t \leq \hbar$. By this reasoning, time step sizes satisfying $\Delta t \leq \hbar/\Delta E$ are required in order to resolve dynamics of a system resulting in changes of the total energy, ΔE. This illustrates that the required time step size can vary with whatever dynamics are being studied. The following approximations for the discrete time step time evolution operator will also provide limitations on the maximum size of the time step allowed.

5.3.1 Taylor Expansion of the Time Evolution Operator

A straightforward means of approximating the discrete time step evolution operator is by Taylor expansion. This approach breaks the exponential into a sum of polynomials. Such expansions are not unique to the Taylor expansion; another example is that of the Chebychev propagator [184, 185]. The popularity of the Taylor expansion is due to its simplicity: only the repeated action of the Hamiltonian is needed. In this way, it is not necessary to store the full Hamiltonian matrix, as, instead, one only requires the result of its action on a wave function vector. This makes the Taylor expansion the prominent propagation technique for the real space grid approach, which makes use of the same principle.

The form of the discrete time step time evolution operator becomes

$$\exp\left[-\frac{i}{\hbar}H(t_m)\Delta t\right] \approx \sum_{n=0}^{N_{\text{Taylor}}} \frac{1}{n!}\left(-\frac{i\Delta t}{\hbar}H^{\text{KS}}(t_m)\right)^n . \tag{5.13}$$

While $N_{\text{Taylor}} \to \infty$ would result in an exact expression, in practice, one must truncate this expansion. This truncation breaks the unitarity of the exponential and the stability of the propagation becomes dependent on the time step size used. The term "stability" here is introduced to describe the preservation of the norm of the wave function, $|\psi|^2$. A truncation to $N_{\text{Taylor}} = 4$ has been demonstrated to provide optimal stability and accuracy [133, 184] and a time step size of 0.001 fs has been used in many TDDFT studies [186–191]. The maximum time step size, however, is dependent on the system of study as well as the potentials used; for instance, high intensity laser fields require smaller Δt.

5.3.2 Crank–Nicolson Approximation

By averaging the forward and backward Euler methods, one obtains the Crank–Nicolson (CN) propagation scheme,

$$\psi(t_{m+1}) = \psi(t_m) - \frac{i\Delta t}{2\hbar}\left[H(t_m)\psi(t_m) + H(t_{m+1})\psi(t_{m+1})\right]. \tag{5.14}$$

Rearranging terms yields

$$\left[1 + \frac{i\Delta t}{2\hbar}H(t_{m+1})\right]\psi(t_{m+1}) = \left[1 - \frac{i\Delta t}{2\hbar}H(t_m)\right]\psi(t_m), \tag{5.15}$$

and by approximating that $H(t_{m+1}) \approx H(t_m)$ in the limit of small Δt, one may derive the CN propagation technique,

$$\psi(t_{m+1}) \approx \left[1 + \frac{i\Delta t}{2\hbar}H(t_m)\right]^{-1}\left[1 - \frac{i\Delta t}{2\hbar}H(t_m)\right]\psi(t_m), \tag{5.16}$$

which is $\mathcal{O}(\Delta t^4)$ accurate in time.

This method approximates the time evolution operator as

$$\exp\left[-\frac{i}{\hbar}H(t_m)\Delta t\right] \approx \left[1+\frac{i\Delta t}{2\hbar}H(t_m)\right]^{-1}\left[1-\frac{i\Delta t}{2\hbar}H(t_m)\right]. \tag{5.17}$$

The primary advantage of this representation of the time evolution operator is that it remains unitary so that the norm remains conserved explicitly, apart from roundoff errors. This allows for long propagations with many time steps which maintain reasonable accuracy. The primary disadvantage is the required calculation of the matrix inverse. While iterative methods for the calculation of matrix inverses make calculations possible for cases involving the storage of full matrices, the application of the CN propagator is not viable in real space grid approaches for large systems.

5.3.3 Split Operator Approach

The split operator (SPO) approach is of the earliest propagation techniques, dating back to its first appearance in 1957 [192] and an independent emergence in 1968 as “Sprang splitting” in Ref. [193]. This approach is simplistic in nature and consists of splitting the Hamtiltonian into kinetic and potential energy parts and approximating the time evolution operator as a product of exponentials of these constituents. This was first used in the field of physics in Ref. [194] and later was incorporated in RT-TDDFT in Ref. [195] using higher order decompositions.

As described, the discrete time evolution operator is approximated as

$$\exp\left[-\frac{i}{\hbar}H(t_m)\Delta t\right] \approx \exp\left[-\frac{i}{2\hbar}T\Delta t\right]\exp\left[-\frac{i}{\hbar}V(t_m)\Delta t\right]\exp\left[-\frac{i}{2\hbar}T\Delta t\right], \tag{5.18}$$

or similarly,

$$\exp\left[-\frac{i}{\hbar}H(t_m)\Delta t\right] \approx \\ \exp\left[-\frac{i}{2\hbar}V(t_m)\Delta t\right]\exp\left[-\frac{i}{\hbar}T\Delta t\right]\exp\left[-\frac{i}{2\hbar}V(t_m)\Delta t\right]. \quad (5.19)$$

The accuracy of these expressions scale as $\mathcal{O}(\Delta t^4)$ [196]. This form is chosen such that each matrix exponential is diagonal in either real space or reciprocal space, facilitated by fast Fourier transforms. For example, if acting on a wave function given in real space, one may first apply the rightmost exponential of Eq. (5.18) which is diagonal in real space. Next, the result may be Fourier transformed into reciprocal space in which the subsequent exponential related to the kinetic energy is diagonal. A final Fourier transform can then be used to return the representation to real space in which the final remaining exponential is, again, diagonal. Furthermore, the SPO approach has the advantage of maintaining unitarity and being unconditionally stable [197].

5.4 Exponential Integrators

Many phenomenon of interest call for long simulations which, in turn, require long time stability and accuracy; however, for RT-TDDFT propagation, the numerical solution gradually deteriorates over the course of many time steps, often limiting the scope of what can be studied. This problem is, in part, due to the fact that the TDKS equations represent a set of differential equations which are nonlinear, due to the dependence of the Hamiltonian on the density, and, thus, the Kohn–Sham orbitals. In conventional RT-TDDFT calculations, the nonlinear part of the TDKS equation is not distinguished from the linear part. Instead, it is time propagated using the time evolution operator together with the rest of the Hamiltonian. The only distinguishing feature is, then, the additional step in each iteration which updates the nonlinear terms in order to satisfy self-consistency. The nonlinear terms are only approximately known. Thus, their inclusion in the matrix exponential that is the time evolution operator magnifies inherent inaccuracies, leading to numerical errors.

Various mathematical approaches have been developed in order to solve such nonlinear differential equations. In order to solve the initial value problem

$$\frac{dy}{dt} = f(y,t), \qquad y(t=0) = y_0, \tag{5.20}$$

one may separate the linear, Ly, and nonlinear, $N(y,t)$, parts of $f(y,t)$ as

$$\frac{dy}{dt} = Ly + N(y,t). \tag{5.21}$$

The relative influence of either part will vary, depending on the the type of operators involved. An ideal method for the solution of this sort of problem would be to incorporate separate approximations that are best suited to either part individually.

Here, two robust methods are introduced which have been developed for this purpose, the integrating factor (IF) [198] and exponential time differencing (ETD) [198] methods. These methods are collectively known as exponential integrators. The IF method introduces a new variable by factoring out the stiff part of the equation, and only the nonlinear part of the differential equation must be solved by time stepping procedures. In the ETD method, the exact integration of the linear part is followed by an approximate integration of the nonlinear part. Both approaches have been tested for cases of dissipative and dispersive partial differential equations [198–202] with the ETD method appearing most accurate in test calculations.

There are three important distinctions between the differential equations solved in RT-TDDFT and the first-order nonlinear differential equations that are commonly examined in the mathematical literature: (1) the coupled nature of the TDKS equations, (2) the time-dependent external potential, and (3) the Hartree and exchange-correlation potentials. The first is a result of the density, which is defined using a sum over all occupied Kohn–Sham orbitals, coupling the TDKS equation through the nonlinear potential functionals. Second, the external potential is a time-dependent linear part of the equation; no such term has been incorporated in the above mentioned studies of nonlinear ordinary differential equations. Lastly, the Hartree and exchange-correlation potentials cause the TDKS equation to be an integro-differential equation, involving both integral and derivative operators. These considerations make clear the need to test these techniques within RT-TDDFT calculations in order to assess their potential enhancement of accuracy and functionality.

The exponential integrators may be introduced by first analyzing the TDKS equation in terms of the Kohn–Sham Hamiltonian matrix, $\mathbf{H}^{\mathrm{KS}}$ and the vectorized Kohn–Sham orbitals, Φ_n,

$$i\hbar\frac{\partial}{\partial t}\Phi(t) = \mathbf{H}^{\mathrm{KS}}(t)\Phi(t). \tag{5.22}$$

Here, Φ indicates the set of all Kohn–Sham orbitals, $\Phi = \{\Phi_1, \Phi_1, \ldots\}$. The right-hand side is separated as

$$\mathbf{H}^{\mathrm{KS}}(t)\Phi(t) = \mathbf{L}\Phi(t) + \mathbf{N}(\Phi, t), \tag{5.23}$$

where the linear part is defined by the matrix,

$$\mathbf{L} = \mathbf{T} + \mathbf{V}, \tag{5.24}$$

comprised of the kinetic energy matrix, $\mathbf{T}$, and linear time-independent potential $\mathbf{V}$. The nonlinear part is defined by the potential functionals in the Kohn–Sham Hamiltonian,

$$\mathbf{N}(\Phi, t) = \mathbf{V}^{\mathrm{N}}(\Phi, t)\Phi(t). \tag{5.25}$$

This nonlinear part depends on all orbitals, thereby coupling the differential equations. This nonlinear potential, $\mathbf{V}^{\mathrm{N}}$, is the sum of the Hartree and exchange-correlation potentials, plus the time-dependent potential. The latter is a linear term, but in the following formalism it is more convenient to absorb it into $\mathbf{V}^{\mathrm{N}}$, preserving the time-independence of $\mathbf{L}$.

5.4.1 Integrating Factor Method

In the IF method, the differential equation is multiplied by an integrating factor, thereby introducing new variables. Ideally, one may change the variables in order to solve the linear part exactly and use some technique in order to address the remaining nonlinear part. In the present context, one may define the integrating factor as $\mathrm{e}^{i\mathbf{L}t/\hbar}$ and define the new variables

$$\Psi_n = \mathrm{e}^{-i\mathbf{L}t/\hbar}\Phi_n. \tag{5.26}$$

By multiplying Eq. (5.22) by this integration factor, one obtains

$$i\hbar\frac{\partial}{\partial t}\Psi = \mathrm{e}^{-i\mathbf{L}t/\hbar}\mathbf{N}(\mathrm{e}^{i\mathbf{L}t/\hbar}\Psi, t), \tag{5.27}$$

where, again, Ψ indicates the set $\{\Psi_1, \Psi_2, \ldots\}$. This approach is similar to the interaction picture in quantum mechanics.

The purpose of this transformation is to ameliorate the stiff linear part of the TDKS equations. In the above form, one may use a time stepping method, such as the Runge–Kutta method, to advance the equation in time. Stiffness is not well-defined in the mathematical literature [203, 204], but, in general, this term refers to cases when an implicit Euler method would be more efficient than the explicit Euler method. In the present case of the TDKS equations, or even the TDSE, the largest eigenvalues result from the kinetic energy and laser field terms of the Hamiltonian. If the real space grid approach is applied, and, thus, a finite difference representation is used for the kinetic energy matrix, then the Laplacian operator eigenvalues can vary greatly, and the ratio of the largest to smallest eigenvalue is then very large, leading to a stiff problem. The degree of stiffness would then depend on the grid spacing used.

The disadvantage of the IF method is that it changes the fixed points of the original differential equation, and the local truncation error is larger than in other methods such as

ETD [198]. While in the following applications of the IF method for describing the TDKS equations this consideration appears to be of little concern, it may play a role in determining the method's ability to perform long time propagation.

Integrating Factor Method with Explicit Multistep

Eq. (5.27) can be solved using the most popular integration schemes. Using the Adam-Bashforth method [205], one may derive the following update scheme which is $\mathcal{O}(\Delta t^3)$ accurate in time (IFAB2):

$$\begin{aligned}&\Phi(t_{m+1}) = \\ &\quad \mathrm{e}^{i\mathbf{L}\Delta t/\hbar}\Phi(t_m) + \frac{3i\Delta t}{2\hbar}\mathrm{e}^{i\mathbf{L}\Delta t/\hbar}\mathbf{N}(\Phi(t_m), t_m) - \frac{i\Delta t}{2\hbar}\mathrm{e}^{-2i\mathbf{L}\Delta t}\mathbf{N}(\Phi(t_{m-1}), t_{m-1}).\end{aligned} \tag{5.28}$$

Integrating Factor Method with Fourth-Order Runge–Kutta

By applying the RK4 method to Eq. (5.27) and transforming the new variables, Ψ_n, back to Φ_n, one achieves a new time propagation scheme of accuracy $\mathcal{O}(\Delta t^3)$ (IFRK4),

$$\begin{aligned}\Phi(t_{m+1}) &= \mathrm{e}^{i\mathbf{L}\Delta t/\hbar}\Phi(t_m) + \frac{1}{6}\mathrm{e}^{i\mathbf{L}\Delta t/\hbar}\Psi^{(1)} + \frac{1}{3}\mathrm{e}^{i\mathbf{L}\Delta t/2\hbar}\left(\Psi^{(2)} + \Psi^{(3)}\right) + \frac{1}{6}\Psi^{(4)} \\ \Psi^{(1)} &= \frac{-i}{\hbar}\Delta t\mathbf{N}\left(\Phi(t_m), t_m\right) \\ \Psi^{(2)} &= \frac{-i}{\hbar}\Delta t\mathbf{N}\left(\left[\mathrm{e}^{i\mathbf{L}\Delta t/2\hbar}\left(\Phi(t_m) + \frac{1}{2}\Psi^{(1)}\right)\right], t_{m+1/2}\right) \\ \Psi^{(3)} &= \frac{-i}{\hbar}\Delta t\mathbf{N}\left(\left[\mathrm{e}^{i\mathbf{L}\Delta t/2\hbar}\Phi(t_m) + \frac{1}{2}\Psi^{(2)}\right], t_{m+1/2}\right) \\ \Psi^{(4)} &= \frac{-i}{\hbar}\Delta t\mathbf{N}\left(\left[\mathrm{e}^{i\mathbf{L}\Delta t/\hbar}\Phi(t_m) + \mathrm{e}^{i\mathbf{L}\Delta t/2\hbar}\Psi^{(3)}\right], t_{m+1}\right).\end{aligned} \tag{5.29}$$

The same scheme can be applied for the case of the second-order Runge–Kutta method (IFRK2) [205].

5.4.2 Exponential Time Differencing Method

The ETD method makes use of the identity

$$i\hbar\frac{\partial}{\partial t}\left[\mathrm{e}^{i\mathbf{L}t/\hbar}\Phi(t)\right]=\mathrm{e}^{i\mathbf{L}t/\hbar}\left[-\mathbf{L}\Phi(t)+i\hbar\frac{\partial}{\partial t}\Phi(t)\right], \tag{5.30}$$

which allows Eq. (5.22) to be rewritten as

$$i\hbar\frac{\partial}{\partial t}\left[\mathrm{e}^{i\mathbf{L}t/\hbar}\Phi(t)\right]=\mathrm{e}^{i\mathbf{L}t/\hbar}\mathbf{N}(\Phi,t). \tag{5.31}$$

By integrating this equation from t_m to t_{m+1} and rearranging terms, one may arrive at

$$\Phi(t_{m+1})=\mathrm{e}^{-i\mathbf{L}\Delta t/\hbar}\Phi(t_m)-\mathrm{e}^{i\mathbf{L}(t_{m+1})/\hbar}\frac{i}{\hbar}\int_{t_m}^{t_{m+1}}\mathrm{e}^{i\mathbf{L}\tau/\hbar}\mathbf{N}(\Phi,\tau)d\tau. \tag{5.32}$$

This equation is exact. The simple difference of this form from the IF method is that one maintains Φ as the variables.

In the above derivation, it has been assumed that $\mathbf{L}$ is time-independent and that all time-dependent potential terms may be found within the definition of $\mathbf{N}(\Phi,t)$. However, one may instead include linear time-dependent terms, $\mathbf{V}^{\mathrm{L}}(t)$, within $\mathbf{L}$ and arrive at the same conclusion as Eq. (5.32) if it can be assumed that $\mathbf{V}^{L}(t_m)\approx\mathbf{V}^{L}(t_{m+1})$ [205].

In practice, the integral in Eq. (5.32) is evaluated via some approximation. In the evaluation of this integral, matrix-valued functions arise such as $f(\mathbf{L})=\mathrm{e}^{-i\mathbf{L}\Delta t/\hbar}$ and $f(\mathbf{L})=\mathbf{L}^{-1}$. These functions must be evaluated efficiently for applications [206, 207]. One may calculate the matrix exponentials by Taylor expansion and obtain other needed matrix-valued functions by recurrence relations [208]. In the case of large basis sizes, and thus large matrices, one may efficiently evaluate matrix-valued functions in a Krylov subspace [207, 209]. For methods requiring the calculation of $\mathbf{L}^{-1}$, problems may arise due to small eigenvalues. Following Ref. [198], one may simply eliminate these eigenvalues from the calculation in order to define a pseudo-inverse which may serve in place of $\mathbf{L}^{-1}$.

Exponential Time Differencing with Constant Nonlinear Term

Assuming that the nonlinear term is constant during the time step $t_m \to t_{m+1}$, that is

$$\mathbf{N}(\Phi, \tau) = \mathbf{N}(\Phi(t_m), t_m) \quad (t_m < \tau < t_{m+1}), \tag{5.33}$$

the time propagation update scheme becomes (ETD1)

$$\Phi(t_{m+1}) = \mathrm{e}^{i\mathbf{L}\Delta t/\hbar}\Phi(t_m) + \mathbf{M}_1\mathbf{N}(\Phi(t_m), t_m), \tag{5.34}$$

where

$$\mathbf{M}_1 = \mathbf{L}^{-1}\left(\mathrm{e}^{i\mathbf{L}\Delta t/\hbar} - \mathbf{I}\right). \tag{5.35}$$

Here, $\mathbf{I}$ is the identity matrix.

Exponential Time Differencing with Linearly Raising Nonlinear Term

Instead of the assumption of a constant nonlinear term, a better approximation would be

$$\mathbf{N}(\Phi, \tau) = \mathbf{N}(\Phi(t_m), t_m) + \frac{\Delta\mathbf{N}}{\Delta t}(\tau - t_m) \quad (t_m < \tau < t_{m+1}), \tag{5.36}$$

where $\Delta\mathbf{N} = [\mathbf{N}(\Phi(t_m), t_m) - \mathbf{N}(\Phi(t_{m-1}), t_{m-1})]$. With this assumption, the time propagation update scheme becomes (ETD2)

$$\Phi(t_{m+1}) = \mathrm{e}^{i\mathbf{L}\Delta t/\hbar}\Phi(t_m) + \mathbf{M}_1\mathbf{N}(\Phi(t_m), t_m) - \frac{i\hbar}{\Delta t}\mathbf{M}_2\Delta\mathbf{N}, \tag{5.37}$$

where

$$\mathbf{M}_2 = \mathbf{L}^{-1}\left(\mathbf{M}_1 + \frac{i\Delta t}{\hbar}\mathbf{I}\right). \tag{5.38}$$

The accuracy of this scheme scales as $\mathcal{O}(\Delta t^3)$.

Exponential Time Differencing with Constant Nonlinear Term, Separating the Wave Function

By assuming that the nonlinear potential is constant during the time step $t_m \rightarrow t_{m+1}$, that is

$$\mathbf{V}^{\mathrm{N}}(\Phi, \tau) = \mathbf{V}(\Phi(t_m), t_m) \quad (t_m < \tau < t_{m+1}), \tag{5.39}$$

one can integrate Eq. (5.32) using the trapezoidal rule. This leads to the following relationship:

$$\left[\mathbf{I} + \frac{i}{\hbar}\mathbf{V}(\Phi(t_m), t_m)\Delta t\right] \Phi(t_{m+1}) = \mathrm{e}^{i\mathbf{L}\Delta t/\hbar} \left[\mathbf{I} - \frac{i}{\hbar}\mathbf{V}(\Phi(t_m), t_m)\Delta t\right] \Phi(t_m). \tag{5.40}$$

This is similar to the Crank–Nicolson propagation technique, Sec. 5.3.2, but with an extra factor of $\mathrm{e}^{i\mathbf{L}\Delta t/\hbar}$. By evaluating the inverse of the leftmost operator, one may arrive at another time propagation update scheme which approximates the discrete time step time evolution operator (ETDCN),

$$\Phi(t_{m+1}) = \left[\mathbf{I} + \frac{i}{\hbar}\mathbf{V}(\Phi(t_m), t_m)\Delta t\right]^{-1} \mathrm{e}^{i\mathbf{L}\Delta t/\hbar} \left[\mathbf{I} - \frac{i}{\hbar}\mathbf{V}(\Phi(t_m), t_m)\Delta t\right] \Phi(t_m). \tag{5.41}$$

Exponential Time Differencing with Fourth-Order Runge–Kutta

In the application of the RK4 method to the ETD approach, one must define the following set of vectors:

$$\begin{aligned}
\Psi^{(a)} &= \varphi_0\left(\frac{\beta}{2}\mathbf{L}\right)\Phi(t_m) + \frac{\beta}{2}\varphi_1\left(\frac{\beta}{2}\mathbf{L}\right)\mathbf{N}(\Phi(t_m), t_m), \\
\Psi^{(b)} &= \varphi_0\left(\frac{\beta}{2}\mathbf{L}\right)\Phi(t_m) + \frac{\beta}{2}\varphi_1\left(\frac{\beta}{2}\mathbf{L}\right)\mathbf{N}(\Psi^{(a)}, t_{m+1/2}) \\
\Psi^{(c)} &= \varphi_0\left(\frac{\beta}{2}\mathbf{L}\right)\Psi^{(a)} + \frac{\beta}{2}\varphi_1\left(\frac{\beta}{2}\mathbf{L}\right)\left[2\mathbf{N}(\Psi^{(b)}, t_{m+1/2}) - \mathbf{N}(\Phi(t_m), t_m)\right],
\end{aligned} \tag{5.42}$$

where $\beta = -i\Delta t/\hbar$ and the φ-functions are defined in Appendix C of Ref. [205]. One may then define the update scheme (ETDRK4)

$$\Phi(t_{m+1}) = \mathrm{e}^{-i\mathbf{L}\Delta t/\hbar}\Phi(t_m) + \beta\left[\varphi_1(\beta\mathbf{L})\mathbf{K}_1 + \varphi_2(\beta\mathbf{L})\mathbf{K}_2 + \varphi_3(\beta\mathbf{L})\mathbf{K}_3\right], \tag{5.43}$$

where

$$\begin{aligned}
\mathbf{K}_1 =& \mathbf{N}(\Phi(t_m), t_m) \\
\mathbf{K}_2 =& -3\mathbf{N}(\Phi(t_m), t_m) + 2\mathbf{N}(\Psi^{(a)}, t_{m+1/2}) + 2\mathbf{N}(\Psi^{(b)}, t_{m+1/2}) - \mathbf{N}(\Psi^{(c)}, t_{m+1}) \\
\mathbf{K}_3 =& 4\left[\mathbf{N}(\Phi(t_m), t_m) - \mathbf{N}(\Psi^{(a)}, t_{m+1/2}) - \mathbf{N}(\Psi^{(b)}, t_{m+1/2}) + \mathbf{N}(\Psi^{(c)}, t_{m+1})\right].
\end{aligned} \tag{5.44}$$

A similar technique can be achieved based on the RK2 method (ETDR2) [205].

Krogstad Time Propagation

The ETDRK4 method was further developed in Ref. [210] using a truncated Taylor expansion of the nonlinear part in order to increase the accuracy. It is only different from the above described ETDRK4 method by the definition of the $\Psi^{(a)}$, $\Psi^{(b)}$, and $\Psi^{(c)}$ functions:

$$\begin{aligned}
\Psi^{(a)} =& \varphi_0\left(\frac{\beta}{2}\mathbf{L}\right)\Phi(t_m) + \frac{\beta}{2}\varphi_1\left(\frac{\beta}{2}\mathbf{L}\right)\mathbf{N}(\Phi(t_m), t_m) \\
\Psi^{(b)} =& \varphi_0\left(\frac{\beta}{2}\mathbf{L}\right)\Phi(t_m) + \frac{\beta}{2}\varphi_1\left(\frac{\beta}{2}\mathbf{L}\right)\mathbf{N}(\Phi(t_m), t_m) \\
&+ \beta\varphi_2\left(\frac{\beta}{2}\mathbf{L}\right)\left[\mathbf{N}(\Phi^{(a)}, t_{m+1/2}) - \mathbf{N}(\Phi(t_m), t_m)\right] \\
\Psi^{(c)} =& \varphi_0\left(\beta\mathbf{L}\right)\Phi(t_m) + \beta\varphi_1\left(\beta\mathbf{L}\right)\mathbf{N}(\Phi(t_m), t_m) \\
&+ 2\beta\varphi_2\left(\beta\mathbf{L}\right)\left[\mathbf{N}(\Phi^{(b)}, t_{m+1/2}) - \mathbf{N}(\Phi(t_m), t_m)\right].
\end{aligned} \tag{5.45}$$

5.5 Computational Details and Results for One-Dimensional Helium

In order to test these approaches, each propagation method has been employed to represent a simple one-dimensional helium atom model which has been often used in similar test calculations [211]. The Hamiltonian in this case is

$$H = -\frac{\hbar^2}{2m}\frac{\partial^2}{\partial x^2} + V(x) + V^{\text{laser}}(x,t) + V^{\text{H}}[\rho](x,t) + V^{\text{ex}}[\rho](x,t). \tag{5.46}$$

Here, $V(x)$ is a sot Coulomb potential [212, 213] for $Z = 2$,

$$V(x) = \frac{-2}{\sqrt{a^2 + x^2}}, \tag{5.47}$$

where, in the following calculations, the parameter a has been set to 1. Two models for the two-electron density are used,

$$\rho(x,t) = 2|\Phi_1(x,t)|^2 \quad \text{(model A)} \tag{5.48}$$

and

$$\rho(x,t) = |\Phi_1(x,t)|^2 + |\Phi_2(x,t)|^2 \quad \text{(model B)}, \tag{5.49}$$

where Φ_1 and Φ_2 are initialized as the first two eigenstates of the ground state Kohn–Sham Hamiltonian at $t = 0$. Model A is an uncoupled system, while, in model B, the two state are coupled, leading to more complicated nonlinear effects.

The one-dimensional Hartree potential is calculated as

$$V^{\mathrm{H}}[\rho](x,t) = \frac{e^2}{4\pi\varepsilon_0} \int \frac{\rho(y,t)}{\sqrt{(x-y)^2 + a^2}} dy, \tag{5.50}$$

with the same value for a. The exchange-correlation potential used is given by the exact-exchange approximation [213],

$$V^{\mathrm{ex}}[\rho](x,t) = -\frac{1}{2} V^{\mathrm{H}}[\rho](x,t). \tag{5.51}$$

The electric field, $E(t)$ has been incorporated via the dipole approximation and use of the length gauge representation for the orbitals leading to

$$V^{\mathrm{laser}}(x,t) = E(t)x. \tag{5.52}$$

This term may be incorporated within either the linear part, resulting in a time-dependent $\mathbf{L}$, or the nonlinear part, preserving the time-independence of $\mathbf{L}$. In the latter case, the two parts take the form

$$\mathbf{L} = -\frac{\hbar^2}{2m}\frac{\partial^2}{\partial t^2} + V(x) \tag{5.53}$$

$$\mathbf{N}(\Phi, t) = \left(V^{\text{laser}}(x,t) + V_H[\rho](x,t) + V_{ex}[\rho](x,t)\right)\Phi(t). \tag{5.54}$$

Two types of TDDFT calculations were performed using this model. In the first, the orbitals were chosen to be in an excited state at $t = 0$. Such an initial condition causes immediate fluctuations in the electron density upon propagation which, in turn, cause rapid changes in the nonlinear part, $\mathbf{N}$. In these calculations, the electric field was kept at zero so that only the nonlinear potentials were time-dependent. The computational box was of width 160 Bohr, and a complex absorbing potential (CAP) [214] was added at the boundaries in order to allow some ionization which occurs early in the simulation.

In the second type of calculation, the orbitals were initialized in the natural ground state by diagonalizing the ground state Kohn–Sham Equation, and a laser field was used to excite the system. The form of this field was a variation of the smooth turn-on pulse [160],

$$E(t) = \begin{cases} E_0 \sin\left(\dfrac{\pi t}{2T_r}\right)\sin(\omega t), & \text{if } 0 \le t \le T_r, \\ \\ E_0 \sin(\omega t), & \text{otherwise,} \end{cases} \tag{5.55}$$

where the frequency, ω, and ramping time, T_r, were set to 0.148 a.u. and $6/\omega$, respectively. Simulations were carried out for maximum electric fields, E_0, of both 0.1 a.u. (5.14 V/Å) and 1.0 a.u. (51.4 V/Å). The computational box in these cases was of width 400 Bohr. In both types of calculations, the wave functions were represented using a sinc basis, Eq. (4.2), with the Kinetic energy being represented by the full matrix of Eq. (4.3).

Benchmark calculations were performed using the Taylor time propagator, Eq. (5.13), using a time step size of 10^{-5} a.u., where 1 atomic time unit equals 0.0241 femtoseconds.

These time step sizes are 1000 times smaller than those needed for stability and ensure dramatic accuracy. The wave functions resulting from the various methods are compared to the benchmark calculations (B) by use of the Tanimoto index [215],

$$\sigma_i(t) = \frac{I_{Bi}(t)}{I_{BB}(t) + I_{ii}(t) - I_{Bi}(t)}, \tag{5.56}$$

where

$$I_{ij}(t) = \int |\Phi_i^*(x,t)\Phi_i(x,t)|dx. \tag{5.57}$$

This metric ranges in value between zero and one, with the latter indicating a perfect match. This similarity measurement takes into account whether the two functions differ by a constant; thus, the wave functions are not normalized at each time step. In practice, it is more convenient to discuss the time averaged agreement,

$$\sigma_{(T_i \to T_f),i} = \frac{1}{T_f - T_i} \int_{T_i}^{T_f} \sigma_i(t)dt \tag{5.58}$$

defined within the given temporal range, T_i to T_f. The time-averaged error may then be determined as $1 - \sigma_T$.

A summary of the operation count, number of times the TDDFT functionals must be updated per time step, and accuracy scaling for each propagation technique used below is presented in Table 5.1. Each propagation technique is expected to scale linearly with respect to the number of electrons, with the exception of the Runge–Kutta-type methods, in which case the scaling is affected by the number of times that the TDDFT functionals must be updated. Descriptions of the implicit-explicit (IMEX) methods may be found in Ref. [205]. The following data and figures are reproduced from Ref. [205] with the permission of the American Physical Society.

Method	Operations	Hartree	Accuracy
Taylor	4	1	$\mathcal{O}(\Delta t^4)$
SPO	1	1	$\mathcal{O}(\Delta t^3)$
CN	2	1	$\mathcal{O}(\Delta t^2)$
RK2	2	2	$\mathcal{O}(\Delta t^2)$
RK4	4	4	$\mathcal{O}(\Delta t^4)$
AB2AM2	2	1	$\mathcal{O}(\Delta t^3)$
IFAB2	3	1	$\mathcal{O}(\Delta t^3)$
IFRK2	3	2	$\mathcal{O}(\Delta t^3)$
IFRK4	3	4	$\mathcal{O}(\Delta t^4)$
ETD1	2	1	$\mathcal{O}(\Delta t^2)$
ETD2	3	1	$\mathcal{O}(\Delta t^3)$
ETDCN	3	1	$\mathcal{O}(\Delta t^3)$
ETDRK2	3	2	$\mathcal{O}(\Delta t^3)$
ETDRK4	8	4	$\mathcal{O}(\Delta t^4)$
Krogstad	9	4	$\mathcal{O}(\Delta t^4)$

Table 5.1: The main computational effort per time step is matrix vector multiplication (Operations) and solution of the Poisson equation (Hartree). All matrices dependent upon $\mathbf{L}$ are considered to be constant in time so that they must be calculated only once. The table is separated into three sections: time evolution operator and direct numerical integration methods (top), in which the complete Hamiltonian is used to propagate the wave function, IMEX methods (middle), and exponential integrator methods (bottom). Both of the latter two groups split the TDKS equations into linear and nonlinear parts.

5.5.1 Excited State Superposition

First, the single-orbital case is considered. This orbital is initialized as a superposition in equal measure of the ground and first excited eigenstates of the ground state Hamiltonian. Upon propagation, the orbital is free to develop without external perturbation. Thus, the only time-dependent potentials are the nonlinear functionals of TDDFT.

Figure 5.1 shows the error associated with various techniques for propagating the TDKS equations describing this system. Of the time evolution operator techniques—Taylor, CN, and SPO—each appear to exhibit comparable error in these simulations when stable. Taylor propagation yields values similar to the CN and SPO methods for time step sizes up to $\Delta t = 0.02$ a.u., after which it becomes unstable. For these methods, the largest time step

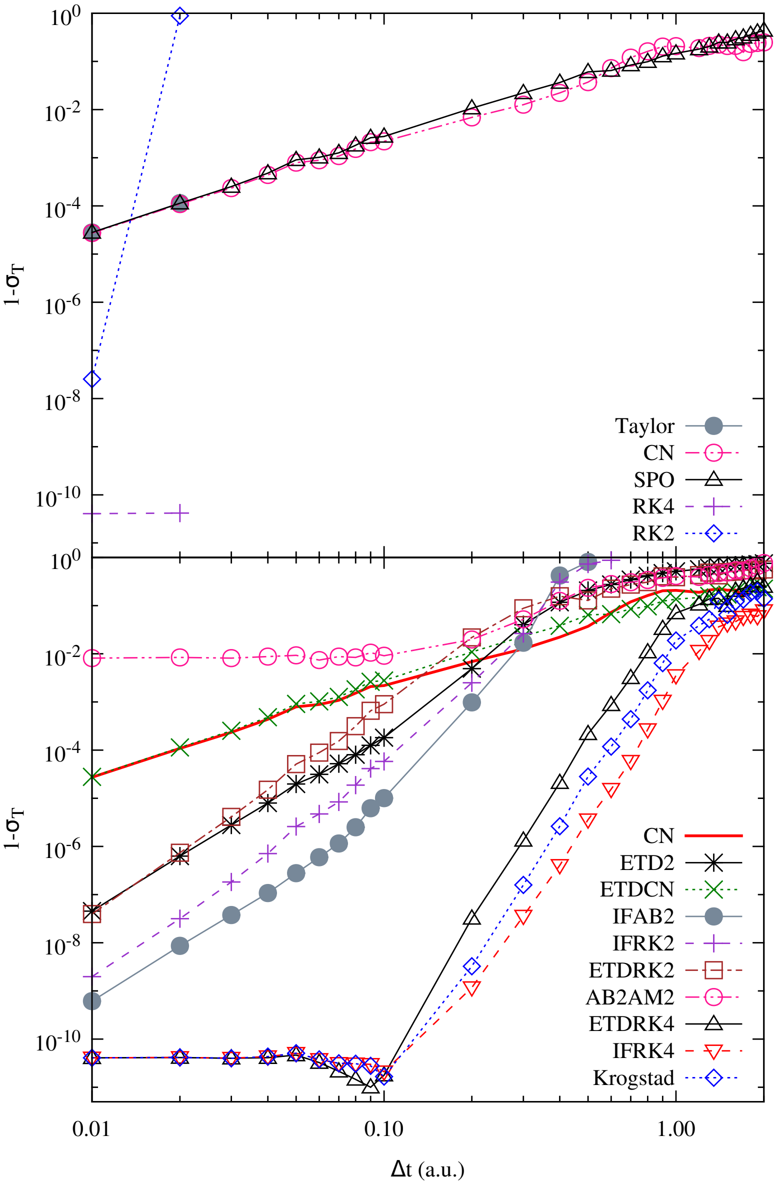

Figure 5.1: The time-averaged error of various methods for integrating the TDKS equations when electrons are initialized in an excited state. The time interval considered was between $T_i = 10$ a.u. and $T_f = 100$ a.u. Time evolution operator and direct numerical integration approaches are shown above while IMEX, IF, and ETD approaches are shown below. CN is shown in the latter for comparison.

size which allows for 99% accuracy in the orbital is around $\Delta t = 0.2$ a.u. As for the direct numerical integration methods, RK2 and RK4, these have less error than the time evolution operator techniques but are limited by a maximum time step size.

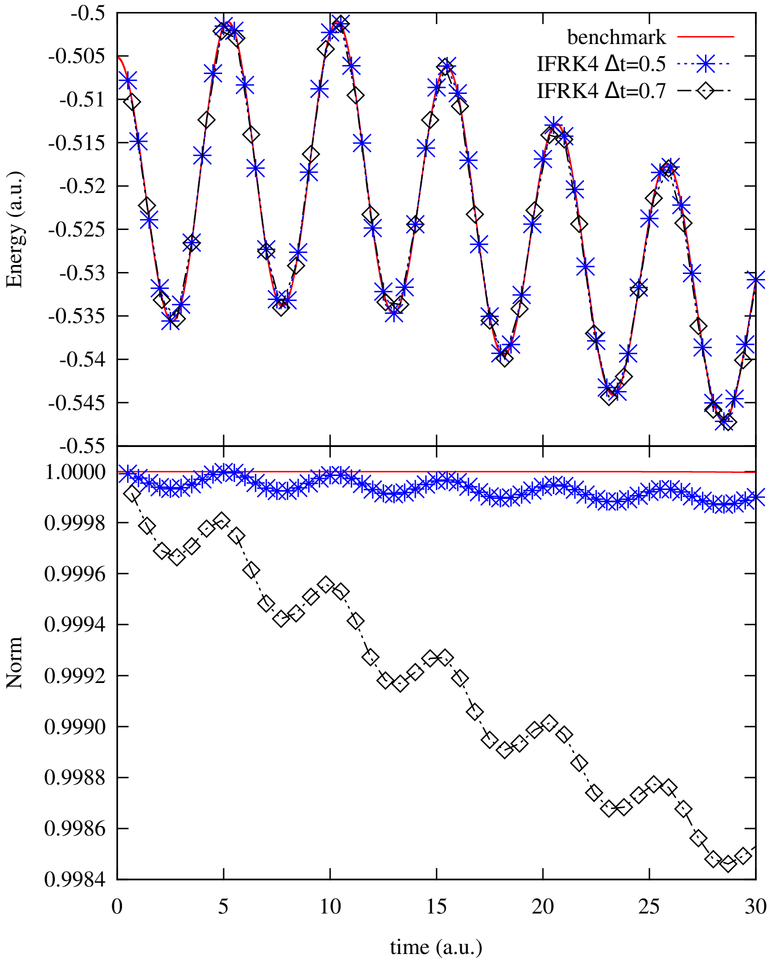

Figure 5.2: The time-dependent energy (above) and norm (below) of the IFRK4 integration method using time step sizes of 0.5 and 0.7 a.u. as compared to a benchmark calculation.

The IF and ETD methods perform much better than the time evolution operator and direct numerical integration techniques, indicated by smaller error for larger time step sizes. Of methods scaling as $\mathcal{O}(\Delta t^3)$, the IFRK2 and IFAB2 methods perform marginally better than the ETDRK2 method. For each of these, the maximum time step size which maintains 99% accuracy is around 0.2 to 0.3 a.u. Of methods scaling as $\mathcal{O}(\Delta t^4)$, IFRK4 does best, with Krogstad outperforming ETDRK4 integration and a maximum time step size for each near 1.0 a.u.

The energy oscillates with a period of 5 a.u. in these calculations, as shown in Fig. 5.2.

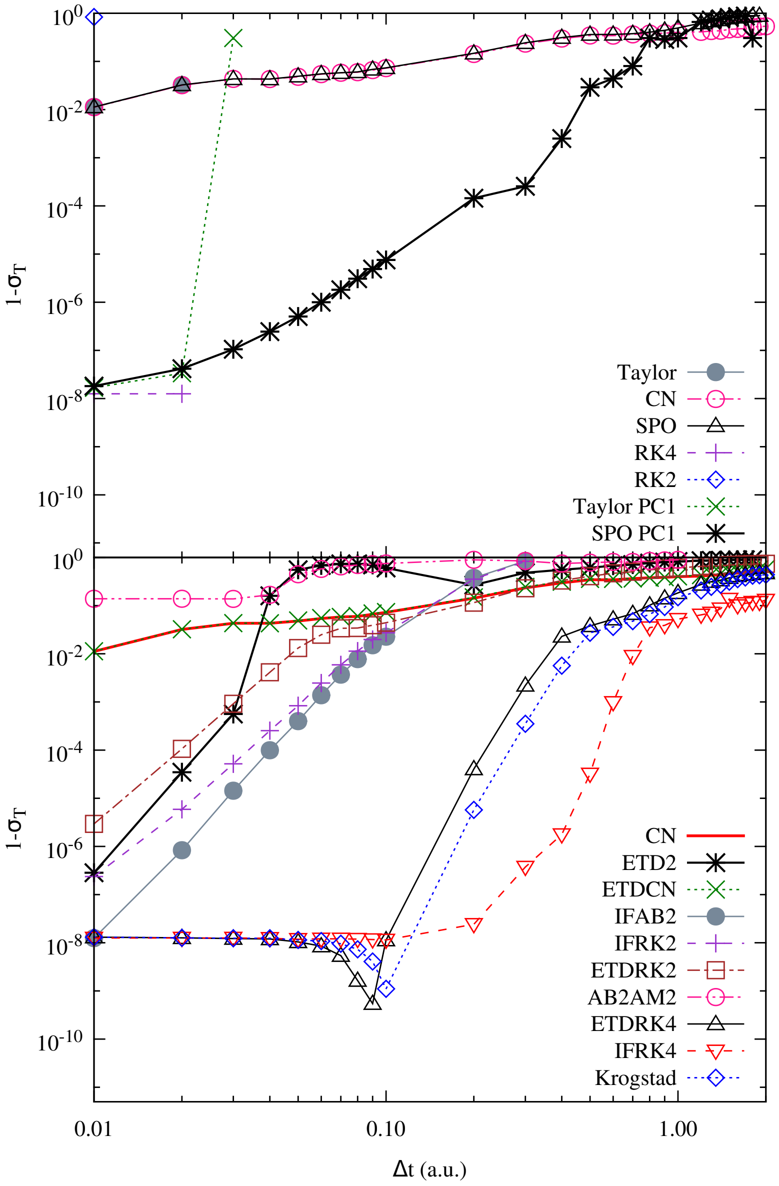

Figure 5.3: The time-averaged error of various methods for integrating the TDKS equations over a long time period. The time interval considered was between $T_i = 10$ a.u. and $T_f = 1000$ a.u. Time evolution operator and direct numerical integration approaches are shown above while IMEX, IF, and ETD approaches are shown below. CN is shown in the latter for comparison.

The IFRK4 method is seen to be capable of accurately producing the proper energy curve for even large choices of time step size near 0.7 a.u., while the norm deviates at a rate of only about 5×10^{-5} fs^{-1}.

For longer simulations, the nonlinear nature of the TDKS equations requires accurate integration in time. As a rigorous test of the methods considered here, a long ($T_f = 1000$ a.u.) simulation was performed using each. The results are shown in Fig. 5.3. Here, the time evolution operator and direct numerical integration methods fail to maintain accuracy over the course of the simulation. This is because the error associated with assuming the total Hamiltonian to be constant between steps accumulates throughout the simulation and is exacerbated by the rapidly changing nonlinear potential in this case. These methods can be improved by modification using predictor-corrector schemes. The maximum time step sizes for the ETDRK4 and Krogstad methods are near 0.3 a.u., while the IFRK4 method performs well up to time step sizes of around 0.5 a.u.

5.5.2 Laser-Driven Dynamics of a Single Orbital

The collection of methods was also tested with application to describing laser-driven dynamics. In these simulations, a single orbital was used, initialized in the ground state of the $t = 0$ Hamiltonian, and the density was defined using model A. Tests including the laser potential, V^{laser}, in the linear part as well as the nonlinear part were both conducted. For the latter, the matrix-valued functions containing $\mathbf{L}$ were updated at each time step. Due to the wide computational box, no ionization was expected and, thus, no CAP was implemented.

The accuracy of the time evolution operator and direct numerical integration methods is shown in Fig. 5.4. The performance of these methods in this case is much better than that of the excited state superposition. This is likely due to the fact that the orbitals develop more slowly under the the driving influence of the ramped laser rather than that of the previous rapidly changing nonlinear potentials. This allows for the approximation of a constant Hamiltonian between time steps to better describe the dynamics.

Laser Potential in Nonlinear Part

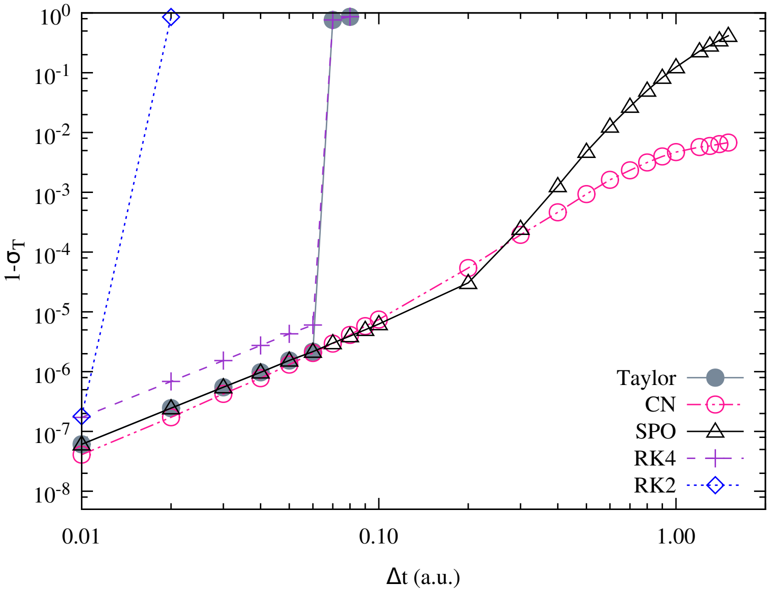

Figure 5.4: The time-averaged error of time evolution operator and direct numerical integration methods for integrating the TDKS equations when electrons are driven by an external electric field of strength 0.1 a.u. The time-dependent potential from the electric field was included in the linear part. The time interval considered was between $T_i = 10$ a.u. and $T_f = 100$ a.u.

The errors associated with the IMEX, IF, and ETD methods for a maximum electric field value of 0.1 a.u. are presented in Fig. 5.5. Methods using RK4-type integration, other than Krogstad, exhibit stability for time step sizes up to about 0.1 a.u. For stable time step sizes, these methods' accuracies are within an order of magnitude of the CN method. However, it appears that the separate numerical integration of the time-dependent nonlinear part hinders the IF and ETD methods such that they are outperformed by the CN method for all choices of time step size. The ETDCN method is able to match the CN method up to time step sizes of about 0.7 a.u. due to its time evolution form.

Laser Potential in Linear Part

By including the laser potential in the linear part, the stability of the IF and ETD methods is significantly enhanced, as shown in Fig. 5.6. There is a clear grouping of $\mathcal{O}(\Delta t^3)$ and $\mathcal{O}(\Delta t^4)$ methods. The RK4-type methods now outperform CN for choices of time step sizes up to about 0.8 a.u.

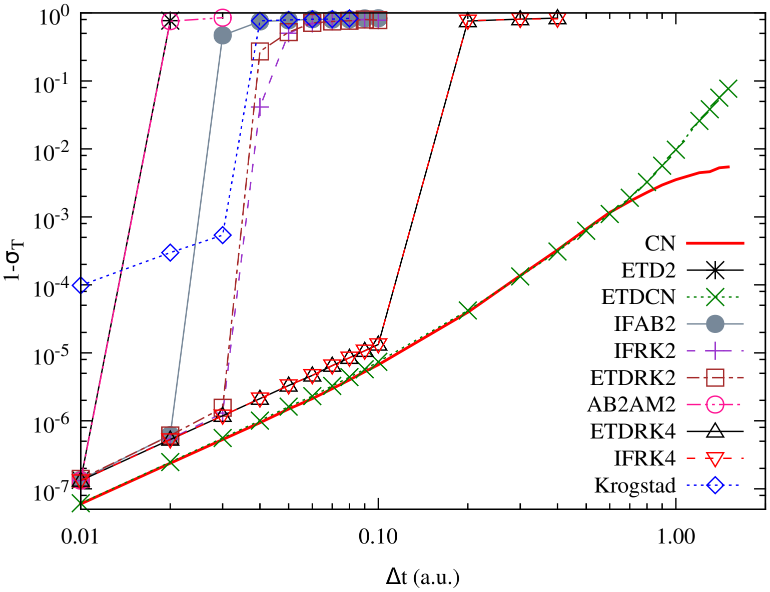

Figure 5.5: The time-averaged error of various methods for integrating the TDKS equations when electrons are driven by an external electric field of strength 0.1 a.u. The time-dependent potential from the electric field was included in the nonlinear part. The time interval considered was between $T_i = 10$ a.u. and $T_f = 100$ a.u. CN is shown for comparison.

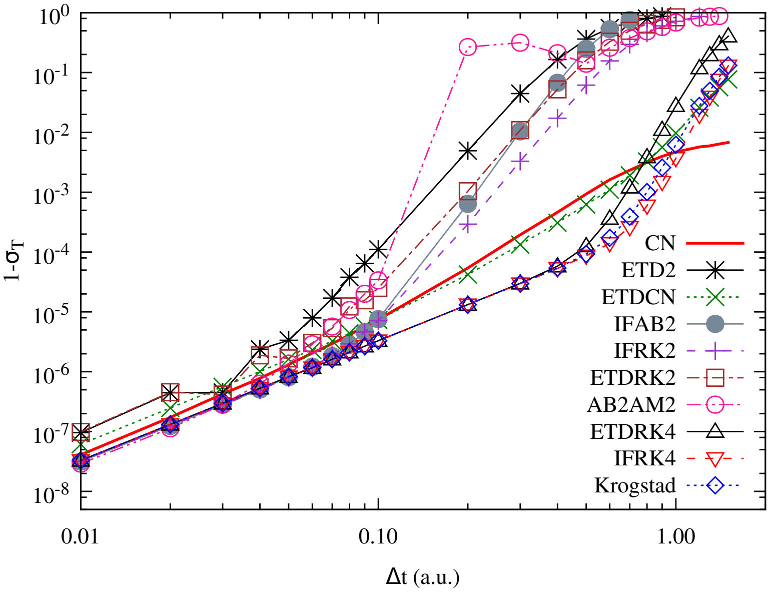

Figure 5.6: The time-averaged error of various methods for integrating the TDKS equations when electrons are driven by an external electric field of strength 0.1 a.u. The time-dependent potential from the electric field was included in the linear part. The time interval considered was between $T_i = 10$ a.u. and $T_f = 100$ a.u. CN is shown for comparison.

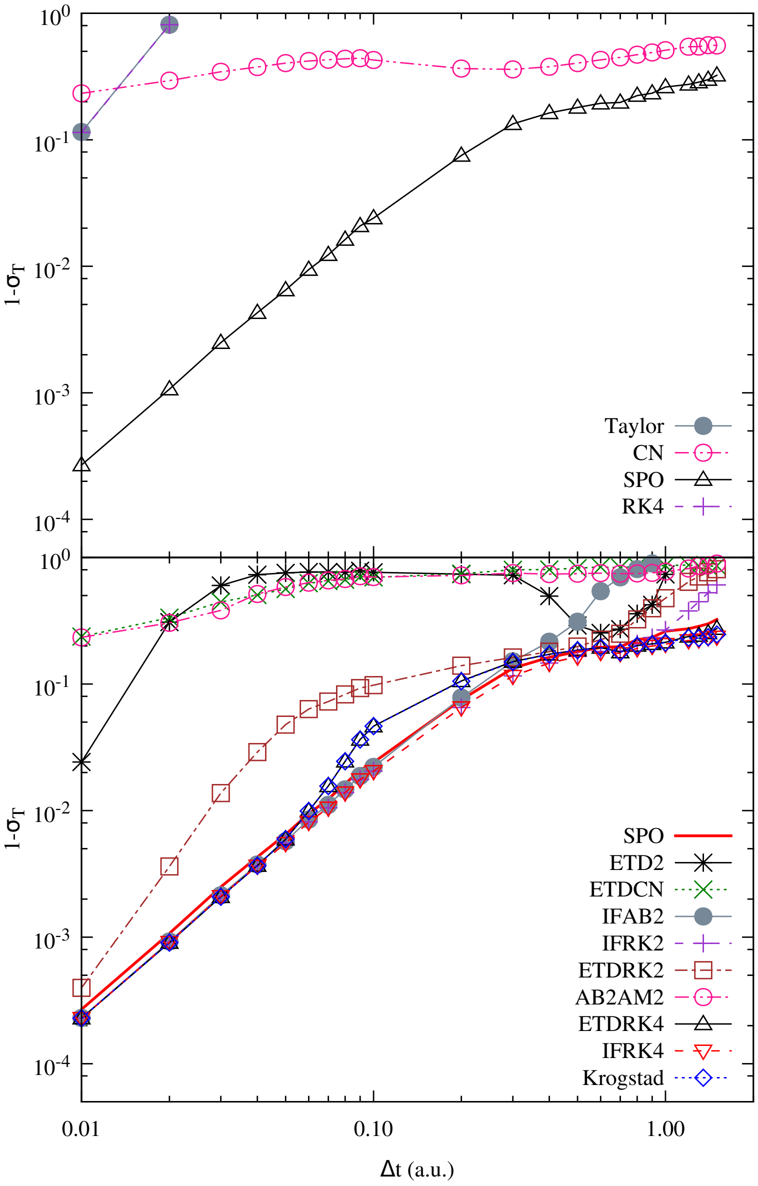

Figure 5.7: The time-averaged error of various methods for integrating the TDKS equations when electrons are driven by a strong external electric field of strength 1.0 a.u. The time-dependent potential from the electric field was included in the linear part. The time interval considered was between $T_i = 10$ a.u. and $T_f = 100$ a.u. SPO is shown for comparison. The second-order Runge–Kutta method is excluded from the top figure due to it being unstable for each choice of time step size.

When a strong laser field is considered, all methods generally perform worse. This is illustrated in Fig. 5.7. In the case of the time evolution operator and direct numerical integration methods, this increased error is due to the large magnitudes of the rapidly changing

Hamiltonian. While the Taylor and CN approximations for the exponential time evolution operator significantly degrade in this case, the SPO approach performs best by far due to its analytical expression for the matrix-exponential form.

In the case of the IF and ETD methods, this degradation in accuracy is due to the breakdown of the approximation that the **L** matrix and its associated matrix-valued functions are constant for the duration of each time step. While the SPO approach performs best out of the time evolution operator methods, IFRK4 is able to match or exceed it for all choices of time step size, while other RK4-type methods maintain similar accuracy. Notably, the ETDRK2 and IFRK2 methods perform surprisingly well in this case, with the latter being nearly indistinguishable from its RK4-type counterpart.

5.5.3 Laser with Two Orbitals

In order to provide a rigorous test of nonlinear contributions, a system comprised of two electrons in separate orbitals, coupled via the Hartree and exchange-correlation potentials, was time propagated under the influence of an external electric field using the collection of methods. The density was determined using model B. The laser was included in the linear part.

The error associated with the lower initial energy orbital is shown in Fig 5.8 and that of the higher initial energy orbital is shown in Fig. 5.9. It appears that the second, higher energy orbital dominates as the larger source of error for most methods. This is to be expected due to the spatial extension and more complicated nodal structure of this orbital. The CN and SPO methods alternate in exhibiting the superior accuracy of the time evolution operator and direct numerical integration methods as the time step size changes for each orbital. Of the IF and ETD methods, IFRK4 and ETDRK4 share similar accuracy for the second orbital, representing the lowest error of any tested method. However, in the case of the first orbital, the IFRK4 method gains an advantage for time step sizes above 0.4 a.u. The reason that the integration methods perform better, in general, for model B is that the

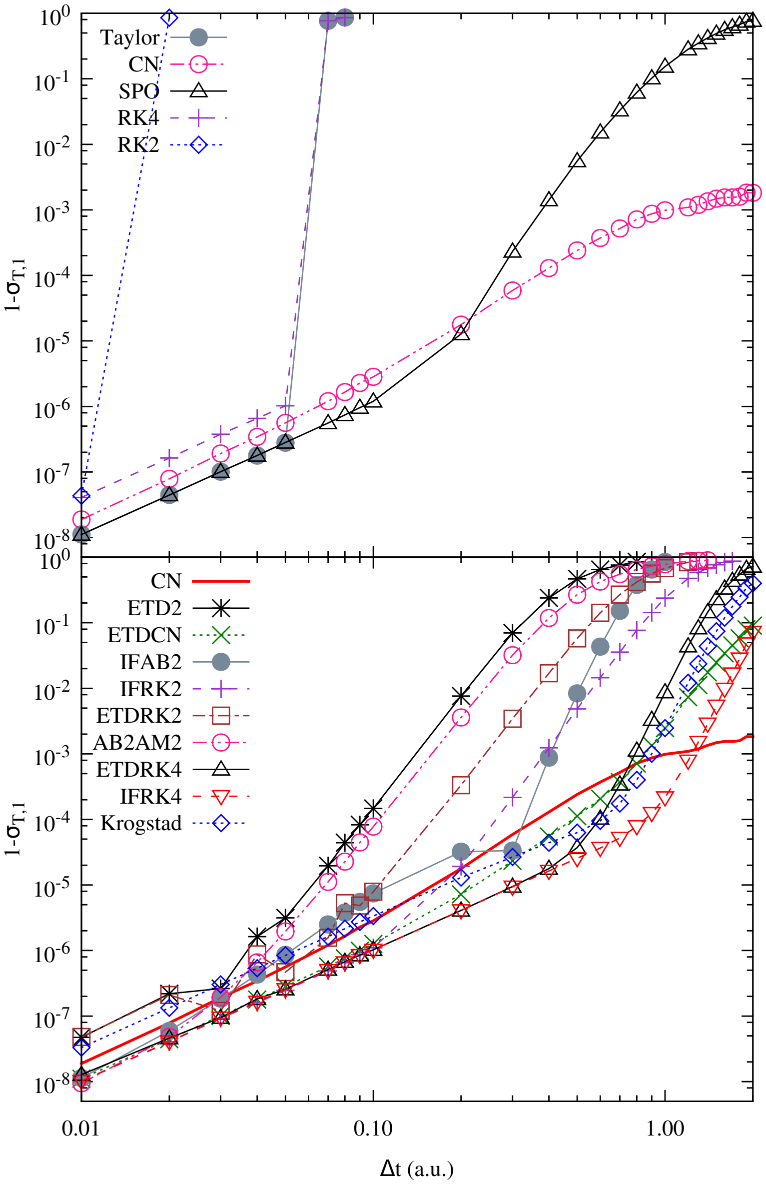

Figure 5.8: The time-averaged error of orbital 1 for model B, using various methods for integrating the TDKS equations when electrons are driven by an external electric field of strength 0.1 a.u. The time interval considered was between $T_i = 10$ a.u. and $T_f = 100$ a.u. Time evolution operator and direct numerical integration approaches are shown above while IMEX, IF, and ETD approaches are shown below. CN is shown in the latter for comparison.

dynamics related to the nonlinear potential occur more slowly than for model A.

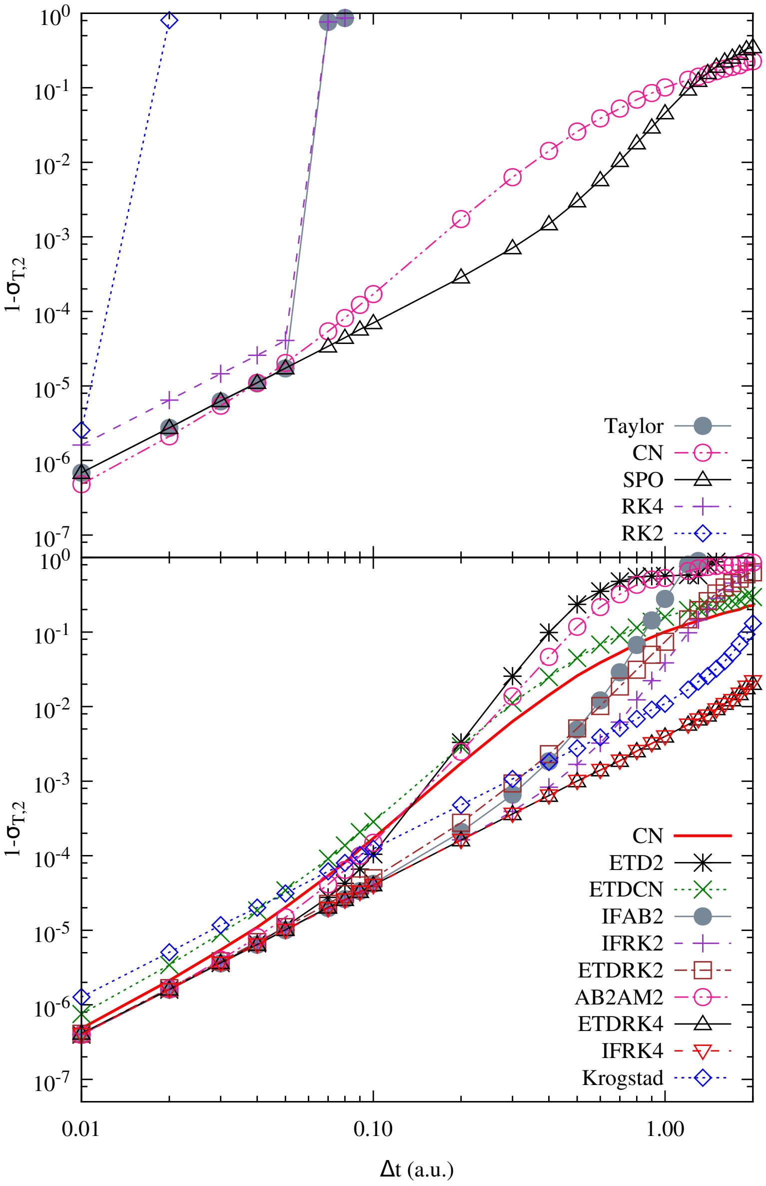

Figure 5.9: The time-averaged error of orbital 2 for model B, using various methods for integrating the TDKS equation when electrons are driven by an external electric field of strength 0.1 a.u. The time interval considered was between $T_i = 10$ a.u. and $T_f = 100$ a.u. Time evolution operator and direct numerical integration approaches are shown above while IMEX, IF, and ETD approaches are shown below. CN is shown in the latter for comparison.

5.6 Summary

Various exponential integrator methods have been implemented within TDDFT and tested against conventional propagation techniques. It has been determined that of the time evolution operator and direct numerical integration methods, the CN and SPO approaches performed best for the test simulations. Typically these two choices yielded similar results; however, in the cases of intense laser fields, SPO was clearly superior. Of the IF and ETD methods, the IFRK4 and ETDRK4 approaches yielded the most accurate results for each of the test cases.

For dynamics driven by a linear, time-dependent potential, the RK4-type exponential integrator methods were able to match the front-runners of the joint time evolution operator and direct numerical integration group, CN or SPO, for both moderate and high laser intensities. In cases where the dynamics were driven by the nonlinear part of the Hamiltonian, the RK4-type exponential integrator methods outperformed even the best suited time evolution operator methods by orders of magnitude.

While the ETD method is typically seen as being the most accurate of the exponential integrators in the mathematical literature, in these results the IF method performed uniformly better, though slightly so. This may be due to a more complicated structure of the nonlinear part in Eq. (5.32) for TDDFT rather than in other equations investigated in the literature where the nonlinear part is typically a y^k term.

Beyond the success of the RK4-type exponential integrators shown in this study, one may note that they may further benefit from the ability of Runge–Kutta approaches to propagate the wave function using variable time step sizes. This implies the capability of dynamically adjusting the time step size throughout simulations in order to best balance the computational cost and accuracy.

In tests including a time-dependent, linear potential associated with a driving laser field, the accuracy when including this term in the linear part far exceeded that of when it was included in the nonlinear part. This implies that in order to achieve the best results, one must update the matrix-valued functions containing the linear part at each time step—an equivalent complication to that of the CN method. While this process may be possible in the case of a compact basis representation, such calculations would be infeasible when dealing with large, sparse matrices related to representations such as the real space grid approach. The inclusion of Krylov subspace expansions, or alternative approaches for the evaluation of these matrix-valued functions in such a scenario remains a topic of future research. A split operator approach, using fast Fourier transforms as explained in Sec. 5.3.3, was tested as a means of approximating the matrix exponential needed for the IFRK4 method. The results of this approach yielded the same improvement of accuracy as those presented above using a diagonalization of the **L** matrix.

Chapter 6

VOLKOV STATE BASIS FOR THE SIMULATION OF PERIODIC SYSTEMS IN INTENSE LASER FIELDS

6.1 Volkov State Basis Set

As described in Chapter 1, field-induced dynamics within periodic systems is a topic of common interest. These laser-matter interactions play a role in the investigation of materials' optical and electrical properties and are the subject of popular studies such as that of recently demonstrated HHG in solids. Up until this point of the thesis, only static basis functions, borrowed from popular DFT implementations, have been discussed for use within TDDFT calculations. In this section, time-dependent basis functions are introduced, which are meant to well-represent laser-induced electron dynamics. These time-dependent functions are chosen as the Volkov states, $\phi^{\mathrm{V}}_{\mathbf{g}}(\mathbf{r}, t)$, defined as the solution to the TDSE for the velocity gauge Hamiltonian, Eq. (2.41),

$$i\hbar\dot{\phi}^{\mathrm{V}}_{\mathbf{g}}(\mathbf{r}, t) = H^{\mathrm{vel}}(t)\phi^{\mathrm{V}}_{\mathbf{g}}(\mathbf{r}, t), \tag{6.1}$$

representing single particles that are free apart from the influence of a uniform external vector potential. The form for these states may be analytically described as

$$\phi^{\mathrm{V}}_{\mathbf{g}}(\mathbf{r}, t) = \frac{1}{\sqrt{\Omega}}\mathrm{e}^{i\mathbf{g}\cdot\mathbf{r}}\mathrm{e}^{-i\varphi^{\mathbf{g}}(t)}, \tag{6.2}$$

which is that of a plane wave modified by a time-dependent phase factor with the Volkov phase defined as

$$\varphi^{\mathbf{g}}(t) = \int_0^t \frac{\hbar^2}{2m}\left[\mathbf{g} + \frac{e}{\hbar}\mathbf{A}(\tau)\right]^2 d\tau. \tag{6.3}$$

A wave function described by such time-dependent basis functions takes the form

$$\psi(\mathbf{r},t) = \sum_{\mathbf{g}} c_{\mathbf{g}}(t)\phi_{\mathbf{g}}(\mathbf{r},t). \tag{6.4}$$

Substitution of this into the TDSE yields

$$i\hbar \sum_{\mathbf{g}} \Big[\dot{c}_{\mathbf{g}}(t)\phi_{\mathbf{g}}(\mathbf{r},t) + c_{\mathbf{g}}(t)\dot{\phi}_{\mathbf{g}}(\mathbf{r},t)\Big] = \sum_{\mathbf{g}} c_{\mathbf{g}}(t) H \phi_{\mathbf{g}}(\mathbf{r},t). \tag{6.5}$$

Of present interest is the description of wave functions resulting from Hamiltonians of the form $H = H^{\text{vel}} + V(t)$. By this substitution and choosing the basis functions to be Volkov states, Eq. (6.5) may be simplified due to the advantageous property $i\hbar\dot{\phi}^{\text{V}}_{\mathbf{g}} = H^{\text{vel}}\phi^{\text{V}}_{\mathbf{g}}$,

$$\sum_{\mathbf{g}} \left[i\hbar\dot{c}_{\mathbf{g}}(t) - c_{\mathbf{g}}(t)V(t)\right]\phi^{\text{V}}_{\mathbf{g}}(\mathbf{r},t) = 0. \tag{6.6}$$

By left-multiplying by $\phi^{\text{V}}_{\mathbf{g}'}(\mathbf{r},t)$ and integrating over $\mathbf{r}$, this equation may be rewritten in the matrix form for a periodic TDDFT application as

$$i\hbar\dot{\mathbf{c}}^{\text{V}}_{n\mathbf{k}}(t) = \mathbf{V}^{\text{V}}(t)\mathbf{c}^{\text{V}}_{n\mathbf{k}}(t). \tag{6.7}$$

Equation (6.7) may be solved using the collection of techniques discussed in Chapter 5.

Here, $\mathbf{V}^{\text{V}}(t)$ indicates the time-dependent Volkov matrix elements which are related to the plane wave matrix elements as

$$V^{\text{V}}_{\mathbf{g}\mathbf{g}'}(t) = \langle\phi^{\text{V}}_{\mathbf{g}}(t)|V(t)|\phi^{\text{V}}_{\mathbf{g}'}(t)\rangle = V^{\text{PW}}_{\mathbf{g}\mathbf{g}'}(t)\mathrm{e}^{i\left(\varphi^{\mathbf{g}}-\varphi^{\mathbf{g}'}\right)}. \tag{6.8}$$

This form makes clear the simplicity of calculating the Volkov state basis matrix elements. One may transform existing plane wave basis programs into Volkov state basis programs in a straightforward manner by calculating the Volkov phase difference via on-the-fly integration of the vector potential and applying the associated phase factor to the plane wave

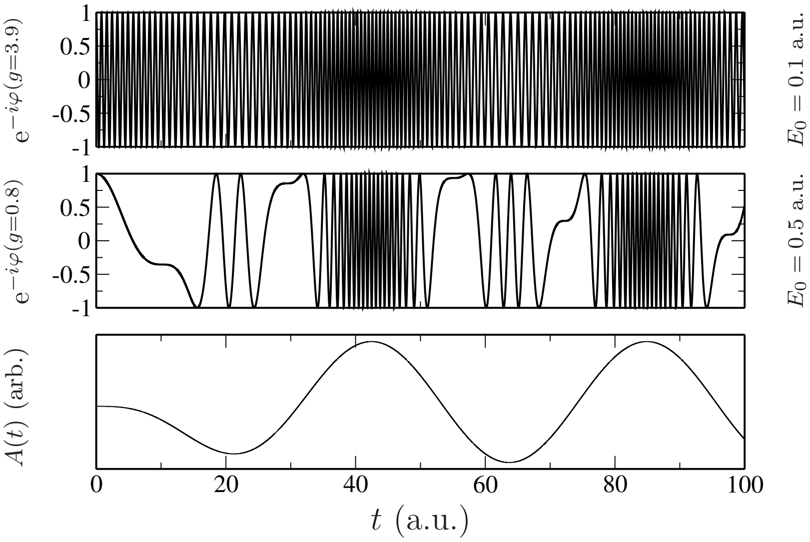

Figure 6.1: One-dimensional, time-dependent phase factors at $|\mathbf{g}| = 3.9$ a.u. (top) and $|\mathbf{g}| = 0.8$ a.u. (middle) included in the analytic solution of the TDSE using the velocity gauge Hamiltonian with electric field amplitudes of $E_0 = 0.1$ a.u. and $E_0 = 0.5$ a.u, respectively. The shape of the vector potential is presented for arbitrary units (bottom).

matrix elements, which are readily available and employed in many popular codes. Furthermore, due to the fact that the Volkov phase equals zero at $t = 0$, the initial Volkov state basis matrix elements are exactly the plane wave basis elements when describing the field-free ground state. Thus, conventional plane wave basis techniques may be used to initialize the system before propagation via the Volkov state basis.

In the Volkov state basis representation, the stiff $\frac{1}{2m}\left[\hat{\mathbf{p}} + \mathbf{A}\right]^2$ operator is removed from the acting Hamiltonian during propagation and is, instead, absorbed into the basis functions as a phase factor. Without this mathematical relocation of the vector potential, this phase factor would still be present in the time-dependence of the expansion coefficients for a static basis. The time-dependence of this phase factor is illustrated in Fig. 6.1, which is reproduced from Ref. [216] with permission of the American Physical Society. It is shown that the dynamic behavior of the expansion coefficients for a static basis set are capable of occurring on a time scale which is much shorter than the causal vector potential. The advantage of the Volkov state expansion, then, is clear as this phase factor may be analytically included in the definition of the basis functions rather than numerically propagated.

In order to apply Volkov states to the representation of periodic systems, $\mathbf{k}$-points must be introduced. By modifying the definition of the Volkov states as

$$\phi^{\mathrm{V}}_{\mathbf{k},\mathbf{g}}(\mathbf{r},t) = \frac{1}{\sqrt{\Omega}} \mathrm{e}^{i\mathbf{g}\cdot\mathbf{r}} \mathrm{e}^{-i\varphi^{\mathbf{g}+\mathbf{k}}(t)}, \tag{6.9}$$

one maintains the necessary property of Eq. (6.1) when describing a Bloch wave function of the form found in Eq. (2.59).

6.2 Computational Details and Results

In the following sections, the Volkov state basis is used within RT-TDDFT in order to simulate laser-driven dynamics in a one-dimensional periodic potential and, then, for a three-dimensional bulk diamond test case. In both scenarios, the results are compared to those of conventional representation techniques such as the related plane wave basis and the real space grid approach.

6.2.1 One-Dimensional Mathieu Potential

First, the Volkov state basis is tested for a simple one-dimensional, single-electron case using only one $\mathbf{k}$-point of $\mathbf{k} = \mathbf{0}$. The periodic potential is that of the one-dimensional Mathieu potential,

$$V(x) = -V_0 \left[1 + \cos(2\pi x/L)\right], \tag{6.10}$$

where the parameters V_0 and L are the potential amplitude set as 0.37 a.u. and the length of the unit cell set as 8 Bohr, respectively. The system is subject to a laser field as described by Eq. (5.55) with parameters $E_0 = 0.1$ a.u., $\omega = 0.148$ a.u, and $T_r = 6/\omega$. The figures and results presented here are reproduced from Ref. [211] with the permission of the American Physical Society.

A comparison of performance between the plane wave and Volkov state bases is pre-

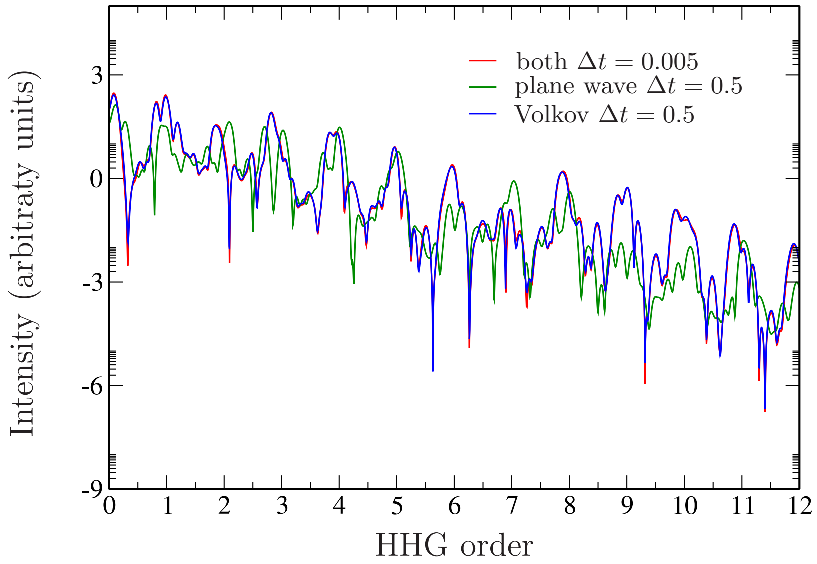

Figure 6.2: Calculations of the HHG spectra of one electron in a periodic Mathieu potential using both plane wave and Volkov state bases. This calculation was performed using a single **k**-point and propagated until $t_{\text{final}} = 500$ a.u. Laser parameters $E_0 = 0.1$ a.u. and $\omega = 0.148$ a.u. were used.

sented in Fig. 6.2 for the description of HHG. This spectrum has been obtained by taking the Fourier transform of the cell-averaged probability current after propagation of the expansion coefficients via the Crank–Nicolson time evolution operator approach. In the case of time step sizes equal to 0.005 a.u., both representations produce overlapping data, showing high harmonics at each integer multiple of the input frequency. However, for the plane wave basis, as Δt increases to 0.5 a.u. the production of these high harmonics breaks down since these large time steps are unable to resolve the rapidly changing expansion coefficients. The Volkov state basis, on the other hand, is able to nearly completely overlap with the benchmark case, even for $\Delta t = 0.5$ a.u.

The advantage of the Volkov state basis is readily noticeable in Fig. 6.3 which is reproduced from Ref [216] with the permission of the American Physical Society. This figure shows the density at the conclusion of the time step propagation. Again, both representations provide overlapping densities for the small time step size of $\Delta t = 0.005$ a.u. However, for large time step sizes, the plane wave basis yields results which diverge signif-

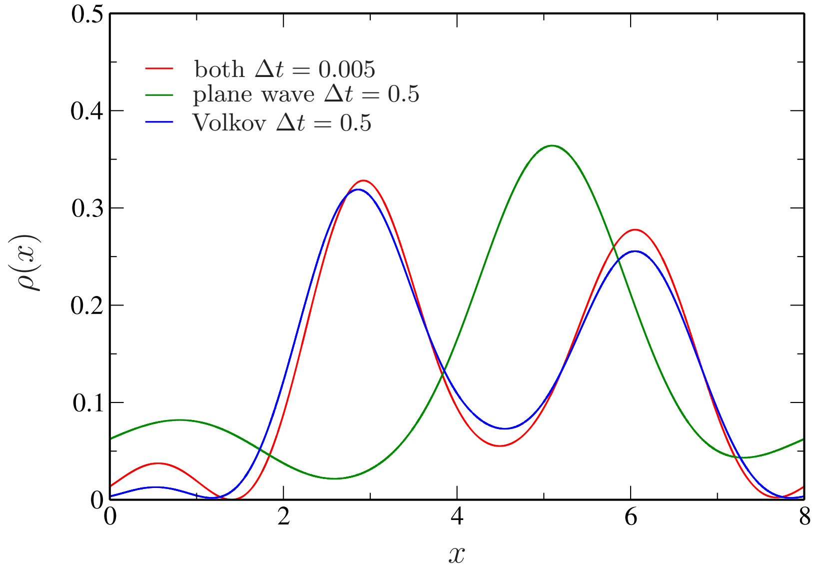

Figure 6.3: Electron density at $t_{\text{final}} = 500$ a.u. for time step sizes of $\Delta t = 0.005$ a.u. and $\Delta t = 0.5$ a.u. The potential and laser parameters were the same as those used in Fig. 6.2.

icantly from the benchmark case while the Volkov state basis yields a density which closely resembles it.

This comparison is further investigated in Figs. 6.4(a) and 6.4(b) which indicate the oscillatory nature of the expansion coefficients by plotting the metric $\langle \dot{c} \rangle = \int \langle |\text{Re}\{\dot{c}_{\mathbf{g}}\}| \rangle_t d\mathbf{g}$ for a range of field strengths and frequencies. This metric is related to the time-averaged rate of change of these coefficients over time, which is indicative of the difficulty in using the time evolution operator approach to numerically propagate the wave function. In these simulations, the potential amplitude of the Mathieu potential was set as $V_0 = 0.37$ a.u.

In this case, where the Hamiltonian is of the form $H^{\text{V}} + V$, the Volkov state expansion is expected to perform best when the frequency, and, thus, the energy, of the external field is high enough so that the perturbation of the Mathieu potential becomes negligible. This is due to the fact that, in this region, the solution approaches being analytically described by this representation. Similarly, for the plane wave representation, higher frequency fields are easier to describe as the additional complexity of including a perturbation is minimized. For both cases, higher field strengths result in more oscillatory expansion coefficients, in-

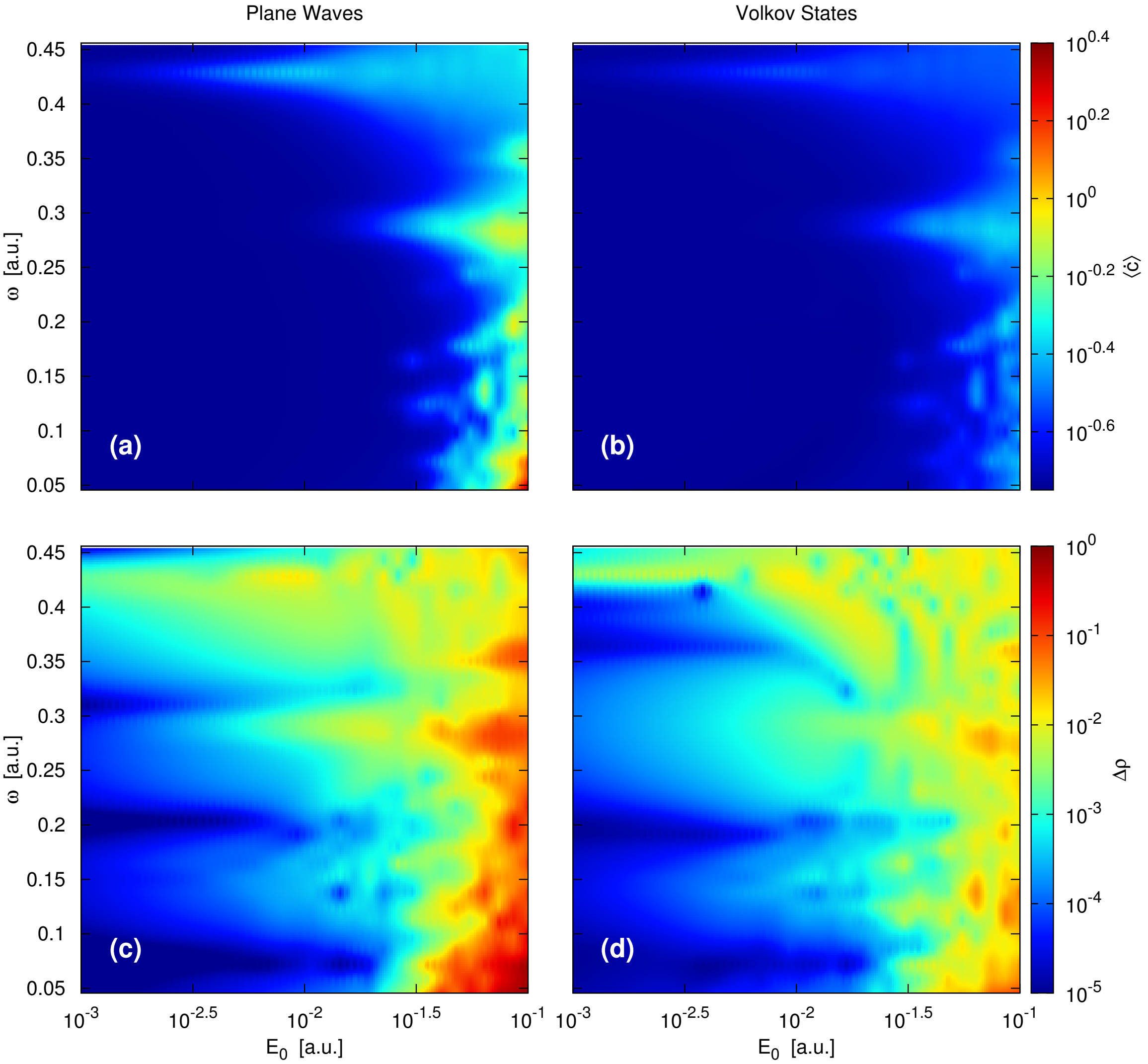

Figure 6.4: (a,b) Time-averaged, g-integrated expansion coefficients and (c,d) density difference for both plane wave and Volkov state representations over a range of laser frequencies and amplitudes. The influence of the static Mathieu potential results in resonances corresponding to the $E_0 \rightarrow E_1$ and $E_1 \rightarrow E_2$ transitions at 0.428 a.u. and 0.154 a.u., respectively, and the $E_0 \rightarrow E_2$ double photon transition at 0.291 a.u.

dicating a heightened difficulty when attempting to propagate the wave function. Most importantly, the Volkov state coefficients are seen to vary significantly more smoothly overall, which speaks to that representation's advantage.

Instead, via inductive reasoning, one may also assess the two representations by comparing the resulting final densities, $\rho(x) = |\psi(x, t_{\text{final}})|^2$, of large time step simulations to the small time step, converged solutions by the metric $\Delta\rho \equiv \int |\rho_{\text{converged}}(x) - \rho(x)| dx$.

These results are presented in Figs. 6.4(c) and 6.4(d) for the same range of field strengths and frequencies and provide a more straightforward depiction of the Volkov state expansion's ability to better represent laser-induced dynamics. The trends match those found by analyzing the average change in coefficients. It may be concluded that the advantage of the Volkov state basis is best realized for field strengths above ~ 0.3 a.u., corresponding to ~ 1.5 V/Å or, equivalently, an intensity of $\sim 3.0 \times 10^{13}$ W/cm^{12}.

6.2.2 Three-Dimensional Bulk Diamond

In this section, results, reproduced from Ref [216] with the permission of the American Physical Society, are presented for the RT-TDDFT propagation of laser excited diamond using the Volkov state basis for a laser of energy 6.05 eV. In each simulation, the vector potential was simultaneously propagated via the Verlet algorithm as explained in Ref. [85]. The external electric field representing the laser was defined using a squared sine envelope with pulse length T:

$$\mathbf{E}(t) = \mathbf{E}_0 \sin\left(\frac{\pi t}{T}\right)^2 \sin\left(\omega t\right). \tag{6.11}$$

These results are compared to benchmark calculations using the real space grid approach and a Taylor expansion of the time evolution operator, Eq. (5.13). In these simulations, the upper limit of the time step sizes used within the Taylor expansion approach was determined to be about $\Delta t = 0.005$ a.u. Above this, simulations became unstable. The Volkov state basis simulations were propagated using the split operator approach described in Ref. [211]. The resulting potential exponential was split in order to treat the nonlocal pseudopotential in the manner discussed in Ref. [195].

For each Volkov state basis calculation, the initial state was prepared using the conjugate gradient method and a plane wave basis representation, as opposed to using the real space grid approach for the ground state and Fourier transforming the result. This detail is important as the nonlinearity of the Kohn–Sham equations leads to enhanced sensitivity with respect to the choice of initial state, and by preparing the system in this manner, small perturbations attributed to the sudden change of kinetic energy operator representation at $t = 0$ were avoided.

In the example calculation, a high intensity is chosen for the laser, $I > 3 \times 10^{13}$ W/cm^2, because in this regime one expects the Volkov state basis propagation to display significant accuracy improvement as compared to full Hamiltonian discrete time step propagation methods. In the case of intense lasers applied to systems using pseudopotentials to describe frozen core electrons, the upper bound on the range of considered intensities should be around 10^{15} W/cm^2 [217]. In the following tests, the diamond unit cell is impacted by a laser pulse of intensity 1×10^{14} W/cm^2.

The Volkov state propagated energy and current, shown in Fig. 6.5, behave well for large time step sizes. The results for both 0.005 a.u. and 0.05 a.u. time step sizes nearly overlap. While the overall features of these results are well represented by the Volkov propagation, one notices the effect of nonlinear elements occurring in the Hamiltonian, namely the Hartree and exchange-correlation potentials. These terms lead to unavoidable small oscillations in the early energy. While these nonphysical features cannot be completely eliminated, they are significantly diminished by choosing a smaller time step size; see the energy inset of Fig. 6.5. These oscillations lead to growing noise in the resulting current, shown in the current inset of Fig. 6.5.

Here, the increased magnitude of the current lessens the impact of the oscillations related to the Volkov state basis propagation. Figure 6.6 shows the spectral response in which the first few harmonic resonance peaks are pronounced. Even when using a time step size of 0.05 a.u., the Volkov state basis propagation is capable of distinguishing modes related to the third and fifth harmonics. This example illustrates that for high intensities, the Volkov state basis representation is capable of accurately describing complex electron density dynamics using time step sizes roughly an order of magnitude greater than that of the conventional real space Taylor propagation method.

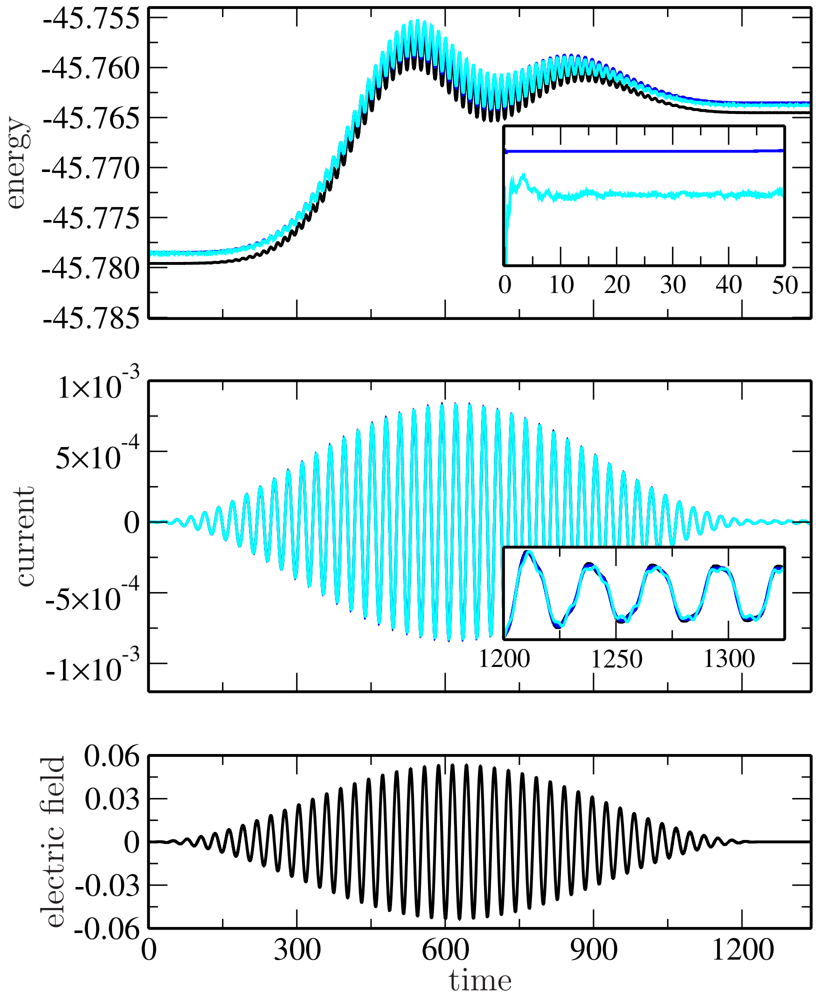

Figure 6.5: Energy and current results for real space grid and Volkov state bases corresponding to laser energy 6.05 eV, intensity 1×10^{14} W/cm^2, and width 30 fs. The real-space grid representation has been propagated using the Taylor expansion of the discrete time step propagator and a time step size of 0.005 a.u. (black). Volkov state basis results are shown for time step sizes of 0.005 a.u. (blue) and 0.05 a.u. (cyan). Insets highlight oscillation in early energies and later currents for Volkov propagations. These calculations were performed using an $8 \times 8 \times 8$ $\mathbf{k}$-point mesh. Atomic units have been employed.

6.3 Application: Nano-Scale Vacuum Tube Diode

In the following section, an example application of Volkov state basis TDDFT is presented. Many simulations are conducted which propagate an electronic density associated with 30 lithium atoms up to a final time of $t_{\text{final}} = 30$ fs. These simulations take advantage of the large time step sizes made available by the Volkov state basis. Results in this section

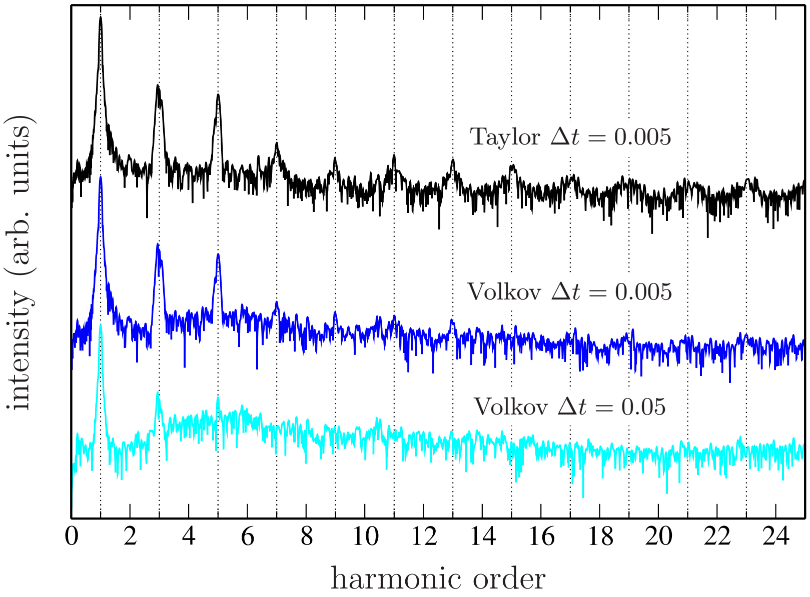

Figure 6.6: High harmonic generation results for both real space grid and Volkov state bases corresponding to the current results shown in Fig. 6.5. The employed window function is the pulse envelope.

are reproduced from Ref. [218] with the permission of AIP Publshing.

The modern era of electronics was marked by the development of the integrated circuit, whose foundation was the semiconductor-based transistor. This technology allowed for low power consumption, reliability, and intuitive circuit design, thereby outpacing and replacing the earlier relied upon vacuum-tube-based implements. Such semiconductor-based devices have been the backdrop of the advancing field of electronics for many years; however, as the push for ultrafast operating speeds approaches the petahertz range [4], the limited electron transport velocity of semiconductor transistors presents a formidable obstacle. Recent interest in electron photo-emission from metal nanotips [219–222], motivated by improved ultrafast laser-guidance of electrons [223–230], has inspired research pointing back in the direction of vacuum transport as a path towards achieving such higher speeds, with some prototype transistor devices being fabricated in the last few years [113–116].

This section focuses on the template of Higuchi *et al.*[116], who take advantage of asymmetric near-field enhancement of two facing tungsten tips in order to achieve laser-

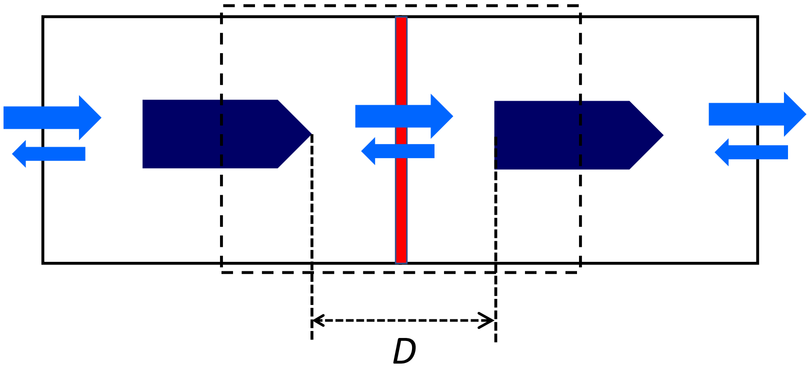

Figure 6.7: Schematic of two neighboring cells within the model system, presented as a two-dimensional slice through the middle. The jellium diode shape (dark blue) is centered within a periodic computational box of width 27 Å in directions perpendicular to the axis of symmetry. The length of the box is adjusted in order to vary the effective separation distance, D, between the sharp and flat ends of the diode shape. The sharp cone tip experiences enhanced field emission (light blue), resulting in a preferential current in the direction of sharp end to flat end (left to right in this schematic). The flux is measured at the midpoint between the two tips (red), which is essentially either the left or right boundary of the box. The dashed line box indicates the similarity of this model to that of two facing nano-scale tips.

driven rectification. It was found that by inducing electron emission from either tip using a few-cycle laser pulse, a sharper tip may act as an anode and an opposite dull tip may act as a cathode due to the relative emission rates which allow for an effective one-way total current. Because of the short duration of the multi-photon photoemission process, the high kinetic energy of the emitted electrons, and the sub-micron separation distance between the opposing tips, it was asserted that this device was able to operate on the sub-picosecond timescale. Furthermore, it was noted that faster electron transport may be possible for smaller separation distances due to stronger field enhancement and, in the sub-nanometer separation regime, prominent tunneling channels [101].

6.3.1 Model

This investigation of laser-driven nano-scale rectification was pursued by means of simulation via RT-TDDFT applied to a jellium model of a lithium cluster. Such models have been shown to well-resemble the description of electronic excitations in bulk metal counterparts [107, 133, 231–233]. In this case, the external ion potential was represented by the Coulomb attraction to the homogeneous positive background charge density of the jellium,

$$V^{\text{ion}}(\mathbf{r}) = \frac{-e^2}{4\pi\epsilon_0} \int \frac{\rho_{\text{bg}}(\mathbf{r}')}{|\mathbf{r} - \mathbf{r}'|} d\mathbf{r}'. \tag{6.12}$$

The shape of the positive background charge density was chosen to be a cylinder with one end capped by a cone—see Fig. 6.7—in order to model facing sharp and flat tips. The system was excited by a homogeneous laser field in order to simulate an induced preferential net current direction. Periodic boundary conditions were enforced so that electron density leaving from either end of the jellium model traveled between the two sites by wrapping through the boundary of the computational box, a process analogous to the facing tips of Higuchi *et al.*. The system of study in this work, then, is truly an infinitely repeating chain of pointed jellium diode devices. Only one $\mathbf{k}$-point was employed in these calculations, with value of $\mathbf{k} = 0$.

In these simulations, the sharp tip of the jellium is expected to induce field enhancement [234, 235] which, in turn, is expected to result in amplified electron emission at that site. The directionally favored electron emission is expected to lead to a preferential net current direction traveling in the direction of sharp tip to flat tip. The cylindrical portion of the jellium was given a radius of 3.43 Å, with the angle of the cone-shape cap as $80°$. The total length of the shape was then 20 Å, in order to yield a volume corresponding to a cluster of 30 lithium atoms. The length of the box was adjusted in order to vary the separation distance between the tips.

6.3.2 Results and Discussion

The jellium model system was subjected to a laser of wavelength 780 nm, polarized parallel to the axis of symmetry, which induced an oscillating current in the computational

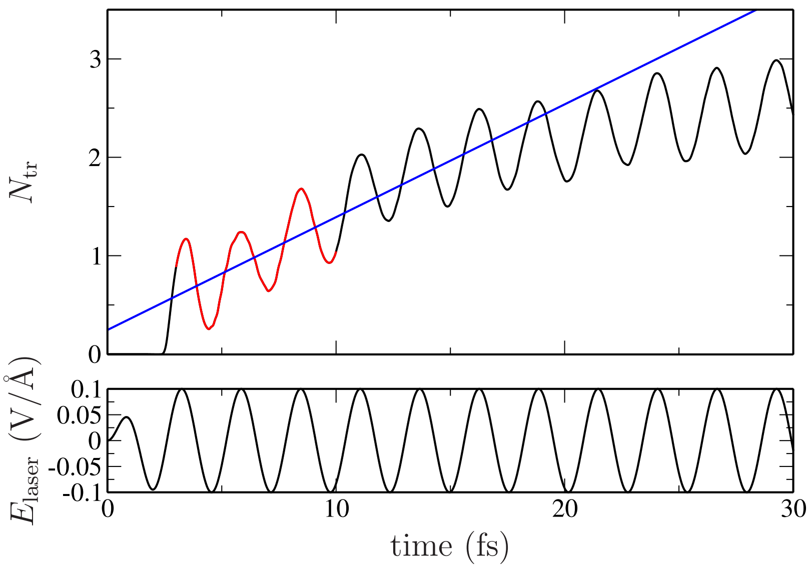

Figure 6.8: Probability density transfered through the plane bisecting the two jellium model edges (top) for the example case of $D = 30$ Å, using a laser field of $I = 1.33 \times 10^{13}$ W/cm^2 and $T_{\rm r} = 2.48$ fs (bottom). A linear fit (blue) was fit by linear regression applied to the data sampled between $t = 3$ and $t = 10$ fs (red).

box. The resulting flux, determined at the location of the plane bisecting the two edges of the jellium model, z_0, as

$$\Phi(z_0, t) = \frac{\hbar}{mi} \int \int \mathbf{j}(x, y, z_0; t) dx dy, \tag{6.13}$$

was integrated over time in order to ascertain the probability density transfered, $N_{\rm tr}$:

$$N_{\rm tr}(t) = \int_0^t \Phi(t') dt'. \tag{6.14}$$

Figure 6.8 shows this result for an example scenario of a separation distance, D, of 30 Å, a field intensity, I, of 1.33×10^{13} W/cm^2, and a short field ramping time of $T_{\rm r} = 2.48$ fs. Here, positive values for $N_{\rm tr}$ relate to a transfer of probability density from sharp to flat edges of the jellium model, i.e. left to right with respect to the schematic in Fig. 6.7. In each simulation, the small time regime ($t \leq 15$ fs) was well described by a linear trending sine curve. This section was fit by means of linear regression and the probability

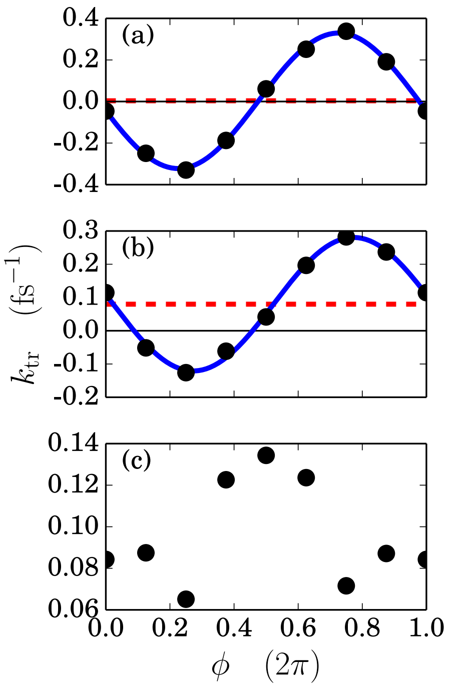

Figure 6.9: Phase dependence of the probability density transfer rate for (a) a symmetric jellium cylinder shape without a cone cap and with a ramping time of $T_{\mathrm{r}} = 2.48$ fs, (b) the diode jellium model with a ramping time of $T_{\mathrm{r}} = 2.48$ fs, and (c) the diode jellium model with a ramping time of $T_{\mathrm{r}} = 9.94$ fs. For results using the shorter ramping time, a sinusoidal fit (blue line) shifted by an offset along the y-axis (dashed red line) was determined via linear regression. Each simulation employed parameters $D = 30$ Å and $I = 1.33 \times 10^{13}$ W/cm^2.

density transfer rate, k_{tr}, was determined as the slope of the resulting trend line. The rate of transfer tended to level off soon after this region in each simulation. This is most likely due to the increasing amount of high-energy orbitals being ionized from the jellium and following the field as nearly free particles. In this way, the near-field enhancement becomes more negligible to the physics described within the computational box as the simulation progresses.

The laser phase dependence of the transfer rate is shown in Fig. 6.9 for parameters $D = 30$ Å and $I = 1.33 \times 10^{13}$ W/cm^2. A symmetrically shaped cylinder without a cone cap was substituted in Fig. 6.9(a) in order to serve as a control test under geometrically symmetric conditions. In this case, while the shape of the jellium is symmetric, the phase,

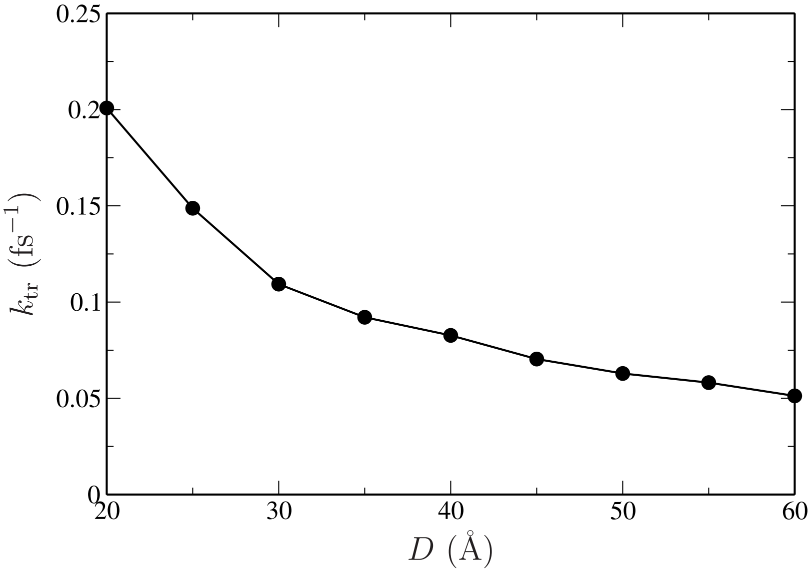

Figure 6.10: Separation distance dependence of the probability density transfer rate for the jellium diode shape using a ramping time of $T_\mathrm{r} = 9.94$ fs and an intensity of $I = 1.33\times10^{13}$ W/cm^2. Data points have been connected with a solid line in order to guide the eye.

in combination with the short ramp time, provides a source of asymmetry by significantly lowering the effective potential barrier on one end of the jellium before the other. This causes a preferred current direction in the early time steps of the simulation. The trend observed is well described as a sine curve, whose vertical shift only varies from the zero axis by 0.004 fs^{-1} (1 % of the amplitude). This insignificant offset indicates that no particular direction along the axis of symmetry is favored when the influence of the phase is neglected. However, for the case of the diode shape, Fig. 6.9(b), the same trend may be applied with an offset of 0.080 fs^{-1} (40 % of the amplitude), indicating a preferential current in the direction of sharp to flat edges. A longer ramping time of $T_\mathrm{r} = 9.94$ fs was also employed using the diode shape, Fig. 6.9(c), in order to demonstrate positive transfer rates for any choice of phase. In this case, no such discernible trend was determined.

The dependence of the transfer rate on the separation distance, D, is presented in Fig. 6.10. For each value of D, two simulations were performed using a phase of either 0 or π. The two results for k_tr were then averaged together in order to eliminate the phase dependence. Even for the smallest separation distance of 20 Å, the potential barrier is wide enough as to not allow for significant tunneling. The enhanced net transfer rate for shorter separation distances is due to the faster arrival of the emitted electron density to the opposite edge of the jellium. This traveling density, then, interacts with the Kohn-Sham effective potential well and, thus, is reintroduced to the near-field enhancement.

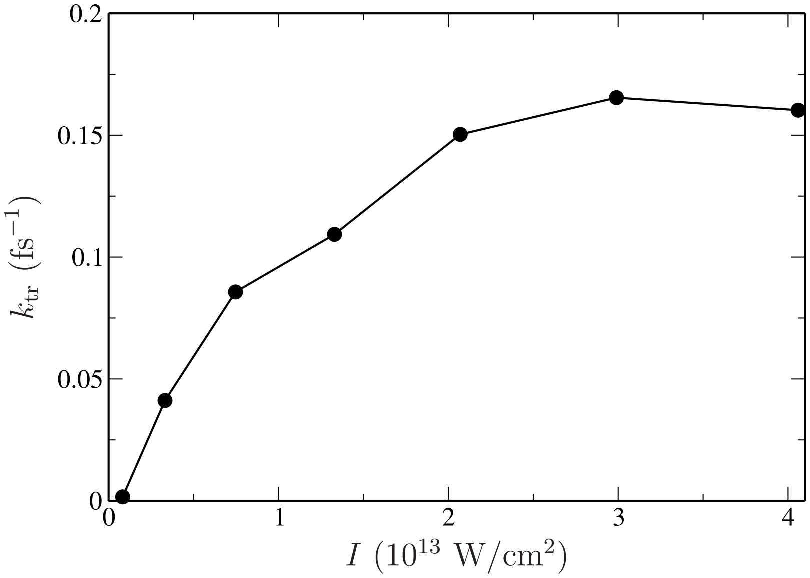

Figure 6.11: Intensity dependence of the probability density transfer rate for the jellium diode shape using a ramping time of $T_{\mathrm{r}} = 9.94$ fs and a separation distance of $D = 30$ Å. Data points have been connected with a solid line in order to guide the eye.

Figure 6.11 shows the dependence of the transfer rate on the intensity of the laser field. These simulations were similarly performed twice each in order to average results for laser phases of 0 and π. As the intensity rises, so too does the transfer rate. However, at large enough intensities, as in this case of around $I = 3 \times 10^{13}$ W/cm^2, the emission from either edge begins to become comparable and the trend in the net transfer rate, k_{tr}, levels off.

6.4 Summary

In summary, the Volkov state basis was implemented and tested for representing periodic structures in both one- and three-dimensional cases against the plane wave basis and real-space grid representations, respectively. In either scenario, the Volkov state basis propagation was capable of besting the conventional methods by allowing an increase in time step size by an order of magnitude when describing interactions with fields of intensity greater than 3×10^{13} W/cm^2. For the case of representing bulk diamond, the Volkov state basis propagation successfully produced current oscillation modes related to the third and fifth harmonics, even at large time step sizes. This approach may be easily implemented within existing plane wave codes by the straightforward calculation of the time-dependent Volkov phase factors. As popular RT-TDDFT codes currently employ static basis functions borrowed from DFT implementations, the success of the Volkov state basis may be viewed as motivation for the further investigation of other potential choices of time-dependent basis functions, explicitly chosen for RT-TDDFT. While the periodic nature of the Volkov states allows for optimal application to the study periodic systems, this basis may just as easily be employed for the describing non-periodic cases [216].

Furthermore, laser-induced rectification has been computationally demonstrated by simulating the effects of increased electron emission due to near-field enhancement within a periodic jellium system with geometrical asymmetry. Such behavior opens the door for new nano-scale "vacuum-tube-based" devices, which take advantage of the enhanced transport rate of electrons in vacuum as compared to the relatively limited electron transport rates in conventional semiconductor-based devices. These findings show a significant increase in transport rate when the distance between facing anode and cathode tips becomes small. Similarly, an increase in transport rate has been shown for higher laser intensities; however, for high enough laser intensities, the local near-field enhancement becomes negligible and rectification becomes less prominent.

Chapter 7

CONCLUSION

In this thesis, bottlenecks on the computational implementation of real-time time-dependent density functional theory have been addressed. Various improvements which allow for improved accuracy or computational efficiency have been demonstrated. It is the goal of this thesis to present and promote such computational methods so that time-dependent density functional calculations may become further accessible and capable of describing a wider range of electronic systems and attosecond-scale phenomenon.

In Chapter 2, density functional theory and time-dependent density functional theory were reviewed as the predominant tool for describing non-relativistic many-electron electronic structure and dynamics, respectively, motivated by the difficulty in solving the many-electron Schrödinger equation directly. The inclusion of external electromagnetic fields in time-dependent density functional theory was discussed as a means of describing laser-matter interactions. In order to represent core electrons in a computationally efficient manner, the pseudopotential approach was presented which replaces the interaction between the valence electrons and ions—that is, core electrons and nuclei—with numerically constructed effective potentials, consisting of local and nonlocal contributions. Finally, the Bloch theory of solids was introduced which describes the electron wave function for spatially periodic Hamiltonians.

In Chapter 3, conventional means of discretizing the real space description of the wave functions were presented, along with implications for the application of density functional theory. Such techniques are necessary in order to allow for the representation of continuous functions within the discrete language of computer codes. Three popular approaches were discussed: the atomic orbitals basis, the plane wave basis, and the real space grid approach. Each of these are widely used today in density functional theory calculations.

In Chapter 4, another means of representation, the pseudospectral basis, was presented. This choice is related to the real space grid approach in its simplicity of implementation but allows for significantly improved accuracy due to the use of continuous basis functions. On the other hand, in its basic form, the pseudospectral basis demands kinetic energy matrices which are significantly less sparse than in the real space grid approach, thus dramatically lowering the computational efficiency. It was shown, however, that by employing acceleration weights to the description of these matrices, one could match the computational efficiency of the real space approach while maintaining the improved accuracy. It is believed that this basis may allow for significantly improved accuracy in not only ground state calculations, as shown in this chapter, but also in time-dependent simulations.

In Chapter 5, a collection of propagation techniques were presented which solve the time-dependent Schrödinger equation for a wave function at some time of interest. First, popular techniques for direct integration of the time-dependent Schrödinger equation were introduced. Second, techniques making use of the time evolution operator form were introduced, which propagate the wave function by small discrete time steps using a unitary operator which depends on the full time-dependent Hamiltonian. Finally, a new class of propagation techniques were introduced which are of particular interest for the solution of the time-dependent Kohn–Sham equations of time-dependent density functional theory due to their specialty for handling differential equations with nonlinear terms. These were the integrating factor and exponential time differencing methods, collectively known as exponential integrator methods.

A variety of techniques derived from these methods were tested against the conventional choices for the following one-dimensional test cases of a helium atom: initialized in an excited state without external perturbation and initialized in the ground state and excited with a laser field. Throughout these tests, the fourth-order Runge–Kutta variants of the exponential integrator methods either matched or bested the conventional propagation techniques. Similarly, the second-order Runge–Kutta variants and other exponential integrator methods of lower time step scaling accuracy exhibited enhanced performance, given the cheaper computational cost. Beyond the success of the Runge–Kutta-type exponential integrator propagation techniques used here, they might further benefit from the ability of the Runge–Kutta method to propagate the wave function using variable time step sizes. This implies the capability od dynamically adjusting the time step size throughout a simulation in order to optimally balance computational cost and accuracy. While the time step size has been kept constant in this research, such an improvement is suggested as the subject of future work.

Chapter 6 presented a new set of basis functions related to plane waves, the time-dependent Volkov states, which well-resemble motion driven by external fields. The Volkov state basis was shown to allow for significantly larger time step sizes when simulating the effects of high intensity lasers, allowing for faster computational times, or, alternatively, higher accuracy when using conventional time step sizes. The necessary matrix elements were shown to be easily accessible, being those of the plane wave basis multiplied by an analytically available phase factor. While the Volkov state basis approach shares the same purpose as the exponential integrator methods, that is, both are meant to improve the accuracy of time-dependent simulations, each are best applied for particular applications. The Volkov state basis is perfectly suited for periodic calculations, and the exponential integrator methods well-describe dynamics driven by nonlinear effects. Furthermore, the two may be combined, as the latter are independent of the basis representation. This combination may provide a means of alleviating the nonphysical oscillations occurring in the large time step Volkov state basis simulations which are due to the nonlinear potential functionals.

An example application taking advantage of the fast computational times of the Volkov state basis was then presented in which a new device design, effectively consisting of a nano-scale vacuum-tube diode, was investigated computationally. In this study, a clear rectification effect resulting from geometrical asymmetry was demonstrated, and the dependence of the electron transfer rate between cathode and anode on the separation distance and laser intensity were qualitatively described. As many simulations were required for the collection of this data, the study benefited significantly from computational speeds about ten times faster than those available using conventional representation techniques.

As laser technologies continue to advance, driving the further sophistication of experimental techniques, such computational improvements as those introduced in this thesis are undoubtedly to be proven invaluable towards the effort of theoretically investigating attosecond scale phenomenon. Such simultaneous improvement is expected to lead towards the ability to control electronic process on their natural time scale.

BIBLIOGRAPHY

[1] S. Baker, I. A. Walmsley, J. W. G. Tisch, and J. P. Marangos. Femtosecond to attosecond light pulses from a molecular modulator. *Nat. Photonics*, 2011.

[2] T. Popmintchev, M.-C. Chen, P. Arpin, M. M. Murnane, and H. C. Kapteyn. The attosecond nonlinear optics of bright coherent x-ray generation. *Nat. Photonics*, 2010.

[3] B. Bergues, D. E. Rivas, M. Weidman, A. A. Muschet, W. Helml, A. Guggenmos, V. Pervak, U. Kleineberg, G. Marcus, R. Kienberger, D. Charalambidis, P. Tzallas, H. Schröder, F. Krausz, and L. Veisz. Tabletop nonlinear optics in the 100-ev spectral region. *Opt.*, 2018.

[4] M. F. Ciappina, J. A. Pérez-Hernández, A. S. Landsman, W. A. Okell, S. Zherebtsov, B. Förg, J. Schötz, L. Seiffert, T. Fennel, T. Shaaran, T. Zimmermann, A. Chacn, R. Guichard, A. Zaïr, J. W. G. Tisch, J. P. Marangos, T. Witting, A. Braun, S. A. Maier, L. Roso, M. Krüger, P. Hommelhoff, M. F. Kling, F. Krausz, and M. Lewenstein. Attosecond physics at the nanoscale. *Reports on Prog. Phys.*, 2017.

[5] A. Becker, F. He, A. Picón, C. Ruiz, N. Takemoto, and A. Jaroń-Becker. *Observation and Control of Electron Dynamics in Molecules*, pages 207–229. Springer Berlin Heidelberg, 2013.

[6] P. B. Corkum and F. Krausz. Attosecond science. *Nat Phys*, 2007.

[7] F. Krausz and M. I. Stockman. Attosecond metrology: from electron capture to future signal processing. *Nat. Photonics*, 2014.

[8] J. Mauritsson, T. Remetter, M. Swoboda, K. Klünder, A. L'Huillier, K. J. Schafer, O. Ghafur, F. Kelkensberg, W. Siu, P. Johnsson, M. J. J. Vrakking, I. Znakovskaya,

T. Uphues, S. Zherebtsov, M. F. Kling, F. Lépine, E. Benedetti, F. Ferrari, G. Sansone, and M. Nisoli. Attosecond electron spectroscopy using a novel interferometric pump-probe technique. *Phys. Rev. Lett.*, 2010.

[9] Z. Vager, R. Naaman, and E. P. Kanter. Coulomb explosion imaging of small molecules. *Sci.*, 1989.

[10] S. X. Hu and L. A. Collins. Attosecond pump probe: Exploring ultrafast electron motion inside an atom. *Phys. Rev. Lett.*, 2006.

[11] T. Remetter, P. Johnsson, J. Mauritsson, K. Varju, Y. Ni, F. Lepine, E. Gustafsson, M. Kling, J. Khan, R. Lopez-Martens, K. J. Schafer, M. J. J. Vrakking, and A. L'Huillier. Attosecond electron wave packet interferometry. *Nat Phys*, 2006.

[12] R. Kienberger, M. Hentschel, M. Uiberacker, C. Spielmann, M. Kitzler, A. Scrinzi, M. Wieland, T. Westerwalbesloh, U. Kleineberg, U. Heinzmann, M. Drescher, and F. Krausz. Steering attosecond electron wave packets with light. *Sci.*, 2002.

[13] S. T. Kim, P. F. Heelis, T. Okamura, Y. Hirata, N. Mataga, and A. Sancar. Determination of rates and yields of interchromophore (folate .fwdarw. flavin) energy transfer and intermolecular (flavin .fwdarw. dna) electron transfer in escherichia coli photolyase by time-resolved fluorescence and absorption spectroscopy. *Biochem.*, 1991.

[14] H. Ikeura-Sekiguchi and T. Sekiguchi. Attosecond electron delocalization in the conduction band through the phosphate backbone of genomic dna. *Phys. Rev. Lett.*, 2007.

[15] B. Krauss, T. Lohmann, D.-H. Chae, M. Haluska, K. von Klitzing, and J. H. Smet. Laser-induced disassembly of a graphene single crystal into a nanocrystalline network. *Phys. Rev. B*, 2009.

[16] S. Haessler, J. Caillat, W. Boutu, C. Giovanetti-Teixeira, T. Ruchon, T. Auguste, Z. Diveki, P. Breger, A. Maquet, B. Carre, R. Taieb, and P. Salieres. Attosecond imaging of molecular electronic wavepackets. *Nat Phys*, 2010.

[17] A. Assion, T. Baumert, M. Bergt, T. Brixner, B. Kiefer, V. Seyfried, M. Strehle, and G. Gerber. Control of chemical reactions by feedback-optimized phase-shaped femtosecond laser pulses. *Sci.*, 1998.

[18] S. A. Wolf, D. D. Awschalom, R. A. Buhrman, J. M. Daughton, S. von Molnr, M. L. Roukes, A. Y. Chtchelkanova, and D. M. Treger. Spintronics: A spin-based electronics vision for the future. *Sci.*, 2001.

[19] P. Kok, W. J. Munro, K. Nemoto, T. C. Ralph, J. P. Dowling, and G. J. Milburn. Linear optical quantum computing with photonic qubits. *Rev. Mod. Phys.*, 2007.

[20] E. Schrödinger. An undulatory theory of the mechanics of atoms and molecules. *Phys. Rev.*, 1926.

[21] L. H. Thomas. The calculation of atomic fields. *Math. Proc. Camb. Philos. Soc.*, 1927.

[22] E. Fermi. Un metodo statistico per la determinazione di alcune priopriet dellatomo (a statistical method for the determination of some atomic properties). *Rend. Accad. Naz. Lincei*, 1927.

[23] D. R. Hartree. The wave mechanics of an atom with a non-coulomb central field. part i. theory and methods. *Math. Proc. Camb. Philos. Soc.*, 1928.

[24] J. C. Slater. The theory of complex spectra. *Phys. Rev.*, 1929.

[25] V. Fock. Näherungsmethode zur Lösung des quantenmechanischen Mehrkörperproblems (approach for solving quantum mechanical multibody problems). *Zeitschrift fur Physik*, 1930.

[26] J. C. Slater. Note on hartree's method. *Phys. Rev.*, 1930.

[27] F. Bloch. Über die quantenmechanik der elektronen in kristallgittern (on the quantum mechanics of electrons in crystal lattices). *Zeitschrift für Physik*, 1929.

[28] E. Wigner and F. Seitz. On the constitution of metallic sodium. *Phys. Rev.*, 1933.

[29] E. Wigner and F. Seitz. On the constitution of metallic sodium. ii. *Phys. Rev.*, 1934.

[30] H. Hellmann. A new approximation method in the problem of many electrons. *The J. Chem. Phys.*, 1935.

[31] P. A. M. Dirac. Note on exchange phenomena in the thomas atom. *Math. Proc. Camb. Philos. Soc.*, 1930.

[32] P. Hohenberg and W. Kohn. Inhomogeneous electron gas. *Phys. Rev.*, 1964.

[33] W. Kohn and L. J. Sham. Self-consistent equations including exchange and correlation effects. *Phys. Rev.*, 1965.

[34] K. Burke. Perspective on density functional theory. *The J. Chem. Phys.*, 2012.

[35] D. J. Tozer and M. J. G. Peach. Density functional theory and its applications. *Phys. Chem. Chem. Phys.*, 2014.

[36] B. Kirste. Applications of density functional theory to theoretical organic chemistry. *Chem Sci J*, 2016.

[37] J. P. Brodholt and L. Voadlo. Applications of density functional theory in the geosciences. *MRS Bull.*, 2006.

[38] D. J. Cole and N. D. M. Hine. Applications of large-scale density functional theory in biology. *J. Physics: Condens. Matter*, 2016.

[39] F. Giustino. *Materials Modelling Using Density Functional Theory: Properties and Predictions*. 2014.

[40] W. Kohn. Nobel lecture: Electronic structure of matter-wave functions and density functionals. *Rev. Mod. Phys.*, 1999.

[41] E. Runge and E. K. U. Gross. Density-functional theory for time-dependent systems. *Phys. Rev. Lett.*, 1984.

[42] R. E. Stratmann, G. E. Scuseria, and M. J. Frisch. An efficient implementation of time-dependent density-functional theory for the calculation of excitation energies of large molecules. *The J. Chem. Phys.*, 1998.

[43] R. Bauernschmitt and R. Ahlrichs. Treatment of electronic excitations within the adiabatic approximation of time dependent density functional theory. *Chem. Phys. Lett.*, 1996.

[44] M. van Faassen and K. Burke. Time-dependent density functional theory of high excitations: to infinity, and beyond. *Phys. Chem. Chem. Phys.*, 2009.

[45] G. Onida, L. Reining, and A. Rubio. Electronic excitations: density-functional versus many-body green's-function approaches. *Rev. Mod. Phys.*, 2002.

[46] J. R. Chelikowsky, L. Kronik, and I. Vasiliev. Time-dependent density-functional calculations for the optical spectra of molecules, clusters, and nanocrystals. *J. Physics: Condens. Matter*, 2003.

[47] M. E. Casida. Time-dependent density-functional theory for molecules and molecular solids. *J. Mol. Struct. THEOCHEM*, 2009.

[48] R. W. Boyd. *Nonlinear optics*. 2003.

[49] J.-C. Diels and W. Rudolph. *Ultrashort laser pulse phenomena: fundamentals, techniques, and applications on a femtosecond time scale*. 2006.

[50] A. H. Zewail. Femtochemistry: atomic-scale dynamics of the chemical bond. *The J. Phys. Chem. A*, 2000.

[51] R. Szipöcs, C. Spielmann, F. Krausz, and K. Ferencz. Chirped multilayer coatings for broadband dispersion control in femtosecond lasers. *Opt. letters*, 1994.

[52] P. Agostini, F. Fabre, G. Mainfray, G. Petite, and N. K. Rahman. Free-free transitions following six-photon ionization of xenon atoms. *Phys. Rev. Lett.*, 1979.

[53] J. J. Macklin, J. D. Kmetec, and C. L. Gordon. High-order harmonic generation using intense femtosecond pulses. *Phys. Rev. Lett.*, 1993.

[54] A. L'Huillier and P. Balcou. High-order harmonic generation in rare gases with a 1-ps 1053-nm laser. *Phys. Rev. Lett.*, 1993.

[55] R. Kienberger, E. Goulielmakis, M. Uiberacker, A. Baltuska, V. Yakovlev, F. Bammer, A. Scrinzi, T. Westerwalbesloh, U. Kleineberg, U. Heinzmann, M. Drescher, and F. Krausz. Atomic transient recorder. *Nat.*, 2004.

[56] M. Hentschel, R. Kienberger, C. Spielmann, G. A. Reider, N. Milosevic, T. Brabec, P. Corkum, U. Heinzmann, M. Drescher, and F. Krausz. Attosecond metrology. *Nat.*, 2001.

[57] P. Agostini and L. F. DiMauro. The physics of attosecond light pulses. *Reports on progress physics*, 2004.

[58] F. Krausz and M. Ivanov. Attosecond physics. *Rev. Mod. Phys.*, 2009.

[59] A. Baltuška, T. Udem, M. Uiberacker, M. Hentschel, E. Goulielmakis, C. Gohle, R. Holzwarth, V. Yakovlev, A. Scrinzi, T. W. Hänsch, et al. Attosecond control of electronic processes by intense light fields. *Nat.*, 2003.

[60] W. Hanke and L. J. Sham. Local-field and excitonic effects in the optical spectrum of a covalent crystal. *Phys. Rev. B*, 1975.

[61] W. Hanke and L. J. Sham. Many-particle effects in the optical spectrum of a semiconductor. *Phys. Rev. B*, 1980.

[62] M. S. Hybertsen and S. G. Louie. First-principles theory of quasiparticles: Calculation of band gaps in semiconductors and insulators. *Phys. Rev. Lett.*, 1985.

[63] R. W. Godby, M. Schlüter, and L. J. Sham. Self-energy operators and exchange-correlation potentials in semiconductors. *Phys. Rev. B*, 1988.

[64] M. Rohlfing, P. Krüger, and J. Pollmann. Quasiparticle band structure of cds. *Phys. Rev. Lett.*, 1995.

[65] M. Lucchini, S. A. Sato, A. Ludwig, J. Herrmann, M. Volkov, L. Kasmi, Y. Shinohara, K. Yabana, L. Gallmann, and U. Keller. Attosecond dynamical franz-keldysh effect in polycrystalline diamond. *Sci.*, 2016.

[66] D. Jacquemin, E. A. Perpte, I. Ciofini, and C. Adamo. Accurate simulation of optical properties in dyes. *Accounts Chem. Res.*, 2009.

[67] H. E. Johnson and C. M. Aikens. Electronic structure and tddft optical absorption spectra of silver nanorods. *The J. Phys. Chem. A*, 2009.

[68] C. Adamo and D. Jacquemin. The calculations of excited-state properties with time-dependent density functional theory. *Chem. Soc. Rev.*, 2013.

[69] M. Cascella, M. A. Cuendet, I. Tavernelli, and U. Rothlisberger. Optical spectra of cu(ii)—azurin by hybrid tddft-molecular dynamics simulations. *The J. Phys. Chem. B*, 2007.

[70] A. Marini, R. Del Sole, and A. Rubio. Bound excitons in time-dependent density-functional theory: Optical and energy-loss spectra. *Phys. Rev. Lett.*, 2003.

[71] N. H. Burnett, H. A. Baldis, M. C. Richardson, and G. D. Enright. Harmonic generation in co2 laser target interaction. *Appl. Phys. Lett.*, 1977.

[72] R. L. Carman, C. K. Rhodes, and R. F. Benjamin. Observation of harmonics in the visible and ultraviolet created in CO_2-laser-produced plasmas. *Phys. Rev. A*, 1981.

[73] A. McPherson, G. Gibson, H. Jara, U. Johann, T. S. Luk, I. A. McIntyre, K. Boyer, and C. K. Rhodes. Studies of multiphoton production of vacuum-ultraviolet radiation in the rare gases. *J. Opt. Soc. Am. B*, 1987.

[74] P. B. Corkum. Plasma perspective on strong field multiphoton ionization. *Phys. Rev. Lett.*, 1993.

[75] S. Chelkowski, T. Bredtmann, and A. D. Bandrauk. High-order-harmonic generation from coherent electron wave packets in atoms and molecules as a tool for monitoring attosecond electrons. *Phys. Rev. A*, 2012.

[76] P. M. Kraus, S. B. Zhang, A. Gijsbertsen, R. R. Lucchese, N. Rohringer, and H. J. Wörner. High-harmonic probing of electronic coherence in dynamically aligned molecules. *Phys. Rev. Lett.*, 2013.

[77] H. J. Wörner, J. B. Bertrand, D. V. Kartashov, P. B. Corkum, and D. M. Villeneuve. Following a chemical reaction using high-harmonic interferometry. *Nat.*, 2010.

[78] J. Chen, Y. Yang, J. Chen, and B. Wang. Probing dynamic information and spatial structure of rydberg wave packets by harmonic spectra in a few-cycle laser pulse. *Phys. Rev. A*, 2015.

[79] T. Higuchi, M. I. Stockman, and P. Hommelhoff. Strong-field perspective on high-harmonic radiation from bulk solids. *Phys. Rev. Lett.*, 2014.

[80] T. Tamaya, A. Ishikawa, T. Ogawa, and K. Tanaka. Diabatic mechanisms of higher-order harmonic generation in solid-state materials under high-intensity electric fields. *Phys. Rev. Lett.*, 2016.

[81] N. Tancogne-Dejean, O. D. Mücke, F. X. Kärtner, and A. Rubio. Ellipticity dependence of high-harmonic generation in solids originating from coupled intraband and interband dynamics. *Nat. Commun.*, 2017.

[82] Y. S. You, Y. Yin, Y. Wu, A. Chew, X. Ren, F. Zhuang, S. Gholam-Mirzaei, M. Chini, Z. Chang, and S. Ghimire. High-harmonic generation in amorphous solids. *Nat. Commun.*, 2017.

[83] N. Tancogne-Dejean, O. D. Mücke, F. X. Kärtner, and A. Rubio. Impact of the electronic band structure in high-harmonic generation spectra of solids. *Phys. Rev. Lett.*, 2017.

[84] T. Otobe. High-harmonic generation in α-quartz by electron-hole recombination. *Phys. Rev. B*, 2016.

[85] Y. Li, S. He, A. Russakoff, and K. Varga. Accurate time propagation method for the coupled maxwell and kohn-sham equations. *Phys. Rev. E*, 2016.

[86] A. Boltasseva and H. A. Atwater. Low-loss plasmonic metamaterials. *Sci.*, 2011.

[87] P. J. Schuck, D. P. Fromm, A. Sundaramurthy, G. S. Kino, and W. E. Moerner. Improving the mismatch between light and nanoscale objects with gold bowtie nanoantennas. *Phys. Rev. Lett.*, 2005.

[88] A. G. Curto, G. Volpe, T. H. Taminiau, M. P. Kreuzer, R. Quidant, and N. F. van Hulst. Unidirectional emission of a quantum dot coupled to a nanoantenna. *Sci.*, 2010.

[89] A. N. Grigorenko, M. Polini, and K. S. Novoselov. Graphene plasmonics. *Nat. Photonics*, 2012.

[90] J. N. Anker, W. P. Hall, O. Lyandres, N. C. Shah, J. Zhao, and R. P. Van Duyne. Biosensing with plasmonic nanosensors. *Nat. Mater.*, 2008.

[91] A. G. Brolo. Plasmonics for future biosensors. *Nat. Photonics*, 2012.

[92] H. Xu, E. J. Bjerneld, M. Käll, and L. Börjesson. Spectroscopy of single hemoglobin molecules by surface enhanced raman scattering. *Phys. Rev. Lett.*, 1999.

[93] D.-K. Lim, K.-S. Jeon, H. M. Kim, J.-M. Nam, and Y. D. Suh. Nanogap-engineerable raman-active nanodumbbells for single-molecule detection. *Nat. Mater.*, 2009.

[94] P. Berini and I. De Leon. Surface plasmon-polariton amplifiers and lasers. *Nat. Photonics*, 2011.

[95] H. A. Atwater and A. Polman. Plasmonics for improved photovoltaic devices. *Nat. Mater.*, 2010.

[96] A. Polman and H. A. Atwater. Photonic design principles for ultrahigh-efficiency photovoltaics. *Nat. Mater.*, 2012.

[97] D. L. Jeanmaire and R. P. V. Duyne. Surface raman spectroelectrochemistry: Part i. heterocyclic, aromatic, and aliphatic amines adsorbed on the anodized silver electrode. *J. Electroanal. Chem. Interfacial Electrochem.*, 1977.

[98] S. Nie and S. R. Emory. Probing single molecules and single nanoparticles by surface-enhanced raman scattering. *Sci.*, 1997.

[99] A. Aubry, D. Y. Lei, A. I. Fernndez-Domnguez, Y. Sonnefraud, S. A. Maier, and J. B. Pendry. Plasmonic light-harvesting devices over the whole visible spectrum. *Nano Lett.*, 2010.

[100] J. A. Schuller, E. S. Barnard, W. Cai, Y. C. Jun, J. S. White, and M. L. Brongersma. Plasmonics for extreme light concentration and manipulation. *Nat. Mater.*, 2010.

[101] K. J. Savage, M. M. Hawkeye, R. Esteban, A. G. Borisov, J. Aizpurua, and J. J. Baumberg. Revealing the quantum regime in tunnelling plasmonics. *Nat.*, 2012.

[102] J. A. Scholl, A. L. Koh, and J. A. Dionne. Quantum plasmon resonances of individual metallic nanoparticles. *Nat.*, 2012.

[103] C. Ciracì, R. T. Hill, J. J. Mock, Y. Urzhumov, A. I. Fernández-Domínguez, S. A. Maier, J. B. Pendry, A. Chilkoti, and D. R. Smith. Probing the ultimate limits of plasmonic enhancement. *Sci.*, 2012.

[104] S. F. Tan, L. Wu, J. K. Yang, P. Bai, M. Bosman, and C. A. Nijhuis. Quantum plasmon resonances controlled by molecular tunnel junctions. *Sci.*, 2014.

[105] H. Duan, A. I. Fernndez-Domnguez, M. Bosman, S. A. Maier, and J. K. W. Yang. Nanoplasmonics: Classical down to the nanometer scale. *Nano Lett.*, 2012.

[106] J. Zuloaga, E. Prodan, and P. Nordlander. Quantum plasmonics: Optical properties and tunability of metallic nanorods. *ACS Nano*, 2010.

[107] J. Zuloaga, E. Prodan, and P. Nordlander. Quantum description of the plasmon resonances of a nanoparticle dimer. *Nano Lett.*, 2009.

[108] M. Kuisma, A. Sakko, T. P. Rossi, A. H. Larsen, J. Enkovaara, L. Lehtovaara, and T. T. Rantala. Localized surface plasmon resonance in silver nanoparticles: Atomistic first-principles time-dependent density-functional theory calculations. *Phys. Rev. B*, 2015.

[109] X. Mei, W. Yoshida, M. Lange, J. Lee, J. Zhou, P. H. Liu, K. Leong, A. Zamora, J. Padilla, S. Sarkozy, R. Lai, and W. R. Deal. First demonstration of amplification at 1 thz using 25-nm inp high electron mobility transistor process. *IEEE Electron Device Lett.*, 2015.

[110] H. Mashiko, K. Oguri, T. Yamaguchi, A. Suda, and H. Gotoh. Petahertz optical drive with wide-bandgap semiconductor. *Nat. Phys.*, 2016.

[111] A. Schiffrin, T. Paasch-Colberg, N. Karpowicz, V. Apalkov, D. Gerster, S. Mühlbrandt, M. Korbman, J. Reichert, M. Schultze, S. Holzner, J. V. Barth, R. Kienberger, R. Ernstorfer, V. S. Yakovlev, M. I. Stockman, and F. Krausz. Optical-field-induced current in dielectrics. *Nat.*, 2012.

[112] M. Schultze, E. M. Bothschafter, A. Sommer, S. Holzner, W. Schweinberger, M. Fiess, M. Hofstetter, R. Kienberger, V. Apalkov, V. S. Yakovlev, M. I. Stockman, and F. Krausz. Controlling dielectrics with the electric field of light. *Nat.*, 2012.

[113] G. Diamant, E. Halahmi, L. Kronik, J. Levy, R. Naaman, and J. Roulston. Integrated circuits based on nanoscale vacuum phototubes. *Appl. Phys. Lett.*, 2008.

[114] J.-W. Han, D.-I. Moon, and M. Meyyappan. Nanoscale vacuum channel transistor. *Nano Lett.*, 2017.

[115] J.-W. Han, J. S. Oh, and M. Meyyappan. Vacuum nanoelectronics: Back to the future?—gate insulated nanoscale vacuum channel transistor. *Appl. Phys. Lett.*, 2012.

[116] T. Higuchi, L. Maisenbacher, A. Liehl, P. Dombi, and P. Hommelhoff. A nanoscale vacuum-tube diode triggered by few-cycle laser pulses. *Appl. Phys. Lett.*, 2015.

[117] J. D. Lee, W. S. Yun, and N. Park. Rectifying the optical-field-induced current in dielectrics: Petahertz diode. *Phys. Rev. Lett.*, 2016.

[118] P. A. M. Dirac. Quantum mechanics of many-electron systems. *Proc. Royal Soc. Lond. A: Math. Phys. Eng. Sci.*, 1929.

[119] D. M. Ceperley and B. J. Alder. Ground state of the electron gas by a stochastic method. *Phys. Rev. Lett.*, 1980.

[120] J. P. Perdew and A. Zunger. Self-interaction correction to density-functional approximations for many-electron systems. *Phys. Rev. B*, 1981.

[121] J. P. Perdew and K. Schmidt. Jacobs ladder of density functional approximations for the exchange-correlation energy. *AIP Conf. Proc.*, 2001.

[122] D. C. Langreth and M. J. Mehl. Beyond the local-density approximation in calculations of ground-state electronic properties. *Phys. Rev. B*, 1983.

[123] J. P. Perdew, K. Burke, and M. Ernzerhof. Generalized gradient approximation made simple. *Phys. Rev. Lett.*, 1996.

[124] J. Tao, J. P. Perdew, V. N. Staroverov, and G. E. Scuseria. Climbing the density functional ladder: Nonempirical meta–generalized gradient approximation designed for molecules and solids. *Phys. Rev. Lett.*, 2003.

[125] R. Car and M. Parrinello. Unified approach for molecular dynamics and density-functional theory. *Phys. Rev. Lett.*, 1985.

[126] R. N. Barnett and U. Landman. Born-oppenheimer molecular-dynamics simulations of finite systems: Structure and dynamics of $(H_2O)_2$. *Phys. Rev. B*, 1993.

[127] P. Elliott, J. I. Fuks, A. Rubio, and N. T. Maitra. Universal dynamical steps in the exact time-dependent exchange-correlation potential. *Phys. Rev. Lett.*, 2012.

[128] Y. Suzuki, L. Lacombe, K. Watanabe, and N. T. Maitra. Exact time-dependent exchange-correlation potential in electron scattering processes. *Phys. Rev. Lett.*, 2017.

[129] D. J. Tozer and N. C. Handy. On the determination of excitation energies using density functional theory. *Phys. Chem. Chem. Phys.*, 2000.

[130] N. T. Maitra. Perspective: Fundamental aspects of time-dependent density functional theory. *The J. Chem. Phys.*, 2016.

[131] Z.-h. Yang, A. Pribram-Jones, K. Burke, and C. A. Ullrich. Direct extraction of excitation energies from ensemble density-functional theory. *Phys. Rev. Lett.*, 2017.

[132] M. E. Casida. *Time-Dependent Density Functional Response Theory for Molecules*, volume 1, pages 155–192. World Scientific, 1995.

[133] K. Yabana and G. F. Bertsch. Time-dependent local-density approximation in real time. *Phys. Rev. B*, 1996.

[134] S. K. Ghosh and A. K. Dhara. Density-functional theory of many-electron systems subjected to time-dependent electric and magnetic fields. *Phys. Rev. A*, 1988.

[135] N. T. Maitra, I. Souza, and K. Burke. Current-density functional theory of the response of solids. *Phys. Rev. B*, 2003.

[136] L. Kleinman and D. M. Bylander. Efficacious form for model pseudopotentials. *Phys. Rev. Lett.*, 1982.

[137] N. Troullier and J. Martins. A straightforward method for generating soft transferable pseudopotentials. *Solid State Commun.*, 1990.

[138] S. A. Sato and K. Yabana. Efficient basis expansion for describing linear and nonlinear electron dynamics in crystalline solids. *Phys. Rev. B*, 2014.

[139] S. A. Sato, Y. Taniguchi, Y. Shinohara, and K. Yabana. Nonlinear electronic excitations in crystalline solids using meta-generalized gradient approximation and hybrid functional in time-dependent density functional theory. *The J. Chem. Phys.*, 2015.

[140] C. Kittel. *Introduction to Solid State Physics*. 2004.

[141] N. Ashcroft and N. Mermin. *Solid State Physics*. HRW international editions. 1976.

[142] W. Ritz. Über eine neue methode zur lösung gewisser variationsprobleme der mathematischen physik (a new method for solving certain variational problems of mathematical physics). *J. für die reine und angewandte Math.*, 1909.

[143] J. K. L. MacDonald. Successive approximations by the rayleigh-ritz variation method. *Phys. Rev.*, 1933.

[144] M. Reed and B. Simon. *The min-max principle*, pages 75–79. Methods of Modern Mathematical Physics. 1978.

[145] J. E. Lennard-Jones. The electronic structure of some diatomic molecules. *Trans. Faraday Soc.*, 1929.

[146] J. M. Soler, E. Artacho, J. D. Gale, A. Garca, J. Junquera, P. Ordejn, and D. Snchez-Portal. The siesta method for ab initio order-N materials simulation. *J. Physics: Condens. Matter*, 2002.

[147] J. VandeVondele, M. Krack, F. Mohamed, M. Parrinello, T. Chassaing, and J. Hutter. Quickstep: Fast and accurate density functional calculations using a mixed gaussian and plane waves approach. *Comput. Phys. Commun.*, 2005.

[148] R. A. Kendall, E. Apr, D. E. Bernholdt, E. J. Bylaska, M. Dupuis, G. I. Fann, R. J. Harrison, J. Ju, J. A. Nichols, J. Nieplocha, T. Straatsma, T. L. Windus, and A. T. Wong. High performance computational chemistry: An overview of nwchem a distributed parallel application. *Comput. Phys. Commun.*, 2000.

[149] A. H. Larsen, M. Vanin, J. J. Mortensen, K. S. Thygesen, and K. W. Jacobsen. Localized atomic basis set in the projector augmented wave method. *Phys. Rev. B*, 2009.

[150] J. Kong, C. A. White, A. I. Krylov, D. Sherrill, R. D. Adamson, T. R. Furlani, M. S. Lee, A. M. Lee, S. R. Gwaltney, T. R. Adams, C. Ochsenfeld, A. T. B. Gilbert,

G. S. Kedziora, V. A. Rassolov, D. R. Maurice, N. Nair, Y. Shao, N. A. Besley, P. E. Maslen, J. P. Dombroski, H. Daschel, W. Zhang, P. P. Korambath, J. Baker, E. F. C. Byrd, T. Van Voorhis, M. Oumi, S. Hirata, C.-P. Hsu, N. Ishikawa, J. Florian, A. Warshel, B. G. Johnson, P. M. W. Gill, M. Head-Gordon, and J. A. Pople. Q-chem 2.0: a high-performance ab initio electronic structure program package. *J. Comput. Chem.*, 2000.

[151] J. J. Goings and X. Li. An atomic orbital based real-time time-dependent density functional theory for computing electronic circular dichroism band spectra. *The J. Chem. Phys.*, 2016.

[152] K. Lopata and N. Govind. Modeling fast electron dynamics with real-time time-dependent density functional theory: Application to small molecules and chromophores. *J. Chem. Theory Comput.*, 2011.

[153] C. Jamorski, M. E. Casida, and D. R. Salahub. Dynamic polarizabilities and excitation spectra from a molecular implementation of timedependent densityfunctional response theory: N2 as a case study. *The J. Chem. Phys.*, 1996.

[154] R. Bauernschmitt, M. Hser, O. Treutler, and R. Ahlrichs. Calculation of excitation energies within time-dependent density functional theory using auxiliary basis set expansions. *Chem. Phys. Lett.*, 1997.

[155] M. E. Casida, C. Jamorski, K. C. Casida, and D. R. Salahub. Molecular excitation energies to high-lying bound states from time-dependentdensity-functionalresponsetheory: Characterizationand correctionofthetime-dependentlocaldensityapproximation ionization threshold. *The J. Chem. Phys.*, 1998.

[156] G. Kresse and J. Furthmüller. Efficient iterative schemes for ab initio total-energy calculations using a plane-wave basis set. *Phys. Rev. B*, 1996.

[157] P. Giannozzi, S. Baroni, N. Bonini, M. Calandra, R. Car, C. Cavazzoni, D. Ceresoli, G. L. Chiarotti, M. Cococcioni, I. Dabo, A. D. Corso, S. de Gironcoli, S. Fabris, G. Fratesi, R. Gebauer, U. Gerstmann, C. Gougoussis, A. Kokalj, M. Lazzeri, L. Martin-Samos, N. Marzari, F. Mauri, R. Mazzarello, S. Paolini, A. Pasquarello, L. Paulatto, C. Sbraccia, S. Scandolo, G. Sclauzero, A. P. Seitsonen, A. Smogunov, P. Umari, and R. M. Wentzcovitch. Quantum espresso: a modular and open-source software project for quantum simulations of materials. *J. Physics: Condens. Matter*, 2009.

[158] X. Gonze, J.-M. Beuken, R. Caracas, F. Detraux, M. Fuchs, G.-M. Rignanese, L. Sindic, M. Verstraete, G. Zerah, F. Jollet, M. Torrent, A. Roy, M. Mikami, P. Ghosez, J.-Y. Raty, and D. Allan. First-principles computation of material properties: the abinit software project. *Comput. Mater. Sci.*, 2002.

[159] M. C. Payne, M. P. Teter, D. C. Allan, T. A. Arias, and J. D. Joannopoulos. Iterative minimization techniques for ab initio total-energy calculations: molecular dynamics and conjugate gradients. *Rev. Mod. Phys.*, 1992.

[160] K. Varga and J. A. Driscoll. *Computational Nanoscience*. 2011.

[161] E. L. Briggs, D. J. Sullivan, and J. Bernholc. Real-space multigrid-based approach to large-scale electronic structure calculations. *Phys. Rev. B*, 1996.

[162] T. L. Beck. Real-space mesh techniques in density-functional theory. *Rev. Mod. Phys.*, 2000.

[163] M. M. G. Alemany, M. Jain, L. Kronik, and J. R. Chelikowsky. Real-space pseudopotential method for computing the electronic properties of periodic systems. *Phys. Rev. B*, 2004.

[164] P. Maragakis, J. Soler, and E. Kaxiras. Variational finite-difference representation of the kinetic energy operator. *Phys. Rev. B*, 2001.

[165] J. Bernholc, M. Hodak, and W. Lu. Recent developments and applications of the real-space multigrid method. *J. Physics: Condens. Matter*, 2008.

[166] G. F. Bertsch, J.-I. Iwata, A. Rubio, and K. Yabana. Real-space, real-time method for the dielectric function. *Phys. Rev. B*, 2000.

[167] W. Burdick, Y. Saad, L. Kronik, I. Vasiliev, M. Jain, and J. R. Chelikowsky. Parallel implementation of time-dependent density functional theory. *Comput. Phys. Commun.*, 2003.

[168] J. J. Mortensen, L. B. Hansen, and K. W. Jacobsen. Real-space grid implementation of the projector augmented wave method. *Phys. Rev. B*, 2005.

[169] E. L. Briggs, C. T. Kelley, and J. Bernholc. Parallel implementation of electronic structure eigensolver using a partitioned folded spectrum method. 2015. (Accessed 2018).

[170] M. Walter, H. Hkkinen, L. Lehtovaara, M. Puska, J. Enkovaara, C. Rostgaard, and J. J. Mortensen. Time-dependent density-functional theory in the projector augmented-wave method. *The J. Chem. Phys.*, 2008.

[171] M. A. Marques, A. Castro, G. F. Bertsch, and A. Rubio. octopus: a first-principles tool for excited electron-ion dynamics. *Comput. Phys. Commun.*, 2003.

[172] R. D. King-Smith, M. C. Payne, and J. S. Lin. Real-space implementation of non-local pseudopotentials for first-principles total-energy calculations. *Phys. Rev. B*, 1991.

[173] Z. Ma and M. Tuckerman. Constant pressure ab initio molecular dynamics with discrete variable representation basis sets. *The J. Chem. Phys.*, 2010.

[174] H.-S. Lee and M. E. Tuckerman. Ab initio molecular dynamics with discrete variable

representation basis sets: techniques and application to liquid water. *The J. Phys. Chem. A*, 2006.

[175] Y. Liu, D. A. Yarne, and M. E. Tuckerman. Ab initio molecular dynamics calculations with simple, localized, orthonormal real-space basis sets. *Phys. Rev. B*, 2003.

[176] K. Varga, Z. Zhang, and S. T. Pantelides. “lagrange functions”: A family of powerful basis sets for real-space order-N electronic structure calculations. *Phys. Rev. Lett.*, 2004.

[177] S. Choi, K. Hong, J. Kim, and W. Y. Kim. Accuracy of lagrange-sinc functions as a basis set for electronic structure calculations of atoms and molecules. *The J. Chem. Phys.*, 2015.

[178] D. T. Colbert and W. H. Miller. A novel discrete variable representation for quantum mechanical reactive scattering via the s-matrix kohn method. *The J. Chem. Phys.*, 1992.

[179] J. P. Boyd. Sum-accelerated pseudospectral methods: the Euler-accelerated sinc algorithm. *Appl. Numer. Math.*, 1991.

[180] J. P. Boyd. Sum-accelerated pseudospectral methods: Finite differences and sech-weighted differences. *Comput. Methods Appl. Mech. Eng.*, 1994.

[181] D. A. Mazziotti. Spectral difference methods for solving the differential equations of chemical physics. *The J. Chem. Phys.*, 2002.

[182] D. Kidd, B. Pearson, C. Covington, and K. Varga. Accelerated pseudospectral basis in density functional calculations. *Int. J. Quantum Chem.*, 2017.
Copyright © 2017 Wiley Periodicals, Inc.

[183] A. Schleife, E. W. Draeger, Y. Kanai, and A. A. Correa. Plane-wave pseudopotential

implementation of explicit integrators for time-dependent kohn-sham equations in large-scale simulations. *The J. Chem. Phys.*, 2012.

[184] A. Castro, M. A. L. Marques, and A. Rubio. Propagators for the time-dependent kohn–sham equations. *The J. Chem. Phys.*, 2004.

[185] H. TalEzer and R. Kosloff. An accurate and efficient scheme for propagating the time dependent schrödinger equation. *The J. Chem. Phys.*, 1984.

[186] A. Russakoff, S. Bubin, X. Xie, S. Erattupuzha, M. Kitzler, and K. Varga. Time-dependent density-functional study of the alignment-dependent ionization of acetylene and ethylene by strong laser pulses. *Phys. Rev. A*, 2015.

[187] A. Russakoff and K. Varga. Time-dependent density-functional study of the ionization and fragmentation of $\mathrm{C_2H_2}$ and $\mathrm{H_2}$ by strong circularly polarized laser pulses. *Phys. Rev. A*, 2015.

[188] J. A. Driscoll, S. Bubin, W. R. French, and K. Varga. Time-dependent density functional study of field emission from nanotubes composed of C, BN, SiC, Si, and GaN. *Nanotechnol.*, 2011.

[189] J. A. Driscoll, S. Bubin, and K. Varga. Laser-induced electron emission from nanostructures: A first-principles study. *Phys. Rev. B*, 2011.

[190] S. Bubin and K. Varga. First-principles time-dependent simulation of laser assisted desorption of hydrogen atoms from H-Si(111) surface. *Appl. Phys. Lett.*, 2011.

[191] S. Bubin and K. Varga. Electron-ion dynamics in laser-assisted desorption of hydrogen atoms from H-Si(111) surface. *J. Appl. Phys.*, 2011.

[192] K. A. Bagrinovskii and S. K. Godunov. Difference schemes for multi-dimensional problems. *Dokl. Acad. Nauk,*, 1957.

[193] G. Strang. On the construction and comparison of difference schemes. *SIAM J. Numer. Anal.*, 1968.

[194] M. Feit, J. Fleck, and A. Steiger. Solution of the schrödinger equation by a spectral method. *J. Comput. Phys.*, 1982.

[195] O. Sugino and Y. Miyamoto. Density-functional approach to electron dynamics: Stable simulation under a self-consistent field. *Phys. Rev. B*, 1999.

[196] T. Jahnke and C. Lubich. Error bounds for exponential operator splittings. *BIT Numer. Math.*, 2000.

[197] A. Castro, M. A. L. Marques, and A. Rubio. Propagators for the time-dependent Kohn–Sham equations. *J. Chem. Phys.*, 2004.

[198] S. M. Cox and P. C. Matthews. Exponential time differencing for stiff systems. *J. Comput. Phys.*, 2002.

[199] J. P. Boyd. *Chebyshev and Fourier Spectral Methods*. 1999.

[200] B. Fornberg and T. A. Driscoll. A fast spectral algorithm for nonlinear wave equations with linear dispersion. *J. Comput. Phys*, 1999.

[201] A.-K. Kassam and L. N. Trefethen. Fourth-order time-stepping for stiff PDEs. *SIAM J. Sci. Comput.*, 2005.

[202] P. A. Milewski and E. G. Tabak. A pseudospectral procedure for the solution of nonlinear wave equations with examples from free-surface flows. *SIAM J. Sci. Comput.*, 1999.

[203] A. L. Frapiccini, A. Hamido, S. Schröter, D. Pyke, F. Mota-Furtado, P. F. O'Mahony, J. Madroñero, J. Eiglsperger, and B. Piraux. Explicit schemes for time propagating many-body wave functions. *Phys. Rev. A*, 2014.

[204] B. Sportisse. An analysis of operator splitting techniques in the stiff case. *J. Comput. Phys.*, 2000.

[205] D. Kidd, C. Covington, and K. Varga. Exponential integrators in time-dependent density-functional calculations. *Phys. Rev. E*, 2017.
Copyright © 2017 by the American Physical Society.

[206] Y. Y. Lu. Computing a matrix function for exponential integrators. *J. Comput. Appl. Math.*, 2003.

[207] M. Hochbruck and C. Lubich. On krylov subspace approximations to the matrix exponential operator. *SIAM J. Numer. Anal.*, 1997.

[208] G. Beylkin, J. M. Keiser, and L. Vozovoi. A new class of time discretization schemes for the solution of nonlinear PDEs. *J. Comput. Phys.*, 1998.

[209] M. Tokman. Efficient integration of large stiff systems of odes with exponential propagation iterative (EPI) methods. *J. Comput. Phys.*, 2006.

[210] S. Krogstad. Generalized integrating factor methods for stiff PDEs. *J. Comput. Phys.*, 2005.

[211] C. Covington, D. Kidd, J. Gilmer, and K. Varga. Simulation of electron dynamics subject to intense laser fields using a time-dependent volkov basis. *Phys. Rev. A*, 2017.
Copyright © 2017 by the American Physical Society.

[212] Q. Su and J. Eberly. Model atom for multiphoton physics. *Phys. Rev. A*, 1991.

[213] A. Castro, A. Rubio, and E. K. U. Gross. Enhancing and controlling single-atom high-harmonic generation spectra: a time-dependent density-functional scheme. *Eur. Phys. J. B*, 2015.

[214] D. E. Manolopoulos. Derivation and reflection properties of a transmission-free absorbing potential. *J. Chem. Phys.*, 2002.

[215] R. Carb and B. Calabuig. Molecular quantum similarity measures and n-dimensional representation of quantum objects. i. theoretical foundations. *Int. J. Quantum Chem.*, 1992.

[216] D. Kidd, C. Covington, Y. Li, and K. Varga. Volkov basis for simulation of interaction of strong laser pulses and solids. *Phys. Rev. B*, 2018.
Copyright © 2017 by the American Physical Society.

[217] X.-M. Tong, G. Wachter, S. A. Sato, C. Lemell, K. Yabana, and J. Burgdörfer. Application of norm-conserving pseudopotentials to intense laser-matter interactions. *Phys. Rev. A*, 2015.

[218] D. Kidd, X. Xu, C. Covington, K. Watanabe, and K. Varga. Simulation of laser-induced rectification in a nano-scale diode. *J. Appl. Phys.*, 2018.
Copyright © 2018 AIP Publishing.

[219] B. Ahn, J. Schötz, M. Kang, W. A. Okell, S. Mitra, B. Förg, S. Zherebtsov, F. Sößmann, C. Burger, M. Kbel, C. Liu, A. Wirth, E. D. Fabrizio, H. Yanagisawa, D. Kim, B. Kim, and M. F. Kling. Attosecond-controlled photoemission from metal nanowire tips in the few-electron regime. *APL Photonics*, 2017.

[220] M. A. Gubko, W. Husinsky, A. A. Ionin, S. I. Kudryashov, S. V. Makarov, C. R. Nathala, A. A. Rudenko, L. V. Seleznev, D. V. Sinitsyn, and I. V. Treshin. Enhancement of ultrafast electron photoemission from metallic nanoantennas excited by a femtosecond laser pulse. *Laser Phys. Lett.*, 2014.

[221] L. Wimmer, G. Herink, D. R. Solli, S. V. Yalunin, K. E. Echternkamp, and C. Ropers. Terahertz control of nanotip photoemission. *Nat. Phys.*, 2014.

[222] V. Schweikhard, A. Grubisic, T. A. Baker, I. Thomann, and D. J. Nesbitt. Polarization-dependent scanning photoionization microscopy: Ultrafast plasmon-mediated electron ejection dynamics in single au nanorods. *ACS Nano*, 2011.

[223] D. J. Park, B. Piglosiewicz, S. Schmidt, H. Kollmann, M. Mascheck, and C. Lienau. Strong field acceleration and steering of ultrafast electron pulses from a sharp metallic nanotip. *Phys. Rev. Lett.*, 2012.

[224] K. Yoshioka, I. Katayama, Y. Minami, M. Kitajima, S. Yoshida, H. Shigekawa, and J. Takeda. Real-space coherent manipulation of electrons in a single tunnel junction by single-cycle terahertz electric fields. *Nat Photon*, 2016.

[225] M. Kruger, M. Schenk, and P. Hommelhoff. Attosecond control of electrons emitted from a nanoscale metal tip. *Nat.*, 2011.

[226] V. Jelic, K. Iwaszczuk, P. H. Nguyen, C. Rathje, G. J. Hornig, H. M. Sharum, J. R. Hoffman, M. R. Freeman, and F. A. Hegmann. Ultrafast terahertz control of extreme tunnel currents through single atoms on a silicon surface. *Nat Phys*, 2017.

[227] T. Rybka, M. Ludwig, M. F. Schmalz, V. Knittel, D. Brida, and A. Leitenstorfer. Sub-cycle optical phase control of nanotunnelling in the single-electron regime. *Nat Photon*, 2016.

[228] A. Schiffrin, T. Paasch-Colberg, N. Karpowicz, V. Apalkov, D. Gerster, S. Muhlbrandt, M. Korbman, J. Reichert, M. Schultze, S. Holzner, J. V. Barth, R. Kienberger, R. Ernstorfer, V. S. Yakovlev, M. I. Stockman, and F. Krausz. Optical-field-induced current in dielectrics. *Nat.*, 2013.

[229] S.-G. Jeon, D. Shin, and M. S. Hur. Violation of the transit-time limit toward generation of ultrashort electron bunches with controlled velocity chirp. *Sci. Reports*, 2016.

[230] J. Hoffrogge, J. P. Stein, M. Krüger, M. Förster, J. Hammer, D. Ehberger, P. Baum, and P. Hommelhoff. Tip-based source of femtosecond electron pulses at 30kev. *J. Appl. Phys.*, 2014.

[231] W. Ekardt. Dynamical polarizability of small metal particles: Self-consistent spherical jellium background model. *Phys. Rev. Lett.*, 1984.

[232] M. Brack. The physics of simple metal clusters: self-consistent jellium model and semiclassical approaches. *Rev. Mod. Phys.*, 1993.

[233] M. Madjet, C. Guet, and W. R. Johnson. Comparative study of exchange-correlation effects on the electronic and optical properties of alkali-metal clusters. *Phys. Rev. A*, 1995.

[234] L. Novotny and B. Hecht. *Principles of Nano-Optics*. Cambridge University Press, 2012.

[235] N. Nakaoka, K. Tada, S. Watanabe, H. Fujita, and K. Watanabe. Partitioned real-space density functional calculations of bielectrode systems under bias voltage and electric field. *Phys. Rev. Lett.*, 2001.